



University of Crete

PhD Thesis

**Photonic Crystals with
tunable properties**

Ioanna Sakellari

Supervisor: Costas Fotakis

Co-Supervisors: Maria Farsari, David Gray

Heraklion, June 2011

Contents

I	Theoretical Background	8
1	Chapter 1: Photonic Crystals	8
1.1	Basic concepts	8
1.2	Light propagation in Photonic Crystals	10
1.3	Bloch waves and Brillouin zones	14
1.3.1	The Photonic Band Structure	14
1.3.2	The Photonic Band Gap	17
1.3.3	An example: 1D photonic crystal	18
1.4	Refraction law for Photonic Crystals	21
1.4.1	Refraction at an interface	21
1.4.2	Group velocity and Equiphase surfaces	24
1.4.3	Bragg Diffraction	27
1.5	The Woodpile structure	28
2	Chapter 2: 3D Fabrication of Photonic nanostructures	31
2.1	Direct laser writing	31
2.1.1	Polymerization by two - photon absorption	32
2.1.2	Photo-polymerization via two-photon absorption	33
2.1.3	Resolution limits	36
3	Chapter 3: Sol - Gel process	39
3.1	Materials Fabrication	39
3.1.1	Sol - Gel technique	39
4	Chapter 4: Linear and Non-linear materials characterization techniques	43
4.1	Characterization techniques for Linear materials	43
4.1.1	The Prism-film coupler	43
4.1.2	Waveguide modes	45
4.1.3	Prism-film coupling modes	47
4.2	Characterization techniques for Non-Linear materials	48
4.2.1	Basic concepts of nonlinear optics	49
4.2.2	Non-linear optical media	50
4.2.3	The optical Kerr effect	54

4.2.4	Non-linear molecules	59
II	Experimental	61
5	Chapter 5: Fabrication, Characterization and Simulation	61
5.1	Fabrication via Direct Laser Writing	61
5.2	Optical Characterization	63
5.2.1	Angle Resolved Transmittance Measurements	63
5.2.2	Bragg Diffraction Measurements	64
5.3	Simulation	67
6	Chapter 6: Linear Index Tuning of Titanium containing sol - gel composites	72
6.1	Titanium sol -gel composites	72
6.1.1	Materials preparation process	77
6.1.2	Measurement of the linear refractive index	79
7	Chapter 7: High resolution 3D woodpile structures with a response in the visible range	88
7.1	Zirconium - Dmaema sol - gel composites	89
7.1.1	Materials preparation process	93
7.2	High resolution woodpile structures: the $\frac{c}{\lambda}$ challenge	95
7.2.1	Multiple exposures scheme	96
7.2.2	High resolution woodpiles structures	100
7.3	Optical Characterization	103
7.3.1	Theoretical calculations and FTIR measurements . . .	104
7.3.2	Diffraction patterns	105
8	Chapter 8: NonLinear Photonic crystals of CdS - Zirconium-Dmaema polymer composites	109
8.1	CdS -Zirconium-Dmaema composite	109
8.1.1	Synthesis of CdS-Polymer Nanocomposites	110
8.2	Linear Characterization	112
8.2.1	Angle resolved transmittance measurements	112
8.3	Nonlinear characterization	114
8.3.1	Nonlinear material characterization: Z-scan method . .	114
8.3.2	Z-scan measurements	118

8.3.3 Pump and Probe technique	120
9 Conclusions	126
III Appendices	130
IV Bibliography	135

Introduction

Interaction between light and matter is the main subject of nanophotonics. For most systems, the interaction is electronic, that is, it involves changes in the properties of electrons present in the system. Recently however, this approach has been reversed [76, 29]: light instead of electrons will serve as the information carrier. Thus, the confinement of photons in analogy with the confinement of electrons is the fundamental alteration in these interactions. This feature can be explained from a simple standpoint, that is, light presents several advantages over the electron; it can travel in a dielectric material at much greater speeds than an electron in a metallic wire and also photons are not strongly interacting with each other as with electrons, which helps reduce energy losses [27]. Hence, there is a strong need to design materials so that they can affect the properties of photons, in much the same way that a semiconductor crystal affects the properties of electrons. Both Yablonovitch and John [76, 29] suggested that structures with a periodic variation in the dielectric constant could influence the nature of photonic modes in a material. In this sense, the answer to this need is met through the realization of photonic crystals, which are artificial periodic nanostructures designed to control and manipulate the flow of light.

Essentially, it is difficult to confine or stop light. Since, a photon has no charge or rest mass, it cannot be trapped by an external field potential. This is different from electrons whose confinement is always an easy task. To confine photons one can employ some kind of reflection, which usually occurs at a boundary separating materials with different refractive indices [46]. Photonic crystals are materials patterned with a periodicity in dielectric constant with a repeat unit of the order of the wavelength of light. If the dielectric constants of the constituent materials are different enough, Bragg scattering off the dielectric interfaces can create a range of “forbidden” frequencies called a photonic band gap. Photons with energies lying in the band gap cannot propagate through the medium. This provides the opportunity to shape and mould the flow of light for photonic information technology.

Therefore, one way to induce nanoscale light and matter interaction is to confine light to nanoscale dimensions that are much smaller than the wavelength of light. In addition, a second approach would suggest to confine matter to

nanoscale dimensions in order to make nanomaterials for photonics. This involves the various ways of confining the dimensions of matter to produce nanostructures. For example, using nanoparticles that exhibit unique electronic and photonic properties. Hence, the control of materials chemistry is critical to create desired 3D structures with preferred materials properties, such as high refractive index, high transmission at the wavelength of interest, wide tunability, and high thermal and mechanical stability [44]. Furthermore, in order to fabricate structures of a nanometer size scale, a third approach is to require nanoscale photo-processes suitable for nanolithography. An important feature of nanofabrication is that the photo-processes can be confined to well-defined nanoregions, so that structures can be fabricated in a precise geometry and arrangement.

Considering these three approaches mentioned above for nanoscale light confinement, one comes across the main scope of this thesis which deals with the fabrication and characterization of 3D linear and nonlinear photonic crystals. In particular, we focus on 3D fabrication of high quality photonic structures and on the design of stimulus-responsive materials for dynamic tuning of photonic properties. The systems under study are woodpile based photonic crystals fabricated by means of the two photon polymerization technique. For this reason, the synthesis of novel linear and nonlinear materials suitable for two photon fabrication, with proper optical and mechanical properties necessary for the fabrication of precise 3D photonic structures will be the starting point in our study. Following this, the study of the optical properties of these novel materials in combination with the study of the optical properties of the fabricated structures will lead us towards the complete characterization of such 3D photonic systems. This thesis is organized as follows:

Chapter 1: A short introduction is given about the main principles of photonic crystals. Basic concepts, such as photonic bands and band gaps are briefly discussed as well as, light propagation in terms of Maxwell Equations and Bloch waves typical for the case of periodic structures. Light confinement, frequency dispersion and spatial dispersion represent the basic characteristics of such periodic structures providing the possibility to affect the properties of photons in the same way that a semiconductor crystal affects the properties of electrons.

Chapter 2: Fabrication aspects are briefly described. Direct writing using

a tightly focused femtosecond laser beam exploits nonlinear absorption induced by intense irradiation to provide a well controllable tool for the creation of spatially defined structures. Photopolymerization based on two - photon absorption is used to initiate chemical processes to convert liquid - state monomers to solid macromolecules. Since the nonlinear absorption takes place at high irradiance regions i.e. at the beam focus, the induced photo - polymerization is restricted within the focal volume of the photosensitive resin enabling the formation of features close to 100nm in size.

- Chapter 3: Precise 3D photonic structures are directly patterned from an organic - inorganic hybrid photoresist. The sol - gel reaction is described as it serves as the basic tool for the incorporation of dopants or other functionalized groups into organic nanocomposites. Inorganic - organic hybrid materials synthesized in this way offer better properties than those prepared alone.
- Chapter 4: Linear and nonlinear materials characterization techniques are extensively discussed. For linear refractive index measurements, the prism film coupler technique will be employed, whereas for the case of nonlinear materials, the Z-scan method will be developed. A short introduction about nonlinear material processes is also given.
- Chapter 5: Fabrication, characterization and simulation methods are extensively discussed, as we turn to the experimental part of this thesis. A brief description is given of the experimental layout related to the nanofabrication, optical characterization and theoretical simulations and used for a better understanding of the experimental procedures described in the following chapters.
- Chapter 6: Altering material properties on a nanometer size scale is a critical issue to create the desired 3D nanostructures. For that purpose, the sol - gel method is used to incorporate inorganic dopants into organic nanocomposites. In particular, a titanium alkoxide precursor is added to organosilicates prepared from 3-methacryloxypropyl trimethoxysilane with water and an acid catalyst. The addition of such a transition metal alkoxide to methacrylic

acid (MAA) produces photo-cross-linkable organic-inorganic composites with preferred materials properties. By changing the ratio of the metal alkoxide/titanium and the ratio of the precursor/titanium we are able to tune the refractive index of the resulting materials.

Chapter 7: A novel hybrid zirconium – dmaema based material is used for the fabrication of precise woodpile structures with feature sizes of 100nm, inlayer periodicity of 400nm and an optical response in the visible range of frequencies. In addition, a new method for high resolution micro-structuring is presented, which involves multiple exposures. Fabrication of micro-structures below the polymerization threshold is tuned depending on the number of exposure times. Angle-resolved transmission spectroscopy is employed to characterize the fabricated structures, while diffraction patterns obtained under white light continuum illumination demonstrate the high quality of our samples.

Chapter 8: Design of stimulus - responsive materials for dynamic tuning of photonic properties in the main subject discussed in this chapter. The incorporation of quantum dot semiconductor nanocrystals in the zirconium - dmaema complex composite can lead to a significant modification of light - matter interactions, since the energy of band - to - band transitions in semiconductor microcrystals embedded can overlap with the photonic band gap region. The z - scan method is employed for the nonlinear refractive index measurements. A pump and probe technique is used for the dynamic tuning of the photonic optical properties.

Part I

Theoretical Background

1 Chapter 1: Photonic Crystals

A short introduction is given about the main principles of photonic crystals. Basic concepts, such as photonic bands and band gaps are briefly discussed as well as, light propagation in terms of Maxwell Equations and Bloch waves typical for the case of periodic structures. Light confinement, frequency dispersion and spatial dispersion represent the basic characteristics of such periodic structures providing the possibility to affect the properties of photons in the same way that a semiconductor crystal affects the properties of electrons.

1.1 Basic concepts

Simply stated, a photonic crystal is an artificial periodic array of two different dielectric media with the periodicity extending in one, two or three spacial dimensions. The characteristic of such structures is that the period length is comparable to the wavelength of light in the material i.e. within several hundreds of nanometers in the case of a photonic crystal working in the optical range of electromagnetic spectrum. And, this is a big difference comparing to ordinary crystals, where the scale of the lattice constant is on the order of angstroms. Figure 1.1 shows the simplest case in which two materials are stacked alternatively. The lattice constant here is the spatial period of the stack, since it corresponds to the lattice constant of ordinary crystals composed of a regular array of atoms.

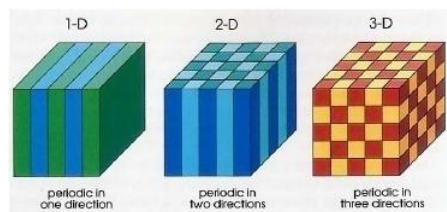


Figure 1.1: Photonic crystals in one, two and three dimensions[28]

In electronic materials, the crystal is a periodic arrangement of atoms or molecules. The pattern with which the atoms or molecules are repeated in space is the crystal lattice. The crystallinity due to nuclear attractions, presents a periodic potential to electrons propagating through it and both the constituents of the crystal and the geometry of the lattice dictate the conduction properties of the crystal. From quantum mechanics is well known that electrons propagate as waves, and waves that meet certain criteria can travel through a periodic potential without scattering (although they will be scattered by defects and impurities). However, the lattice can prohibit the propagation of certain waves, meaning that electrons are forbidden to propagate with certain energies in certain directions. This range of energies form, the so called, electronic band gap.

A photonic crystal, analogous to an electronic crystal, describes a periodic dielectric domain (periodic modulation of refractive index) equivalent to the periodic potential, but now with the periodicity at much larger scales matched to the wavelength of the photons. The atoms or molecules are replaced by macroscopic media with differing dielectric constants. Similar to electrostatic interactions introducing a resistance to the flow of electrons, the dielectric constant and the related refractive index describe the resistance of a medium to the propagation of photons. If the dielectric constants of the materials in the crystal are sufficiently different and if the absorption of light by the materials is minimal, then the refractions and reflections of light from all the various interfaces can produce many of the same phenomena for photons (light modes) that the atomic potential produces for electrons. In particular, it is possible to design and construct photonic crystals with photonic band gaps: light is prevented from propagating in certain directions with specified energies. But also, a photonic crystal can allow propagation in anomalous and useful ways [28].

Typical examples of periodic arrangements of macroscopic dielectric media in two dimensions are shown in figure 1.2. A rod - type photonic crystal i.e. dielectric rods in air background or either air atoms in a high dielectric medium (hole - type photonic crystals) are arranged following a square symmetry. However, the optical analogue of an ordinary electronic crystal is a three dimensional photonic crystal, i.e. a dielectric structure that is periodic along three different axes. Several examples of three dimensional photonic

crystals are shown in figure 1.3: dielectric spheres stacked in an FCC lattice (a), a drilled dielectric known as Yablonovite (b), an inverse opal (c) and a stack of orthogonal dielectric logs (woodpile structure)(d).

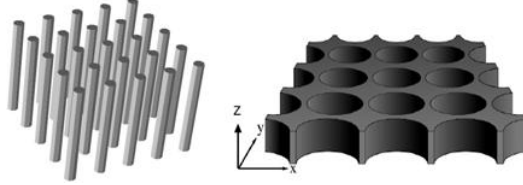


Figure 1.2: Two dimensional photonic crystals

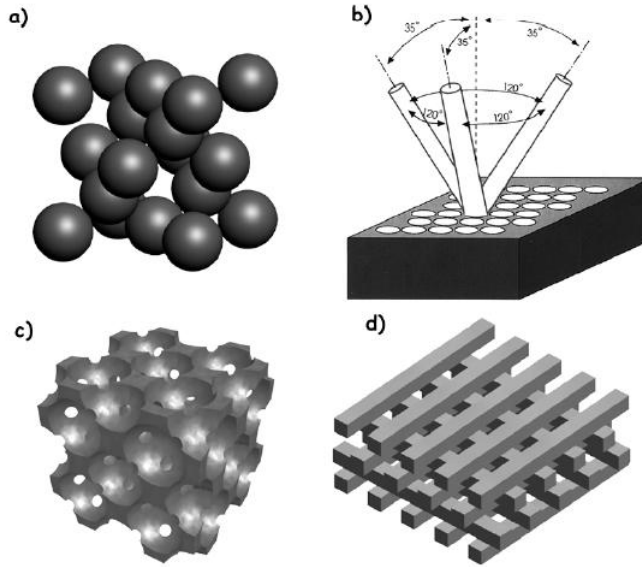


Figure 1.3: Photonic crystals in three dimensions

1.2 Light propagation in Photonic Crystals

The propagation of electromagnetic waves in media free of charges and currents is governed by the four Maxwell equations. We restrict our discussion to propagation in a mixed dielectric medium, a composite of regions of homogenous dielectric material as function of the Cartesian position vector \mathbf{r} , in which the structure does not vary with time. In S.I units they are:

$$\begin{aligned} \nabla \cdot B &= 0 & \nabla \times E + \frac{\partial B}{\partial t} &= 0 \\ \nabla \cdot D &= 0 & \nabla \times H - \frac{\partial D}{\partial t} &= 0 \end{aligned} \quad (1.1)$$

Four assumptions are considered: a) the field strength is small enough, so we approximate the linear regime; b) the material is macroscopic and isotropic so that $D(r,\omega)$ and $E(r,\omega)$ are related by $\varepsilon_0 = 8.854 \times 10^{-12}$ Faraday/m multiplied by a scalar dielectric function $\varepsilon(r,\omega)$, the relative permittivity; c) we ignore any frequency dependence (material dispersion) of the dielectric constant, instead we choose the value of the dielectric constant appropriate to the frequency range of the physical system in question; d) we consider transparent materials, i.e. $\varepsilon(r)$ is purely real and positive. In this way, we have $D(r) = \varepsilon_0 \varepsilon(r)E(r)$, $B(r) = \mu_0 \mu(r)H(r)$ (where $\mu_0 = 4\pi \times 10^{-7}$ Henry/m, the vacuum permeability). But for most dielectric materials of interest $\mu(r)$ is close to unity, so in that case $\varepsilon = n^2$ ($n = \sqrt{\varepsilon\mu}$). Considering the previous assumptions, the Maxwell equations become:

$$\begin{aligned}
\nabla H(r, t) &= 0 \\
\nabla[\varepsilon(r)E(r)] &= 0 \\
\nabla \times E(r, t) + \mu_0 \frac{\partial H(r, t)}{\partial t} &= 0 \\
\nabla \times H(r, t) - \varepsilon_0 \varepsilon(r) \frac{\partial E(r, t)}{\partial t} &= 0
\end{aligned} \tag{1.2}$$

Exploiting the linearity of Maxwell equations, we separate the time dependence from the spatial dependence by expanding the fields $E(r,t)$ and $H(r,t)$ into a set of harmonic modes. We use a complex-valued field taking the real part, so that we can write a harmonic mode as a spatial profile times a complex exponential (recall that a mode is defined as a stationary field configuration oscillating with frequency ω that satisfies the homogenous Maxwell's equations):

$$\begin{aligned}
H(r, t) &= H(r)e^{-i\omega t} \\
E(r, t) &= E(r)e^{-i\omega t}
\end{aligned} \tag{1.3}$$

To find the equations governing the mode profiles for a given frequency, we insert the above equations into (1.2). The two divergence equations imply that there are not point sources and magnetic fields in the medium. Equivalently, the fields configurations are build up of electromagnetic waves that are transverse. Which means that for a plane wave wher $H(r) = a \exp(ikr)$

for some wave vector k , equations 1.2.1 and 1.2.2 require that $\mathbf{a} \star \mathbf{k} = 0$. So, the direction of the electromagnetic field, \mathbf{k} , \mathbf{E} and \mathbf{H} , are mutually perpendicular in the form of a right-handed cartesian system. Then, starting from the two curl equations, dividing equation 1.2.4 by $\varepsilon(r)$, taking the curl and replacing by $c = \sqrt{\frac{1}{\varepsilon_0 \mu_0}}$, we get the following result:

$$\nabla \times \left(\frac{1}{\varepsilon(r)} \nabla \times H(r) \right) = \frac{\omega^2}{c^2} H(r) \quad (1.4)$$

Equation (1.4) (often referred to as the “master equation”) is essentially an eigenvalue problem, i.e. an operation on a function (eigenfunction or eigenvector) which is just the function itself, multiplied by some constant (eigenvalue). In our case, the eigen-operator is expressed by $\Theta = \nabla \times \left(\frac{1}{\varepsilon(r)} \nabla \times \right)$, the fields $H(r)$ are the eigenfunctions and the eigenvalues are given by $\frac{\omega^2}{c^2}$. The eigenvectors $H(r)$ are the spatial patterns of the harmonic modes, and the eigenvalues are proportional to the squared frequencies of those modes. A key here is that the operator Θ is Hermitian [28], which leads to some nice properties: the eigenfrequencies ω are real and that the eigenstates are orthogonal.

1. ω^2 is real: $(H, \Theta H) = \left(\frac{\omega^2}{c^2} \right) (H, H) = (\Theta H, H) = \left(\frac{\omega^2}{c^2} \right) (H, H)$
2. ω^2 is positive: $\left(\frac{\omega^2}{c^2} \right) (H, H) = (H, \Theta H) = \int dr \frac{1}{\varepsilon(r)} |\nabla \times H|^2$ (1.5)
3. two modes $H_1(r)$ and $H_2(r)$ at different frequencies ω_1 and ω_2 are orthogonal: $\left(\frac{\omega_1}{c^2} \right) (H_2, H_1) = (H_2, \Theta H_1) = (\Theta H_2, H_1) = \left(\frac{\omega_2}{c^2} \right) (H_1, H_2)$. Therefore, if ω_1 and ω_2 are different then we have $(H_1, H_2) = 0$. This implies that for two real functions $f(x)$ and $g(x)$ to be orthogonal, we require that: $(f, g) = \int dx f(x)g(x) = 0$. So, fg must be negative as much as positive over the interval for the net integral to vanish.

Written in a form of an eigenvalue problem, Maxwell’s equations show an immediate analogy with the Schroedinger equation for electrons in a periodic potential. In both cases, we decompose the fields in harmonic modes that oscillate with a phase factor $e^{i\omega t}$ and the modes of the system are then determined by a Hermitian eigenvalue equation. In the time-independent Schroedinger wave equation $H\psi(r) = E\psi(r)$, H is the Hamiltonian operator, $\psi(r)$ is the quantum mechanical eigenfunction and E is the energy eigenvalue. The Hamiltonian is given by $-\frac{\hbar^2}{2m} \nabla^2 + V(r)$, where the first term is

the kinetic energy operator and the second is the potential energy. Therefore, one can suggest that the two curls in equation (1.4) correspond roughly to the “kinetic energy” and $\frac{1}{\varepsilon}$ to the “potential” compared to the Schroedinger Hamiltonian [59]. Apart from the similarities, two major differences between the two theories exist: a) the “potential” $\varepsilon(\mathbf{r})$ enters as a multiplication factor, instead of being summed to the free electron Hamiltonian. Unlike an electronic system, where localization was enhanced by lowering the electron energy, lowering the photon energy instead leads to a complete disappearance of the scattering mechanism itself. In addition, the quantity $\frac{\omega^2}{c^2}$, which plays a role analogous to an energy eigenvalue, is always positive thereby precluding the possibility of elementary bound states of light in deep negative potential wells. In other words, if we write the generalized Hermitian eigenproblem in the form for the electric field $\nabla \times \nabla \times E = \left(\frac{\omega^2}{c^2}\right) \varepsilon E$ (1.6) which separates the kinetic and the potential terms, this suggests that electric fields that lie in higher ε , i.e. lower potential, will have lower ω ; b) the Schroedinger wave function is scalar, while the electric and magnetic field have three components that are mixed by the spatial dependent dielectric function.

In addition, one “physical” difference between photonic crystals and conventional crystals is that photons, contrary to electrons, do not have a fundamental length that for electrons is the Bohr radius a_0 . This feature leads to the scaling invariance for the macroscopic Maxwell’s equation. In this sense, we perform the following scale transformation on equation (1.6): $\frac{1}{\alpha}r = r'$ and $\frac{c}{\alpha}t = t'$. The new variables r' and t' are dimensionless [54]. Thus, the photonic crystal can be expanded or reduced via the following transformation $\varepsilon'(s\mathbf{r}) = \varepsilon(\mathbf{r})$, with $s \equiv \frac{1}{\alpha}$ as scaling parameter. Accordingly, we define a new vector field $E'(r', t')$ which satisfies the following wave equation: $\frac{1}{\varepsilon'(r')} \nabla' \times \{ \nabla' \times E'(r', t') \} = -\frac{\partial^2}{\partial t'^2} E'(r', t')$, where ∇' stands for the differentiation with respect to r' . Hence, if the structures of two photonic crystals are similar to each other and their difference is simply the scale of the length, i.e. the lattice constant, then their wave equations are attributed to the same dimensionless wave equation by the scale transformation. Because k and ω have the inverse dimensions of r and t , respectively, the following transformations are necessary: $k' = \frac{\alpha}{2\pi} k$ and $\omega' = \frac{\alpha}{2\pi c} \omega$. Therefore, if we measure the wave vector in units of $\frac{2\pi}{\alpha}$ and the angular frequency in units of $\frac{2\pi c}{\alpha}$, all dispersion curves are the same for those crystals which have simi-

lar dielectric functions. Thus, the eigenfunctions and the eigenvalues of the master equation scale with $\varepsilon(\mathbf{r})$: $H_{k'}(s\mathbf{r}) = H_k(\mathbf{r})$ and $\omega = \frac{\omega}{s}$. In other words, if we want to know the new mode profile after changing the length scale by a factor s , we just scale the old mode and its frequency by the same factor. In this sense, suppose that the bandgap calculated for a given photonic structure is centered at the frequency in dimensionless units $\frac{\omega\alpha}{2\pi c} = \frac{\alpha}{\lambda} = 0.4$. This means that if we want to fabricate a photonic crystal working at telecommunication wavelengths ($1.55\mu\text{m}$), the lattice parameter will be $\alpha = 0.4 * \lambda = 0.4 * 1.55\mu\text{m} = 620\text{nm}$.

1.3 Bloch waves and Brillouin zones

1.3.1 The Photonic Band Structure

In order to solve the electromagnetic problem for a photonic crystal, it is necessary to impose that the dielectric function is periodic $\varepsilon(\mathbf{r}) = \varepsilon(\mathbf{r} + \mathbf{G})$ for some primitive lattice vectors \mathbf{R}_i ($i = 1, 2, 3$ for a crystal periodic in all three dimensions). The dielectric function of a photonic crystal is made of a unit cell repeated in space according to a well defined pattern. Recalling some concepts of solid state physics, the spatial arrangement of the unit cell defines the lattice, whereas the content of the unit cell is specified by the basis. For example, the basis for a three-dimensional photonic crystal can be a dielectric sphere in air or a dielectric cube in air. The lattice is generated by a linear combination of primitive vectors α_i determined by the minimum translations which leave the dielectric function unchanged. Choosing the reference frame and placing the lattice point at the origin of it, any other lattice point is a one-to-one correspondence with a vector \mathbf{R} , a linear combination of α_i : $\mathbf{R} = \sum_i n_i \alpha_i$, ($i = 1, 2, 3$) (1.7). Because ε is a periodic function of the spatial coordinate \mathbf{r} , we can apply Bloch's theorem to the master equation (1.4) and (1.6) as in the case of the electronic wave equation in ordinary crystals with a

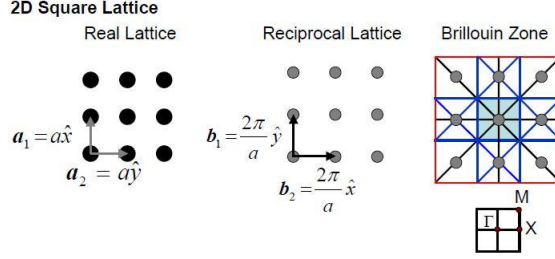


Figure 1.4: Primitive unit cell for square lattice [28]

periodic potential due to the regular array of atoms. $E(r)$ and $H(r)$ are thus characterized by a wave vector k in the first Brillouin zone and a band index n and expressed as $H(r) = e^{ikr} H_{n,k}(r)$, $E(r) = e^{ikr} E_{kn}(r)$ with eigenvalues $\omega_n(k)$ (i.e. a mode consists of a plane wave e^{ikr} modulated by a function that shares the periodicity of the lattice $H_{n,k}(r) = H_{k,n}(r + \alpha_i)$). Moreover, $H_{n,k}$ can also be written in a more compact form as:

$$H_{k,n}(r) = e^{-ikr} \sum c_n(k + G) H_G(r) \quad (1.8)$$

$$H_G(r) = H_G e^{ikr}$$

$$\text{satisfying: } (\nabla + ik) \times \frac{1}{\epsilon} (\nabla + ik) \times H_{n,k} = \left(\frac{\omega_{n,k}(k)}{c} \right)^2 H_{n,k} \quad (1.9)$$

thus, yielding a different Hermitian eigenproblem over the primitive cell of the lattice at each Bloch wavevector k . The eigensolutions are periodic functions of k as well: the solution at k is the same as the solutions at $k + G_i$, where G_i is a primitive reciprocal lattice vector defined by $R * G_i = 2\pi\delta_{i,j}$. Thanks to this periodicity, one needs only to compute the eigensolutions for k within the primitive cell of this reciprocal lattice or, more conventionally, one considers the set of inequivalent wavevectors closest to the $k = 0$ origin, a region called the first Brillouin zone.

Hence, the eigenfunctions of the master equation can be classified by means of the Bloch wave vector k . The Bloch wave vector can also label the corresponding eigenvalues $\frac{\omega^2}{c^2}$. As k varies in the Brillouin zone, the eigenvalues conform to a certain dispersion relation $\omega = \omega(k)$. In fact, it is also possible that two solutions $H_k(r)$ have the same Bloch vector, but different expansion

coefficients $c(k + G)$ in equation (1.9). There are infinite choices for $c(k + B)$ yielding independent linear combinations of the basis functions $H_G(r)$. This means that for each value of k , we expect an infinite set of modes with discretely spaced frequencies, which can be labeled with a band index n . Because of the boundary conditions, we can regard the eigenvalue problem as restricted to a single unit cell of the photonic crystal. This situation is similar to the quantum mechanics problem of the “electron in a box”, where the restriction of the eigenvalue problem to a finite volume leads to discretization of the energy spectrum. In particular, k enters in the master equation only as a parameter, so we expect the frequency of each band, for a given k , to vary continuously as k varies. Thus, the modes of a photonic crystal are a family of continuous functions $\omega_n(k)$, indexed in order of increasing frequency by the band number n . The information contained in these functions is called the *band structure* of the photonic crystal.

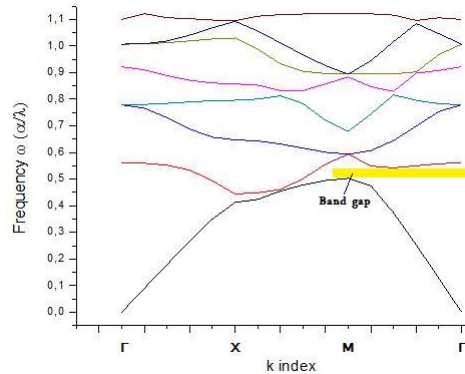


Figure 1.5: Band structure for a square 2D photonic crystal

For example, in figure 1.5, the band structure of a two dimensional photonic crystal with a square symmetry is depicted. The first Brillouin zone, a square, is shown in figure 1.4 as a blue colored area. If a crystal possesses additional symmetries such as mirror planes (rotations, inversion, reflections), the redundant regions are eliminated and one obtains the irreducible Brillouin zone, shown in the inset of figure 1.4 (following the four-fold symmetry of the crystal); the corners (high symmetry points) of this zone are given canonical names, where Γ always denotes the origin $k = 0$. X is the nearest neighbor direction, and M is the next nearest neighbor direction. In general, the wavevector k serves as to specify the phase difference between nearest

neighbor unit cells that are described by $H_{n,k}$. If k is incremented by G , then the phase between cells is incremented by $G * R$, which is a multiple of 2π and not really a phase difference. Also, incrementing k by G results in the same physical mode. Thus, the nearest neighbor unit cell along the x-direction (X: $((0.5 * 2\frac{\pi}{a}), 0)$), is 180 degrees out-of-phase. And, the nearest neighbor unit cell along the diagonal direction (M: $((0.5 * 2\frac{\pi}{a}), (0.5 * 2\frac{\pi}{a}))$), is 180 degrees out-of-phase. The Bloch state $H_k(r)e^{-i\omega t}$ propagates through the crystal without scattering because k is a conserved quantity (apart from an addition of reciprocal lattice vectors, which is merely a relabeling) or, equivalently, all the scattering events are *coherent* and result in the periodic shape of $H_k(r)$ [28]. Furthermore, the Brillouin zone is a two dimensional region of wavevectors, so the bands $\omega_n(k)$ are actually surfaces, but in practice the band extrema almost always occur along the boundaries of the irreducible zone (i.e. the high-symmetry directions). So, the band structure is often calculated along these symmetry lines, because they correspond to higher degree of symmetry with respect to the internal points, and for this reason it is conventional to plot the bands only along these zone boundaries in order to identify the band gap.

1.3.2 The Photonic Band Gap

Thus, a photon with energy ω propagates in a photonic crystal, only if $\exists (k, n) : \omega = \omega(k)$. In this sense, the spectral region $[\omega_1, \omega_2]$ for which $\forall \omega \in [\omega_1, \omega_2], \nexists (k, n) : \omega = \omega(k)$ is called the photonic band gap. The photonic bandgap means that there is null density of states (DOS) $D(\omega)$, which for a photonic crystal is defined as [54]:

$$D(\omega) = \sum_n \sum_{k \in BZ} \delta(\omega - \omega_n(k)) \quad (1.10)$$

In general, the density of states of the radiation field in the volume V of free space is given by $D(\omega) = \frac{\omega^2 V}{\pi^2 c^3}$. The optical properties of atoms and molecules depend on the density of states $D(\omega)$. For example, the rate of spontaneous emission is proportional to $\omega D(\omega)$. Therefore, if we can design and modify the $D(\omega)$, then we can substantially change the optical properties of atoms and molecules. Furthermore, if we introduce a disorder into the regular dielectric structure of the photonic crystal, we obtain midgap modes whose eigenfunctions are strongly localized around the disorder. These modes are called localized defect modes. If the emission frequency of an atom or a

molecule embedded in the photonic crystal lies just in the photonic band gap, the spontaneous emission of a photon from its electronic excited state is completely forbidden, since there exists no photon in the gap [76].

1.3.3 An example: 1D photonic crystal

Returning to the initial point of this section, because $\varepsilon(r)$ is a periodic function it can be expanded into a Fourier series. In the simple case of a 1D photonic crystal, (or a dielectric multilayer) where the x- axis is considered in the direction perpendicular to the surface of the dielectric layers, we have:

$$\varepsilon(x)^{-1} = \sum_n \kappa_n e^{i\frac{2\pi}{\alpha}x} \quad (1.11)$$

$H(x, t)$ can be expressed as a Bloch function $H(x) \equiv H_k(x, t) = H_k(x) e^{i(kx - \omega t)}$, where $H_k(x) = H_k(x + \alpha)$ and, hence, can also be expanded into a Fourier series:

$$H_k(x, t) = \sum H_n e^{i((k + \frac{2\pi}{\alpha})x - i\omega t)} \quad (1.12)$$

where $\{H_n\}$ are the Fourier coefficients. So, if it is assumed that only $n = 0, \pm 1$ are dominant in the Fourier expansion (1.11), we get [54]:

$$\varepsilon(x)^{-1} \simeq \kappa_0 + \kappa_1 e^{i\frac{2\pi n}{\alpha}x} + \kappa_{-1} e^{-i\frac{2\pi n}{\alpha}x}$$

We substitute equations (1.11), (1.12) into the 1D wave equation $\frac{c^2}{\varepsilon(x)} \frac{\partial^2 H}{\partial x^2} = \frac{\partial^2 H}{\partial t^2}$ where we obtain:

$$\kappa_1 \left[k + \frac{2(n-1)\pi}{\alpha} \right]^2 H_{n-1} + \kappa_{-1} \left[k + \frac{2(n+1)\pi}{\alpha} \right]^2 H_{n-1} \simeq \left[\frac{\omega_k^2}{c^2} - \kappa_0 \left(k + \frac{2n\pi}{\alpha} \right)^2 \right] H_n$$

For $n = 0$,

$$H_0 = \frac{c^2}{\omega_k^2 - \kappa_0 c^2 k^2} \left[\kappa_1 \left(k - \frac{2\pi}{\alpha} \right)^2 H_{-1} + \kappa_{-1} \left(k + \frac{2\pi}{\alpha} \right) H_{+1} \right]$$

For $n = -1$,

$$H_{-1} = \frac{c^2}{\omega_k^2 - \kappa_0 c^2 \left(k - \frac{2\pi}{\alpha} \right)^2} \left[\kappa_1 \left(k - \frac{4\pi}{\alpha} \right)^2 H_{-2} + \kappa_{-1} k^2 H_0 \right]$$

Therefore, if $k \simeq |k - \frac{2\pi}{\alpha}|$ (i.e., $k \approx \frac{\pi}{\alpha}$), and if $\omega_k^2 \approx \kappa_0 c^2 k^2$, H_0 and H_{-1} are dominant in the expansion (1.12). In this case, we can neglect all other terms and obtain the following coupled equations:

$$\begin{aligned} (\omega_k^2 - \kappa_0 c^2 k^2) H_0 - \kappa_1 c^2 (k - \frac{2\pi}{\alpha})^2 H_{-1} &= 0 \quad (1.13) \\ -\kappa_{-1} c^2 k^2 H_0 + [\omega_k^2 - \kappa_0 c^2 (k - \frac{2\pi}{\alpha})^2] H_{-1} &= 0 \end{aligned}$$

These linear equations have a non trivial solution when the determinant of the coefficients vanishes:

$$\begin{bmatrix} \omega_k^2 - \kappa_0 c^2 k^2 & -\kappa_1 c^2 (k - \frac{2\pi}{\alpha})^2 \\ -\kappa_{-1} c^2 k^2 & \omega_k^2 - \kappa_0 c^2 (k - \frac{2\pi}{\alpha})^2 \end{bmatrix} = 0$$

If we set $h = k - \frac{\pi}{\alpha}$, the solutions are given by

$$\omega_{\pm} = \frac{\pi c}{\alpha} \sqrt{\kappa_0 \pm |\kappa_1|} \pm \frac{\alpha c}{\pi |\kappa_1|} \left(\kappa_0^2 - \frac{|\kappa_1|}{2} \right) h^2 \quad (1.14)$$

as far as, $|h| \ll \frac{\pi}{\alpha}$. So, there is no mode in the interval

$$\frac{\pi c}{\alpha} \sqrt{\kappa_0 - |\kappa_1|} < \omega < \frac{\pi c}{\alpha} \sqrt{\kappa_0 + |\kappa_1|} \quad (1.15)$$

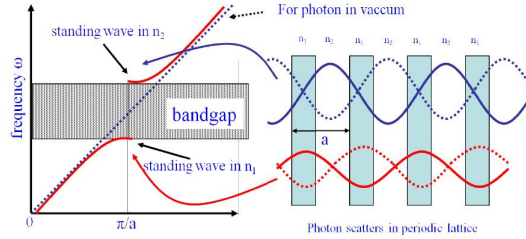


Figure 1.6: Dispersion relation

This gap disappears when $\kappa_1 = 0$, i.e., when there is no spatial modulation in the dielectric function. In addition, if two dispersion lines cross each other, a frequency gap appears. These are schematically shown in figure 1.6. The dispersion relation for 1D photonic crystal is shown with red solid lines. The boundary of the first Brillouin zone is denoted by the vertical thin line. The electromagnetic wave incidents from one side and is reflected at each interface of n_1 and n_2 . If the periodicity of the crystal and the frequency of the incident wave is such that all the reflected waves generated at each interface

interfere constructively, then they will be summed up until they cancel the incoming wave. Hence, forbidden frequency or energy intervals appear as a consequence of interference which must be destructive in all directions. The vectorial nature of the electromagnetic field, however, requires three instead of one interference condition which poses additional restrictions on the symmetry of the crystal and the values of the parameters. In particular, the fcc structure seems to be favorable to develop a photonic band gap as the BZ defined earlier is most “spherelike” [75].

Furthermore, the group velocity of the radiational eigenmode is given by the slope of the dispersion relation $u_g = \frac{\partial \omega(k)}{\partial k}$. From equation (1.14), we can notice that for $k \rightarrow \frac{\pi}{\alpha}$, $h \rightarrow 0$, hence also $u_g \rightarrow 0$. This means that the eigenmodes near the Brillouin zone’s edge are not travelling modes but standing waves. The confined modes, i.e. the standing waves stored in n_1 and n_2 , correspond to the photonic band gap edge frequencies with zero group velocities. In this sense, referring back to the density of states, for photons is defined so that the number of states $N(\omega)$ within the frequency region $[\omega, \omega + \Delta\omega]$ of an infinitesimally small interval $\Delta\omega$ is given by: $N(\omega) = \rho(\omega) \Delta(\omega)$ [25]. Since k is quantized by the spacing $\frac{2\pi}{\alpha}$, where α is the size of the 1D system, the number $N(\omega)$ should be equal to the number of allowed k values within the interval Δk determined by the prescribed allowance $\Delta(\omega)$. For an infinitesimally small interval $\Delta(\omega)$, we have: $\Delta(\omega) = \frac{\partial \omega_n(k)}{\partial k} \Delta k$, or $\Delta k = \left(\frac{\partial \omega_n(k)}{\partial k}\right)^{-1} \Delta\omega$. Dividing Δk by the spacing $\frac{2\pi}{\alpha}$ of the quantization yields $N(\omega)$. Therefore, we have: $D(\omega) = 2\frac{\alpha}{2\pi} \left(\frac{\partial \omega_n(k)}{\partial k}\right)^{-1}$. The DOS is, thus, related to the inverse of the group velocity u_g because $\Delta\omega$ increases as the curvature of the dispersion curve decreases. The prefactor two accounts for the two polarizations of photons propagating in the x-direction. At the frequencies of the bands near the Brillouin zone edge, where the group velocity u_g of the bands 1, 2, ... vanishes, peaks arise in the DOS. Enhanced density of states, is one of the characteristics of photonic crystals. The emission probability of photons of frequency ω from an atom is proportional to $D(\omega)$. It is therefore, natural to expect enhanced light emission from atoms at the frequency of the DOS peaks. The enhancement of the density of states is called the group velocity anomaly. On the other hand, suppression of the DOS occurs in the photonic band gap (region with zero DOS). In this region, we have a zero emission rate of photons from an atom.

1.4 Refraction law for Photonic Crystals

1.4.1 Refraction at an interface

As shown in the previous section, the band structure provides the band and the gaps along the symmetry directions of the photonic crystal lattice. The band structure gives the regions where the propagation is prohibited or allowed. However, in the band regions the band structure does not provide any information about how the wave will propagate inside the structure. The band diagrams in the photonic crystal system, just like the electronic system, are in terms of the wave vector in the first Brillouin zone. An important difference between the electronic system and the photonic system is that although electrons are present in the crystal, the EM waves couple into the crystal from outside. Consequently, in the photonic crystal the wave vector cannot take any value and is subject to the boundary conditions.

Now, consider the case that a light beam is travelling through different media. How is an incoming plane wave refracted at the surface of the photonic crystal? If the medium is a dielectric material, then we observe conventional refraction phenomenon. If the medium is a diffraction grating, then we observe diffraction phenomenon. If the medium is a photonic crystal, then the kind of phenomena observed for light propagation is more complicated. As already mentioned in a previous section, light propagation in photonic crystals is represented by Bloch waves in a similar way to plane waves in a continuous material. Bloch waves have a definite propagation direction in spite of strong scattering by the periodic structure, though, their propagation is complicated because it is influenced by the band structure [45]. This characteristic leads one to consider a geometrical optic approach to understand the propagation.

The simplest case is the one that a photon with energy ω propagates in a 1-dimensional photonic crystal. Thus, a mode with wavevector k_1 and frequency $\omega_1 (= \omega(k_1))$ in a region external to the photonic crystal can be coupled to one with k_2 and ω_2 in the photonic crystal. The spatial dispersion $\omega_2(k_2)$ is determined by the photonic band structure. Because the system has translation symmetry in a direction parallel to the interface, the wave vector in that direction should be conserved when the refraction and the reflection take place. Conservation of both the energy and the wavevector

component parallel to the surface k_{\parallel} gives us: $\omega_1 = \omega_2$ (1.16a) and $k_1 = k_2$ (1.16b).

In the general case of refraction at the interface of two uniform materials with $n_1 > n_2$ (eg. glass-air), the propagation of electromagnetic modes in a dielectric medium with dielectric permittivity ε is described by the phase refractive index (dispersion relation) and Snell's law:

$$\omega = \frac{ck}{\sqrt{\varepsilon}} = c \frac{\sqrt{k_{\parallel}^2 + k_{\perp}^2}}{\sqrt{\varepsilon}} \quad (1.17)$$

$$k_{\parallel} = |k| \sin \theta, \quad |k| = n \frac{\omega}{c}$$

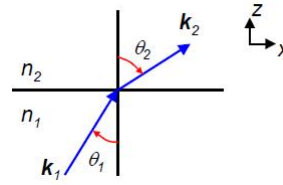


Figure 1.7: Snell's law

These relations are derived from the fact that the equi-phase planes of the relevant waves should have the same spacing along the interface. Equation (1.17) for a one dimensional system depicts a line $\omega = \frac{c}{n} k_{\parallel} = \frac{c}{n} k_x$, called *the light line*, whereas for a two dimensional system it depicts a cone $\omega = \frac{c}{n} k_{\parallel} = \frac{c}{n} \sqrt{k_x^2 + k_y^2}$, called *the light cone* [25]. The light cone divides the phase space (ω, k_{\parallel}) into two parts based on equations (1.16a), (1.16b). Let's say, now, that in medium 1 we have a mode at point A. The magnitude of k of the mode with the k_{\parallel} component is given by:

$$\omega = \frac{c}{n_1} |k_{\parallel}| \quad (1.18)$$

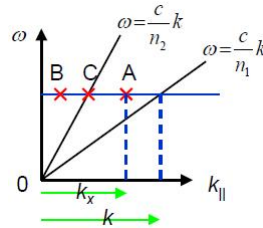


Figure 1.8: The light line [25]

Therefore, the mode is one propagating with an angle θ_1 such that:

$$\sin \theta_1 = \frac{k_{\parallel}}{k} = \frac{k_x}{\left(\frac{n_1 \omega}{c}\right)} \quad (1.19)$$

Hence, all modes in the medium are to the left of the light line for that medium. Therefore, light that is incident on the boundary plane with ω and k_{\parallel} on the left-hand side of the light line of medium 2 (e.g. point B) can go inside medium 2 with a refraction angle θ_2 given by:

$$\sin\theta_2 = \frac{k_{\parallel}}{k} = \frac{k_x}{\left(\frac{n_2\omega}{c}\right)} \quad (1.20)$$

Light with ω and k_{\parallel} on the right-hand side of the light line of medium 2 (e.g. point A) cannot go inside medium 2. It is totally internally reflected in medium 1. The critical angle is therefore given by the light line of medium 2. To find the critical angle we take the light line in medium 2, so that k_x is given by: $k_x = n_2 \frac{\omega}{c}$. Substituting this into equation (1.19) allows us to find the critical angle for total internal reflection for light incident from medium 1 into medium 2:

$$\sin\theta_c = \sin\theta_1 = \frac{k_{\parallel}}{k} = \frac{k_x}{\left(\frac{n_1\omega}{c}\right)} = \left(\frac{\frac{n_2\omega}{c}}{\frac{n_1\omega}{c}}\right) = \frac{n_2}{n_1} \quad (1.21)$$

This may also be directly found from Snell's Law. Therefore, the modes in the light cone are solutions of Snell's Law (less than the critical angle). In addition to the light cone, the glass plate introduces new electromagnetic solutions that lie below the light line ($\omega = ck_{\parallel}$). Because ε is larger in the glass than in air, these modes have lower frequencies relative to the values the corresponding modes would have in free space. These new solutions must be localized in the vicinity of the glass. Below the light line the only solutions in air are those with imaginary $k_{\perp} = \pm i\sqrt{k_{\parallel}^2 - \frac{\omega^2}{c^2}}$, fields that decay exponentially away from the glass: index guided modes in the glass. So for a given k_{\parallel} they form a set of discrete frequencies, because they are localized in one direction, $\omega_n(k_{\parallel})$ below the light line. In the limit of larger and larger k_{\parallel} one obtains more and more guided bands, and eventually one approaches the ray optics limit of totally internally reflected rays with a continuum of angles $\theta > \theta_c$. The main remark here is that the introduction of the continuity conditions on the border of dielectric regions for the propagation of electromagnetic fields in a dielectric plate, modifies the dispersion relation. Two different regions appear, the first corresponds to a discrete number of guided modes, the second to a continuum of modes that extend over all the volume.

1.4.2 Group velocity and Equiphase surfaces

Apart from the continuity conditions and energy conservation at the interface, there are several other parameters that characterize beam propagation in photonic crystals, among them is the *wave velocity*. In contrast to the case of particles for which the velocity has a single meaning, waves have three different kinds of velocities, i.e. the phase velocity, the group velocity and the energy velocity [54]. These velocities are equal to each other in uniform materials with refractive indices which are real and independent of the frequency. The phase velocity, $u_{ph} = \frac{\omega}{k}$, is defined as the velocity of the propagation of an equi-phase surface. This velocity has a definite meaning for a plane wave or spherical wave for which the equi-phase surfaces cannot be defined rigorously. In the photonic crystal case, since its eigenfunction is a superposition of plane waves, the phase velocity cannot be defined appropriately. Inside the photonic crystal the phase velocity cannot be considered because the equi-phase surface does not exist inside the periodic structure. On the other hand, the group velocity which is the velocity of the propagation of a wave packet can be defined as $u_g = \frac{\partial\omega}{\partial k(\omega)}$. The energy velocity is defined as the velocity of propagation of the electromagnetic energy. The propagation of the electromagnetic energy is described by Poynting's vector ($S_{kn}(r) = \frac{1}{2}Re[E_{kn}(r) \times H_{kn}^*(r)]$), so that the energy velocity is equal to the ratio of the time average Poynting vector to the time average electromagnetic energy density ($u_e = \frac{\langle S_{kn}(r) \rangle}{\langle U_{kn}(r) \rangle}$). Hence, the velocity inside the periodic structure may be considered as the group velocity or the energy velocity. The group velocity is equal to the energy velocity even though the dielectric constant is modulated periodically.

Therefore, the propagation directions of light in photonic crystals are determined by analyzing the directions of the group velocity via the wave-vector diagrams [74]. The wave vector diagrams consist of the equifrequency surfaces obtained by calculating the photonic band structures within the first Brillouin zone in all directions (equifrequency surface is a surface/contour in 2D that consists of all the allowed wave vectors within the first Brillouin zone for a certain frequency); the propagation wave vectors are obtained through the momentum conservation rule, i.e. the continuity condition between the incident and the propagation wave vectors (the wave-vector component parallel to the incident crystal edge conserved); the propagation directions (i.e., the group velocity) are obtained by calculating the normal of the equifre-

quency surface curve at the end point of the propagation wave vector. Thus, one first calculates the dispersion relation of the wavelength on the wave vector in the first Brillouin zone. The equifrequency surface is obtained by picking k points corresponding to the selected frequency in the first Brillouin zone. The group velocity is calculated by the formula previously given ($u_g = \frac{\partial \omega}{\partial k(\omega)}$).

Thus, the wave vector diagram, in this case, is nothing but the graphical representation of Snell's law. As mentioned previously, equation (1.17) for a two dimensional system depicts a cone $\omega = \frac{c}{n} k_{\parallel} = \frac{c}{n} \sqrt{k_x^2 + k_y^2}$, called *the light cone*. Thus, the intersection of the equifrequency surface with the plane of incidence is always a circle with radius equal to $n \frac{\omega}{c}$, where n is the refractive index and ω is the frequency (figure 1.9). The k vector in the dielectric medium is determined by the continuity of tangential components of the k vector across the interface ($k_1 = k_2$), and energy conservation ($\omega_1 = \omega_2$) determines that light always propagate parallel to the k vector. Hence, in this case, the direction in which

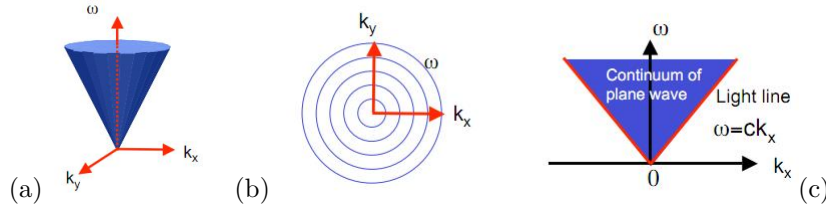


Figure 1.9: a) The light cone, b) Equifrequency surface and c) the light line

the radiational energy of the plane wave flows coincides with the direction of its wave vector. In this sense, in figure 1.10, the blue circle represents the equifrequency surface in air, the orange circle represents the equifrequency surface in the dielectric slab, and the yellow vertical line represents the conservation of the parallel component of the incident wave vector. There are two choices for the wave vector inside the dielectric medium, either to point towards A or to point towards B. The additional constraint comes from requiring the direction of the flow inside the dielectric to be causal, i.e. to point away from the source. For $S * k$ to be positive, the appropriate choice for the wavevector inside the crystal (black arrow) would be to point towards point B. The direction of the wave vector in this case is the direction of the pointing vector (pale arrow) [15], [16].

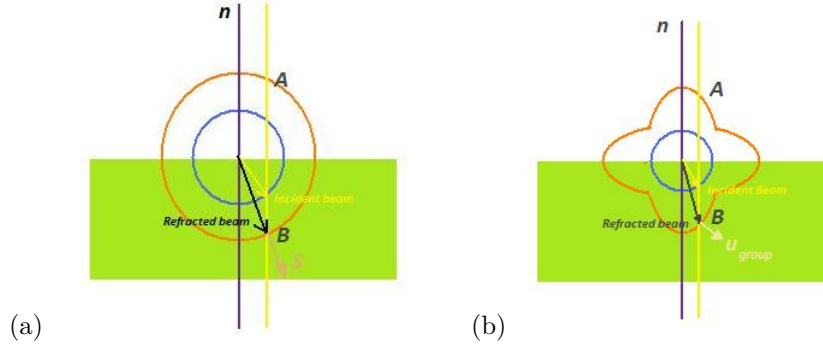


Figure 1.10: Refraction at an interface a) air - dielectric, b) air - photonic crystal

The same principles are applied in determining the refractive behavior of the periodic medium. However, there are several differences between the homogenous medium and a periodic medium. First, the equifrequency surfaces repeat themselves periodically in space, so that the parallel component of the wave vector should be conserved with the allowance for the difference of a multiple of $\frac{2\pi}{\alpha}$. Moreover, the equifrequency surfaces modes are usually not circular and can have a quite complicated shape which leads to marked differences. The wave vector of the refracted wave has its end-point on the equifrequency surface given by the band structure $\omega = \omega(k_2)$. This condition determines the wave vector of the refracted wave. For the present case, the group velocity, and thus the energy velocity of the incident and refracted waves energy are given by $u_i = \nabla_{k_i} \omega = \frac{c}{n} \hat{k}_i$, where \hat{k}_i denotes the unit vector parallel to k_i . Hence, the direction of the energy flow coincides with the direction of the wave vector. Moreover, its direction is perpendicular to the equifrequency surface given by $\omega = constant$. This means that the group velocity is perpendicular at a certain point of the equifrequency surfaces and points towards increasing values of frequency. Thus, it points outwards for a band with positive curvature and inwards for a band with negative curvature. Since group velocity and energy velocity are equal, the group velocity vector shows the direction of $\langle S \rangle$, i.e., the direction of the propagating signal. Then, in the periodic medium, the spatial average of the time-averaged Poynting vector defines the propagation direction rather than the Poynting vector itself. Moreover, the directional relation between $\langle S \rangle$ and the wave vector is not necessarily parallel or antiparallel. In general, $\langle S \rangle$ is at an acute or obtuse angle with k . When the former is the case, $\langle S \rangle \cdot k > 0$,

and we have forward (“right-handed”) propagation. When the latter is the case, we have $\langle S \rangle \cdot k < 0$, and we have (“left-handed”) propagation. So, in figure 1.10b, we assume that the equifrequency surface (star-like curve) corresponds to a band with positive curvature. As before, the blue circle is the equifrequency in air and the yellow vertical line represents the parallel component of the incident wave vector. The refracted wave vector inside the crystal at point B (black vector) corresponds to a group velocity indicated with the pale arrow. The latter points away from the source and represents the direction of the propagation signal. Because of the complex dependence of ω on k_2 , curious phenomena can occur [[45]], [[77]].

In this sense, photonic crystals without a complete PBG can be designed to obtain supercollimators and super-lenses, known as the super-prism effect. Two photons that impinge a photonic crystal with the same angle but a slightly different energy, may find EFSs with a very different curvature. As a consequence their propagation angles would be very dissimilar [35]. In addition, all-angle negative refraction can be used to obtain super-lenses that could potentially overcome the diffraction limit inherent in conventional lenses [42], [49],[41].

1.4.3 Bragg Diffraction

In the general case where an incident plane wave strikes an interface of a photonic crystal, some of the light will be reflected at an angle equal to the incident angle, or outside the photonic band gap some of the light will be transmitted or refracted, propagating at some angle (of the group velocity) within the crystal. Depending upon the frequency, the interface periodicity and the band structure, there may be additional reflected and/or refracted waves, a Bragg diffraction phenomenon [28]. In the context of scattering from periodic structures, diffraction refers in unusual reflected/refracted waves that arise because of the special case that $\lambda/2$ is comparable to or smaller than the periodicity. As mentioned previously in this section, due to energy and momentum conservation at the interface, the wave vector parallel to the interface k_{\parallel} is conserved as light propagates due to addition of reciprocal lattice vectors. Suppose that the periodicity parallel to the interface is Λ , and the incident plane wave has wave vector $(k_{\parallel}, k_{\perp})$ and frequency ω . Then, any reflected or refracted wave must also have frequency ω and a wave vector $(k_{\parallel} + \frac{2\pi l}{\Lambda}, k'_{\perp})$ for any integer l and some k'_{\perp} . Note that the periodicity Λ of

the interface need not be the same as the lattice constant of the crystal. For example, in the case of a square lattice with period a , the diagonal (110) interface has period $\Lambda = a\sqrt{2}$. Indeed, the interface need not be periodic at all. The periodic interface orientations are the lattice planes, where every lattice plane is normal to some reciprocal lattice vector. The lattice planes are typically described by Miller indices.

So, in the case of reflection, the specular reflected wave corresponds to $l = 0$, that is, a plane wave with $k = (k_{\parallel}, k_{\perp})$. Moreover, suppose that the incident medium has a refractive index $\frac{n_i\omega^2}{c^2} = k_{\parallel}^2 + k_{\perp}^2 = k_{\parallel}^2 + (k'_{\perp})^2$. It follows that $k'_{\perp} = \pm k_{\perp}$ and because the reflected wave must be propagating away from the interface, we choose $k'_{\perp} = -k_{\perp}$. The existence of $l \neq 0$ diffractive reflections depends on the frequency. Conservation of ω means that, in general, $k'_{\perp} = -\sqrt{\frac{n_i\omega^2}{c^2} - \left(k_{\parallel} + \frac{2\pi l}{\Lambda}\right)^2}$. From this equation, however, it is clear that if ω is too small or if l is too large, then k'_{\perp} , for $l \neq 0$ will be imaginary, corresponding to an evanescent field that decays exponentially away from the interface. We will obtain a non-evanescent diffractive reflection at l only for $\omega > \frac{c}{n_i} |k_{\parallel} + \frac{2\pi l}{\Lambda}|$.

1.5 The Woodpile structure

In the present thesis, we will focus on three dimensional photonic crystals and in particular on the so-called woodpile structure [23] that is favorable for layer by layer fabrication. A woodpile structure is shown in figure 1.11a. It consists of layers of dielectric rods with a stacking sequence that repeats itself every four layers with a repeat distance of c . Within each layer, the rods are arranged with axes parallel and separated by distance, d . The orientations of the axes are rotated by 90 degrees between adjacent layers. To obtain a periodicity of four layers in the stacking direction, the rods of the second neighbour layers are shifted by a distance of $0.5d$ in the direction perpendicular to the rod axes. For the particular case of $\frac{c}{d} = 1.414$, the lattice can be considered as an FCC primitive unit cell with a basis of two rods. Otherwise, the lattice symmetry is a face centered tetragonal (FCT). If we define the z-axis to lie along the stacking direction and the x- and y-axes to be at 45 degrees to the axes of the rods within the layers, the layered structure can be derived from the diamond

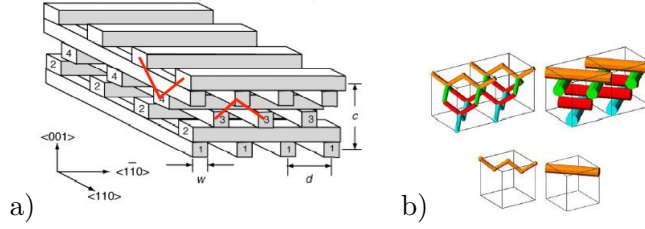


Figure 1.11: The woodpile structure [23]

lattice by replacing the (110) chains in the diamond structure by these rods. In other words, the photonic structure can be derived from the zinc-blende crystal lattice by replacing the sulfur-center of the tetraeder sites at

$$\left(\frac{3}{4}, \frac{1}{4}, \frac{1}{4}\right), \left(\frac{1}{4}, \frac{3}{4}, \frac{1}{4}\right), \left(\frac{1}{4}, \frac{1}{4}, \frac{3}{4}\right), \left(\frac{3}{4}, \frac{3}{4}, \frac{3}{4}\right)$$

by the $[\bar{1}\bar{1}0]$ line pattern and replacing the zinc-edges of the tetraeder sites by the $[110]$ crossed line pattern [34]. This is shown schematically in figure 1.11b, where short dielectric rods are replaced by an equivalent large horizontal rod. The inset shows the replacing of four short rods by a large rod at the top layer. The ratio of the height, c , of the layer in the z -direction to the repeat distance, d , along the layer can be varied to optimize the gap, whereas the cross-sectional changes of the rods (circular, elliptical or rectangular) are not critical to the performance of the structure. In addition, the rods between two layers can be touching each other or can overlap to a certain extent. In fact, the authors have calculated that when the refractive index of the rods is $n = 3.6$, the woodpile structure possesses a maximum $\sim 18\%$ photonic band gap at dielectric volume fraction $f \sim 0.28$ [22]. The circular, elliptical and rectangular dielectric rods give roughly the same results, if the filling ratio ($f = \frac{w}{d}$) -which determines the radius of the rods, the refractive index, n , and the ratio $\frac{c}{d}$ are kept constant. The structure presents a complete photonic band gap located between the second and third band. Lin et al [38] were the first to demonstrate such a structure experimentally. The crystal fabricated on a silicon wafer having a refractive index $n = 3.6$, filling ratio $f = 0.28$ and $\frac{c}{d} = 1.414$ showed a large stop band at $(10 - 14.5) \mu m$ along the $\langle 001 \rangle$ direction.

Generally speaking, the woodpile structure belongs to a broader class of structures, known as the A7 family [5]. This 'parent' structure has a rhombohedral lattice and a basis of two atoms. The primitive translation vectors are given by

$$\begin{aligned} \vec{a}_1 &= a_0 \{\epsilon, 1, 1\} \\ \vec{a}_2 &= a_0 \{1, \epsilon, 1\} \\ \vec{a}_3 &= a_0 \{1, 1, \epsilon\} \end{aligned} \quad (1.22)$$

such that

$$\epsilon = \left[\frac{1 - (1 + \cos\alpha - 2\cos^2\alpha)^{\frac{1}{2}}}{\cos\alpha} \right] \quad (1.23)$$

where α is the angle between any two primitive vectors. The two basis atoms are positioned at $d = \pm u (\vec{a}_1 + \vec{a}_2 + \vec{a}_3)$. For photonic crystals, the term 'atom' is better described by the term 'site' and for our structures these positions are where the rods meet, and thus called 'joints'. In other words, the 'lattice points' of the woodpile structure are represented by the cross-sections of the rods, with the rods connecting nearest neighbor sites. By varying, α and u , a whole series of photonic crystals are generated. In particular, the diamond structure corresponds to $u = \frac{1}{8}$ and $\alpha = 60^\circ$. Thus,

$$\epsilon = 0, \quad \begin{aligned} \vec{a}_1 &= a_0 \{0, 1, 1\} \\ \vec{a}_2 &= a_0 \{1, 0, 1\} \\ \vec{a}_3 &= a_0 \{1, 1, 0\} \end{aligned}, \quad d = \pm \frac{1}{4} a_0 (1, 1, 1) \quad (1.24)$$

2 Chapter 2: 3D Fabrication of Photonic nanostructures

Direct writing using a tightly focused femtosecond laser beam exploits the nonlinear absorption induced by intense irradiation to provide a well controllable tool for the creation of spatially defined structures. Since the absorption takes place at high irradiance regions i.e. at the beam focus, the induced photo-polymerization is restricted within the focal volume of a photosensitive resin. 3D features are obtained by translating the focal spot in the bulk of such a transparent material. The size of the polymerized voxel can be controlled by a variation of laser power and irradiation time and can be as small as 120nm when fabricated near threshold for two-photon absorption. These basic concepts are extensively discussed throughout the present chapter.

2.1 Direct laser writing

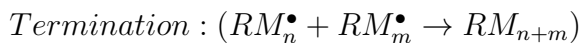
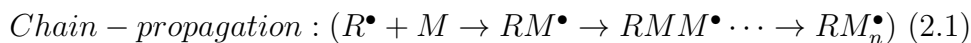
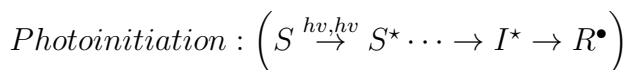
High resolution three-dimensional (3D) optical structuring of materials is an actively developing area of fundamental and applied materials research. The advent of high-power ultrafast picosecond and femtosecond lasers has resulted in high-quality nano-/micro structures defined with high spatial resolution. Since shorter pulses invoke stronger nonlinearities, more efficient and better-localized photomodification of 3D materials is induced. So far, the resolution of features fabricated with conventional photolithographic methods is limited by optical diffraction, and also require expensive photomasks or transparent molds. In addition, most of the processes developed do not enable the fabrication of arbitrary 3D microstructures. Contrary to those constraints, two photon polymerization induced with a femtosecond laser presents many advantages as a technique for the direct fabrication of complex 3D structures on a scale of several microns. A femtosecond laser pulse is closely focused onto liquid-state monomers and the resulting two-photon polymerization used to initiate chemical processes and the formation of features close to 100nm in size. After laser irradiation, the material resins undergo a significant phase transition from liquid to solid as a result of the absorption of the threshold energy for polymerization. The two-photon absorption probability depends quadratically on intensity, and therefore under tight-focusing conditions, the absorption is confined at the focal volume. Hence, a submicron to 100nm resolution can be obtained using a high numerical aperture (NA) objective

lens. After polymerization, the non-polymerized liquid is easily removed by a developing process, so that solidified structures stand out.

2.1.1 Polymerization by two - photon absorption

Polymerization refers to the process of using light as an energy source to induce the conversion of small unsaturated molecules in the liquid state to solid macromolecules through polymerization reactions. In particular, polymerization deals with those curing reactions that are induced by light in the UV and visible to IR spectral regions. The basic components of the starting liquid material are monomers, that upon light excitation are solidified by means of a chain reaction polymerization leading to the creation of macromolecules. In general, the quantum yield of monomers, which is defined as the ratio of number of polymerized monomer units to the number of photons that are needed to cause the polymerization, is low. In order to increase the initiating efficiency, one or several low-weight molecules that are more sensitive to light irradiation are added. Such small molecules are called photoinitiators (I). Efficient two photon chromophores are also generally used to enhance two-photon activation, called photosensitizers (S). They are molecules that absorb light and then transfer the energy to a photoinitiator.

The photopolymerization process consists of the following steps: a) photoinitiation, b) chain propagation and c) termination. During photoinitiation, the photosensitizer chromophore is excited by the simultaneous absorption of two photons, then emits fluorescent light in the UV-vis regime:



Next, photoinitiators with good chemical reactivity absorb the fluorescent light and form initiating species of radicals (R^\bullet)(initiation). The photo-produced radicals react with monomers (M), producing monomer radicals (RM^\bullet), which combine with new monomers. The monomer radicals expand in a chain reaction (propagation), until two radicals meet each other

(termination). The intermediate excited state of the initiator and the photosensitizer after absorbing the photon energy is denoted by (I^*) and (S^*), respectively.

The above descriptions of polymerization are based on radical initiators. In general, polymerization reactions are classified into two categories: radical polymerization and ionic polymerization. In the case of the radical type, polymerization reactions are based upon double-bond addition of acrylates.

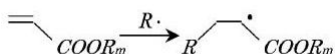


Figure 2.1: Double-bond addition of acrylates

The most efficient radical initiators work via bond cleavage. For this type of reaction, the radical type initiator commonly used is benzoyl, since this chromophore exhibits good absorption in the UV region.



Figure 2.2: Bond cleavage

After polymerization, the monomer constitutes the backbone of the polymer network. The physical, chemical and mechanical properties of the solidified resin depend on the nature and structure of the monomer.

2.1.2 Photo-polymerization via two-photon absorption

Two-photon absorption is a multiphoton excitation process for the initiation of photochemical changes. Two different mechanisms of two-photon absorption exists: sequential excitation and simultaneous two-photon excitation [37]. The former relies on the excitation of the absorbing species to a real intermediate state. This first excited state becomes populated by the first absorbed photon and has a well defined lifetime of 10^{-4} to 10^{-9} sec; this state then absorbs a second photon of the same energy as shown in figure 1.16. In the latter case, an electron absorbs two photons *simultaneously* to transcend the gap in one excitation event. There is no real intermediate state, but a virtual state is created by the interaction of the absorbing species with the

first photon. It persists for a very short duration of the order of several femtoseconds (as defined by Heisenberg's Uncertainty Principle), contrary to the long lifetime of the actual intermediate energy level in sequential absorption. Therefore, only if the second photon arrives within the virtual state lifetime will it be absorbed. Hence, higher intensities are required for the latter case to occur. Since, the two-photon absorption probability depends quadratically on laser intensity, multiphoton absorption is confined to a small 3D volume in the vicinity of the laser beam focus, where the intensity distribution for a gaussian beam is higher.

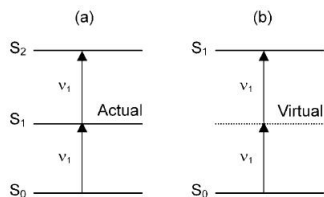
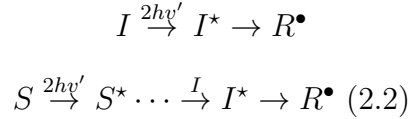


Figure 2.3: Two-photon absorption mechanism [61]:
a) sequential, b) simultaneous excitation

In the case of two-photon absorption, two photons, each with half the energy of the gap between the two energy levels, induce the electron transition. In figure 1.16, the energy of the incident photon is given by $h\nu$, where ν is the frequency of the incident light. The absorbing species is raised to an excited state when it absorbs the energy of the single photon, which is equal to $h\nu = E_1 - E_0$, where E_0 and E_1 are the energy levels ($E_0 < E_1$) of the absorbing species.

Ti:sapphire lasers are widely used for inducing two-photon absorption because they produce ultrahigh peak power with a very short pulse width of approximately 100fsec. The field strength is sufficiently intense to induce direct bond breaking. Furthermore, for many dielectric materials, there is a transparent window in the red-NIR spectral region, which is covered neither by electronic band-band absorption nor by atomic/molecular oscillation absorption. The central wavelength of these lasers is located in this region, approximately at 800nm, which is close to half the photon energy for polymerization. Therefore, a femtosecond laser can penetrate into transparent materials, tailor real 3D structures thus providing an easy control close to the polymerization threshold energy.

In fact, the way that the energy for activating initiators is provided makes the difference between two-photon and one-photon photo-polymerization. In the former case, initiators are excited to triplet states by absorbing combined two-photon energy, so that the photo-initiation part of polymerization can be rewritten as [37] :



where $\nu' \sim \frac{\nu}{2}$ denotes photon frequency in the two-photon excitation beam. This is shown schematically below: the valence electrons of the photoinitiators are excited from the ground state (S_0) to the first excited (S_1) singlet state by simultaneously absorbing two photons. The excited electrons then relax by transition to triplet state (T_1) via intersystem crossing, where the photoinitiator undergoes bond cleavages, producing radicals for polymerization. The excited states can also be relaxed via radiative processes such as fluorescence emission from singlet states (F) or phosphorescence emission from triplet states (P). Though, due to a long excited-state lifetime, the triplet state is the major transient state that is responsible for the generation of radicals. Two kinds of triplet states are exhibited in the carbonyl group contained in the photoinitiators : $\pi\pi^*$ and $n\pi^*$. According to the selection rules of electronic transition, $n \rightarrow \pi^*$ transitions are symmetry forbidden and $\pi \rightarrow \pi^*$ transition are symmetry allowed. Therefore, the molar extinction coefficient of the $n \rightarrow \pi^*$ transition is much smaller than that of the $\pi \rightarrow \pi^*$ [61].

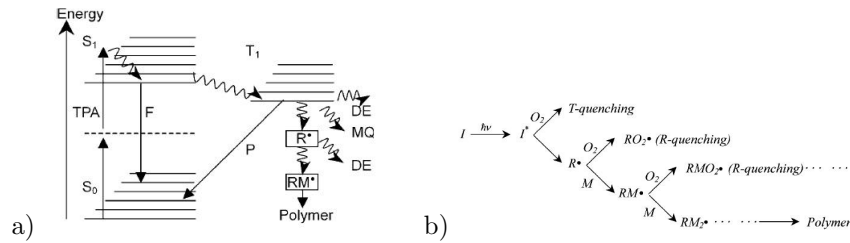


Figure 2.4: a) Activation mechanism during photoinitiation [61],
b) Quenching mechanism [61]

In addition, both the triplet state and the photoproducted radicals can be deactivated by monomer quenching (MQ) for the former, and by radical quenching (RQ) for the latter. In radical type photo-polymerization, the oxygen molecules quench polymerization via two possible routes: a) triplet state quenching, where the triplet state of the initiator molecules are consumed by reacting with oxygen molecules without generating radicals; b) radical quenching (R-quenching), where radicals combine with oxygen molecules, producing much less active radicals. The radical quenching effect is the major factor for sub-diffraction limit fabrication, since it prohibits photo-polymerization reactions.

2.1.3 Resolution limits

The resolution of microstructures fabricated with two photon polymerization is determined by the size of the voxels. There are several factors determining the resolution limits of 3D material treatment with femtosecond lasers. Mainly, laser and material characteristics define how close one can approach to the two-photon polymerization threshold, but also classical resolution limits set by the laser wavelength and by the numerical aperture (NA) of the imaging optics. The last limit is defined by the following expressions :

$$cd = \frac{k_1 \lambda}{\sqrt{q} NA} \text{ and } dof = \frac{k_2 n \lambda}{\sqrt{q} NA^2} \quad (2.3)$$

where cd is the critical dimension of the printed structure, dof is the depth-of-focus, i.e. the axial structure dimension, λ is the wavelength of the laser, NA is the numerical aperture of the objective, q is the order of the multiphoton process ($q = 2$ for two-photon polymerization) and n is the immersion oil refractive index usually used for high numerical aperture microscope objectives. For the case of two-photon absorption and for a laser wavelength centered at 800nm, we get: $cd = 0.61 \frac{\lambda}{NA} = 348nm$, and $dof = \frac{2\lambda n_{oil}}{NA^2} = 1.2\mu m$. For all photosensitive materials, a threshold irradiation fluence (and/or irradiation time) exists, which has to be overcome in order to initiate polymerization. Due to this well defined polymerization threshold, one can reach a resolution far beyond the diffraction limit, as illustrated below for a Gaussian laser pulse.

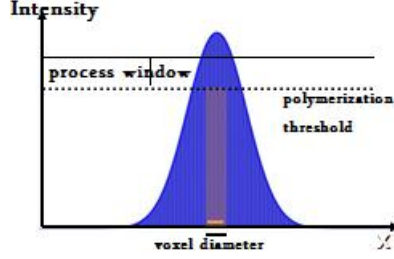


Figure 2.5: Intensity distribution and polymerization threshold [?]

The density of radicals (ρ) produced by the femtosecond laser pulses in the polymerization process varies with the square of the beam intensity [55]:

$$\frac{\partial \rho}{\partial t} = (\rho_0 - \rho) \delta I^2 \quad (2.4)$$

where δ is the effective two-photon cross section for the generation of radicals, I is the intensity distribution of the laser beam (assumed to be Gaussian) and can be expressed as:

$$I(r_0, 0) = I_0 e^{-\frac{2r_0^2}{w_0^2}} \quad (2.5)$$

where r_0 , I_0 and w_0 are the radius of the beam, the beam intensity at the central axis in the focus plane, and the radius of the beam spot respectively. Combining equations (2.4) and (2.5), we get for the voxel size d generated by two-photon polymerization (as long as $\rho > \rho_{th}$):

$$d(I_0, t) = r_0 \sqrt{\ln\left(\frac{\delta I_0^2 n \tau_L}{C}\right)}, \quad C = \ln\left(\frac{\rho_0}{\rho_0 - \rho_{th}}\right) \quad (2.6)$$

where n is the number of pulses, t is the total irradiation time, and τ_L is the laser-pulse duration. Using the same expression for the axial light distribution at $r = 0$, as for a Gaussian beam $I(z) = \frac{I_0}{1 + (\frac{z}{z_0})^2}$, the pixel length can be determined by

$$l(I_0, t) = 2z_R \sqrt{\sqrt{\frac{\delta I_0^2 n \tau_L}{C}} - 1} \quad (2.7)$$

where z_R is the Rayleigh length. These results show that a high spatial resolution can be achieved in the near threshold region of low laser power and for short exposure times, and that the voxel length is more sensitive to the laser power than to the exposure time. Sun, Kawata et al [62] have suggested that there are two different modes of growth determining the shape of the voxels: focal spot duplication and voxel growth. Near the focal spot, the initial voxels take on focal spot shapes defined by the square of the light intensity relative to the threshold level, in growth known as focal spot duplication. In this mode voxel growth follows the growth of the focal spots in all dimensions with increases in the laser power. In the other mode, voxel shape is dependent on exposure time. Immediately after a threshold exposure time, voxels of a certain size form around locations of high light intensity, and then the voxels gradually grow at their active dangling ends by interaction with new monomers, wherein the chain reaction proceeds. This radical diffusion-dominated process is called voxel growth [37]. From these two scaling laws of voxels, the combination of low laser power and long exposure is advantageous to the formation of low aspect ratio of voxels near the threshold energy. Since the aspect ratio of a voxel is one of the most important parameters for high resolution fabrication via two-photon polymerization, the above scheme will be adopted for the fabrication of precise woodpile structures in the experimental procedure.

3 Chapter 3: Sol - Gel process

3.1 Materials Fabrication

3.1.1 Sol - Gel technique

Sol-gel technology is a powerful tool for the fabrication of organic and inorganic-organic hybrid materials. The advantages of the ease of preparation, modification and processing of the materials along with their high optical quality, photochemical and electrochemical inertness and good mechanical and chemical stability have established this method among other available techniques. The process is based on the phase transformation of a sol obtained from metallic alkoxides or organometallic precursors. This sol, which is a solution containing particles in suspension, is polymerized at low temperature to form a wet gel. This one is going to be densified through thermal annealing to give an inorganic product like glass, polycrystals or a dry gel. By using this method inorganic-organic hybrid materials offer properties better than those prepared alone. Many configurations such as monoliths, fibers, thin and thick films can be achieved in the process of fabrication. Sol-gel materials have been applied in many fields, such as membranes, chemical sensors and catalysis.

The term sol-gel originates from the individual terms of sol and gel. A sol is a suspension of solid particles in a liquid. The size of the dispersed phase (solid particles) is very small (between 1 – 1000nm) and thus gravitational forces are negligible and interaction is dominated by short – range forces like Van-de-Waals attraction and surface charges. The small solid particles are typically metal oxides or metal alkoxides and they are also called precursors in the sol-gel process. The precursors of the sol undergo polymerization which leads to the growth of clusters that finally collide and link together into a gel.

A sol-gel process usually involves catalytic hydrolysis of sol-gel precursor(s) and catalytic polycondensation of the hydrolyzed products and other sol-gel-active components present in the reaction medium to form a macromolecular network structure of sol-gel materials. Any sol-gel material is formed through 4 steps [4]. The first one is *hydrolysis* and condensation in which precursors or monomers such as metal oxides or metal alkoxides are mixed with water and

then undergo hydrolysis and condensation to form a porous interconnected cluster structure. An alcohol is chosen as a solvent for the precursors since they are often insoluble in water. Either an acid such as HCL or a base like NH_3 can be employed as a catalyst.

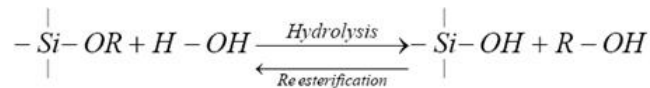


Figure 3.1: Hydrolysis

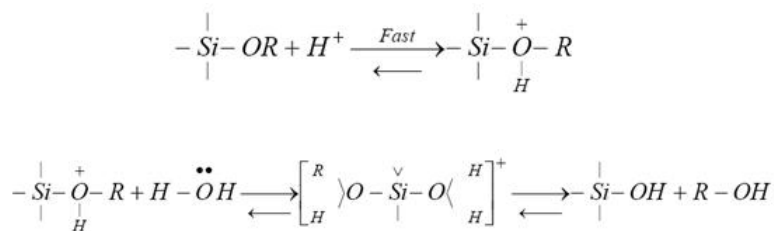


Figure 3.2: Acid - catalyzed

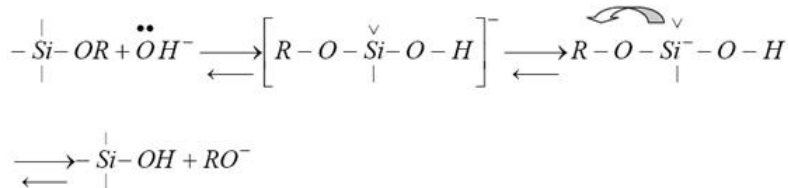


Figure 3.3: Base - catalyzed

The second step is *gelation*. As the first step of hydrolysis and condensation continues, more particles join the clusters. The clusters grow bigger and bigger and they collide with each other and link together to generate a single giant spanning cluster which is called a gel. With time, more clusters present in the sol phase will become connected to the network and the gel will become stiffer and an increase in viscosity and elasticity will result. In addition, hydrolysis and condensation do not stop with gelation. They continue to pass gelation and go to the next step of the sol-gel process.

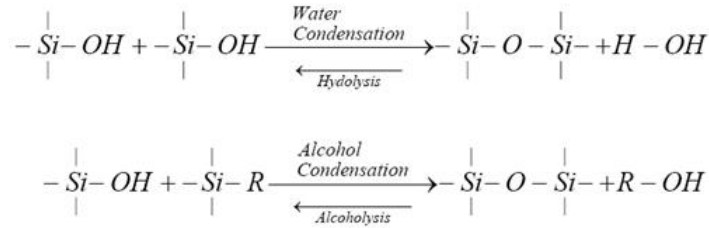


Figure 3.4: Gelation

Aging is the third step of the sol-gel process. During aging, the process of change after gelation can be divided into polymerization, coarsening and phase transformation. Because of the presence of the unreacted hydrolysis groups, condensation reactions continue, resulting in an increase in connectivity of the network and thus an increase in stiffness and strength of the gel. As the continuing condensation process goes on the pores of the gel will become smaller and liquid in the pores will be expelled, leading to gel shrinkage or syneresis. Another change in the process of aging is coarsening, also called ripening. This process involves dissolution and reprecipitation which is driven by differences in the solubility between surfaces with different radii of curvature. The smaller particles, which have positive radii of curvature and higher stability, dissolve again and precipitate into crevices and necks between particles, which have negative radii and lower solubility allowing material to accumulate there. This serves to increase pore size, by filling in smaller pores, and strengthen the network. In addition, phase transformation may take place during aging, such as crystallization from amorphous structure and segregation of a liquid phase into two or more phases.

Drying is the last step of the sol-gel process. It can be divided into three stages. In the first stage, due to evaporation of the liquid in the pores, the gel shrinks. The gel network experiences deformation thanks to capillary forces. New connections in the network are also formed and continue to strengthen the network. The liquid vapor interface remains at the external surface of the gel. Shrinkage continues until stage two starts. The second stage starts when the gel becomes too stiff to shrink and reaches the critical point in which the capillary forces are the highest and the pores begin to empty the liquid in them. At this point, liquid evaporation from pores is slowing down. The liquid retreats into the interior, leaving air-filled pores near the surface. Finally, once the liquid is primarily out of the pores, the liquid is isolated

into pockets. Evaporating within the gel body and diffusing the vapor to the exterior is the only way out for the remaining liquid. No further shrinkage occurs. Loss of weight is the only significant change until equilibrium is reached with the environment.

4 Chapter 4: Linear and Non-linear materials characterization techniques

Characterization techniques for the linear and nonlinear materials fabricated via the sol-gel process will be described. In the former case, the prism film coupler method will be used for the determination of the linear refractive index by measuring the coupling angles at the prism surface. For the latter case, the nonlinear refractive index change will be calculated using the well known Z-scan method. A short introduction about nonlinear material processes is also given.

4.1 Characterization techniques for Linear materials

4.1.1 The Prism-film coupler

The prism-film coupler, given schematically in Figure 4.1, consists of a rectangular and isosceles (in our case) prism with a refractive index n_p (higher than that of the film), tightened against a planar waveguide. The prism is placed above the thin film guide and is separated from it by a small gap of low refractive index material (air). The air gap thickness, S , is controlled with a screw at the back of the waveguide [70].

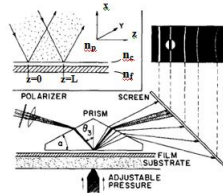


Figure 4.1: Prism-film coupler [70]

In general, the coupling of an incident laser beam by a prism into a thin film is governed by the incident angle of the beam on the prism base. The laser beam enters the prism, reaches the base at an angle of incidence θ_3 and is totally reflected. Normally, the incident power is totally reflected. Under certain conditions, however, the light energy can be transferred into the film via resonant frustrated total internal reflection, i.e. via evanescent waves excited in the air layer. The evanescent waves, having traversed the gap, drive electrons in the frustrating medium and in turn generate a wave that significantly alters the field configuration, thereby permitting energy flow.

The part of the incident energy that has tunneled through the low-index gap into the film, is then alternately reflected at the film-substrate and at the film-gap interfaces so that a zig-zag propagation along the guide results (figure 4.2).

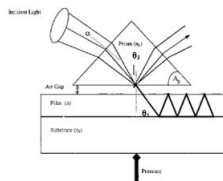


Figure 4.2: Zig-zag waves in the waveguide

Therefore, the incident beam must have the proper angle of incidence so that the evanescent fields in the gap S travel with the same velocity as the mode to be excited in the film. In other words, the component of the propagation constant parallel to the film surface must be equal for the wave in the prism and the wave in the guiding film. This leads to a finite number of discrete incidences of the input laser beam, for which the light can be strongly coupled into the guide, called synchronism angles. Let the propagation constant of the mode under consideration be β . Then, for the incident beam at the prism base the component of the propagation vector parallel to the film is $kn_p \sin \theta_3$, $k = \frac{\omega}{c}$. A direction θ_3 is a synchronous one if $\beta = kn_p \sin \theta_3$. Hence, by proper orientation of the direction of the incident beam, with respect to the prism surface and therefore with the film surface, it is possible to excite any of the film guided modes. Alternatively, the propagation constant β or the phase velocity $\frac{\omega}{\beta}$ of a mode can be determined by measuring the synchronous direction of θ_3 of that mode. Furthermore, when light is coupled into one of the waveguide modes, because of film inhomogeneities, the optical energy is rapidly scattered into other modes and is then coupled back to the outside medium through the other face of the prism. The returned light wave in the prism, therefore, consists of many waveguide modes [71],[68]; each of them appears in its own synchronous direction. We thus see on the screen, where the light beam is reflected, a series of bright lines (called m - lines) with a bright spot on one of this lines (shown in figure 4.1). Each line represents a mode (i.e. the light propagated in the film) of different order m , while the bright spot is the beam totally reflected from the base of the prism. When the spot is on the m_{th} bright line, this means that we are exciting the m_{th} mode. With increasing coupling the lines become brighter first, and then

become broader and shift. Their positions and line widths depend critically on the spacing S of the coupling gap. For infinite gap width they converge against the modes of the free guide, i.e. the modes in the absence of the prism. The m – *lines* are, therefore, a direct display of the spectrum of the film modes. The phase velocity of a light wave in a thin film waveguide depends on the thickness of the film and the mode of propagation. If the characteristics of the prism ($\varepsilon \equiv$ prism angle and n_p) are known, as well as, the substrate refractive index, n_s , and at least two modes are supported by the waveguide, we can estimate both thickness and refractive index of the guiding film. In addition, the intensity distribution of the reflected spot gives the m – *line's* profile. A change in the coupling efficiency (i.e. the thickness S of the air layer between the prism and the guide) changes the shape of the m – *line*, whereas a change in the refractive index of the film causes a pure shift of the m – *line* (with no distortion of the m – *line's* profile) [24]. This is the property that permits the detection of the modifications of the refractive index of a thin film.

4.1.2 Waveguide modes

The light energy is trapped in the film as the wave is totally reflected back and forth between the two film surfaces. In addition, the wave suffers a phase change at the lower and upper film boundary due to total internal reflection. Since there is overlapping of the waves as they travel in the zig-zag path and in order to avoid the decay of optical energy due to destructive interference as the waves travel through the guide, the total phase change for a point on a wavefront that travels from the $n_2 - n_3$ interface to the $n_2 - n_1$ interface and back again must be a multiple of 2π ($\Delta = 2m\pi$ with integer m). The vertical components of the wave vectors have a magnitude of $kn_2 2\cos\theta_1$. The phase change for the plane to cross the thickness W of the film twice (up and down) is then $2kn_2 W \cos\theta_1$. Applying Snell's law and the condition for total internal reflection, we get an expression for the phase change suffered upon total internal reflection at the interface.

$$\Phi_{TE} = \tan^{-1} \left[\frac{\left(\beta^2 - kn_2^2 \right)^{\frac{1}{2}}}{h} \right]$$

Thus, the phase shift in each of the waveguide interfaces is given as follows: At the interface $n_2 - n_1$ ($x = W, n_2 > n_1$), the wave suffers a phase change of

$-2\Phi_{21}$:

$$\begin{aligned} \tan\Phi_{21,TE} &= \frac{(n_2^2 \sin^2 \theta_1 - n_1^2)^{\frac{1}{2}}}{n_2 \cos \theta_1} = \left[\frac{n_2^2 \sin^2 \theta_1 - n_1^2}{n_2^2 - n_2^2 \sin^2 \theta_1} \right]^{\frac{1}{2}} \\ \tan\Phi_{21,TE} &= \frac{n_2^2}{n_1^2} \frac{[n_2^2 \sin^2 \theta_1 - n_1^2]^{\frac{1}{2}}}{n_2 \cos \theta_1} = \frac{n_2^2}{n_1^2} \tan\Phi_{21,TE} \quad (4.1) \end{aligned}$$

At the interface $n_2 - n_3(x = 0)$, the wave suffers a phase change of $-2\Phi_{23}$:

$$\text{and } \tan\Phi_{23,TE} = \frac{[n_2^2 \sin^2 \theta_1 - n_3^2]^{\frac{1}{2}}}{n_2 \cos \theta_1} = \left[\frac{n_2^2 \sin^2 \theta_1 - n_3^2}{n_2^2 - n_2^2 \sin^2 \theta_1} \right]^{\frac{1}{2}} \quad (4.2)$$

In this manner, we can find the phase difference after subsequent zig-zags for the waves travelling upwards and downwards, as follows [69]: The phase of the wave at $z = z_c$ and $x = 0$ is $-\omega t + \beta z_c$. The phase of the wave at the same point but after a zig-zag path is the phase of the wave at $z = z_a$ and $x = 0$ plus that of a zig-zag. It is

$$-\omega t + \beta z_a + \beta(z_c - z_a) + 2kn_2 \cos \theta_1 W - 2\Phi_{21} - 2\Phi_{23} \quad (4.3)$$

The difference of the last two equations is $\Delta = 2m\pi$, therefore,

$$2kn_2 \cos \theta_1 W - 2\Phi_{21} - 2\Phi_{23} = 2m\pi \quad (4.4)$$

This is the equation of the modes. Since $2kn_2 \cos \theta_1 W$ is positive and both $\Phi_{21}, \Phi_{23} \leq \frac{\pi}{2}$, m can not be negative. The integer m may then be 0, 1, 2, 3... up to certain finite value, depending on W . This m specifies the order of the mode. The equation (4.4) stands for both polarization states. Furthermore, it is also worthwhile to note that in spite of the zigzag wave motion described above, the wave in the waveguide mode appears to propagate in the horizontal direction only. The vertical path of the wave motion simply forms a standing wave between the two film surfaces. Thus, in a more explicit manner, it is better to use β and u exclusively for the phase constant and the wave velocity parallel to the film. These two last quantities are related through

$$\beta = kn_2 \sin \theta_1, u = c \frac{k}{\beta} \quad (4.5)$$

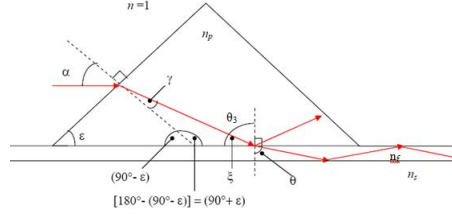


Figure 4.7: Propagation angles in ambient, prism and film

The light propagation angle inside the waveguide can easily be related to the angle between the laser beam and the normal to the surface prism (a). The relations between the angles reported in Figure 4.7 are:

$$\xi = 180^\circ - (90^\circ + \varepsilon) - \gamma = 90^\circ - \varepsilon - \gamma \quad (4.8)$$

$$\theta_3 = 90^\circ - \xi = \varepsilon + \gamma = \varepsilon + \sin^{-1}\left(\frac{\sin a}{n_p}\right) \quad (4.9)$$

and recalling Snell's law at the interfaces: prism-air : $\sin \gamma = \left(\frac{n_c}{n_p}\right) \sin a$ (4.10)

prism-film: $\sin \theta = \left(\frac{n_p}{n_f}\right) \sin \theta_3$ (4.11)

Using the above equations we can write:

$$\begin{aligned} \beta &= kn_p \sin(\varepsilon + \gamma) \Rightarrow \\ \frac{\beta}{k} &= n_p \cos[(90^\circ - \varepsilon) - \gamma] \Rightarrow \\ \frac{\beta}{k} &= n_p \cos[(90^\circ - \varepsilon) - \sin^{-1}(\sin a/n_p)] \quad (4.12) \end{aligned}$$

and this equation gives us a method for the calculation of the effective refractive index and the angle of incidence onto the prism surface.

4.2 Characterization techniques for Non-Linear materials

Under normal conditions the response of a medium to light is linear and as a consequence most optical phenomena can be described with a linear refractive index. It was only with the invention of lasers in the early 1960's that the available optical power level increased to a level where the response of the medium started to deviate from the linear behavior. At sufficiently high intensities the response of a material depends on the light intensity.

4.2.1 Basic concepts of nonlinear optics

The optical response of a material is expressed in terms of the induced polarization $\vec{P} = -Ner$ in the molecule, where e is the electronic charge, N is the electron density in the medium and r is the field induced displacement. For a linear material, the relation between the polarization and the electric field \vec{E} of the incident radiation is linear [50]:

$$\vec{P} = \epsilon_0 \chi^{(1)} \vec{E} \quad (4.13)$$

where $\chi^{(1)}$ is the linear susceptibility.

The Lorentz model provides an instructive way to visualize the optical properties of a medium by considering it as an assembly of forced harmonic oscillators. The bonding of electrons to the nuclei is approximated by that of charged particles attached to nuclei by springs. The force F_e exerted on an electron of charge e by the electric field E is given by: $F_e = eE$. The bond, approximated as a spring, will exert a restoring force on the electron given by: $F_R = -m\omega_0^2 x$, where m is the mass of the electron, x is the displacement from the equilibrium position, and ω_0 is the natural frequency of the oscillator and is equal to the square root of the ratio of the elastic constant to m . From Newton's second law, we have:

$$eE - m\omega_0^2 x = m \frac{d^2 x}{dt^2} \quad (4.14)$$

And, if we consider a damping oscillator with a damp constant Γ , we get:

$$\frac{d^2 x}{dt^2} + 2\Gamma \frac{dx}{dt} + \omega_0^2 x = -\frac{e}{m} E \quad (4.15)$$

The solution of the above differential equation yields the following expression for the displacement x :

$$x = -\frac{e}{m} E \frac{e^{i\omega t}}{\omega_0^2 - 2i\omega\Gamma - \omega^2} + c.c. \quad (4.16)$$

where c.c. denotes the complex conjugate. Equation (4.16) suggests sinusoidal behavior in time with an increasing displacement as the frequency of the field approaches the natural frequency of the oscillator. Since $P = -Ner$, we have the following expression for the polarization:

$$P = \frac{Ne^2}{m} \frac{1}{\omega_0^2 - 2i\omega\Gamma - \omega^2} E(\omega) e^{i\omega t} + c.c. \quad (4.17)$$

Thus, the induced polarization is proportional to the amplitude of the electric field and has the same frequency dependence.

As the electromagnetic wave propagates through the medium the electrons surrounding the nuclei (approximated as harmonic oscillators) are polarized and these oscillating dipoles act as new sources of radiation. The frequency of the radiative wave is identical to the incident wave but its phase lags behind the incident wave by a time determined by the natural frequency of the oscillator. If the wave encounters N oscillators as it passes through the medium, it will accumulate a phase delay proportional to N and will appear to have been delayed relative to a parallel wave that had traveled an identical distance but in vacuum. The ratio between the velocity of light in vacuum, c , and the velocity in the medium or phase velocity u , is the refractive index of the material. So, this leads to:

$$n^2 = \varepsilon = 1 + 4\pi\chi^{(1)} = 1 + \frac{Ne^2}{m} \frac{4\pi}{\omega_0^2 - 2i\Gamma\omega - \omega^2} \quad (4.18)$$

When N is small enough, the absolute value of the second term on the right is small compared with unity. Because of resonances in molecules and solids associated with electronic and nuclear motions, the refractive index and, hence the dielectric constant are complex quantities. We can rewrite equation (4.21) as follows:

$$Re(n) = 1 - \frac{Ne^2}{m} \frac{4\pi\gamma\omega}{(\omega^2 - \omega_0^2)^2 + (2\Gamma\omega)^2}, \quad Im(n) = \frac{Ne^2}{m} \frac{4\pi\gamma\omega}{(\omega^2 - \omega_0^2)^2 + (2\Gamma\omega)^2} \quad (4.19)$$

The real and imaginary parts of the refractive index corresponding to dispersion and absorption are expressed as a function of frequency in the region of an optical transition ω_0 . Near the peak of the absorption the refractive index decreases rapidly and begins to increase again slowly on the high-energy side of the transition.

4.2.2 Non-linear optical media

However, at higher intensities this is no longer an adequate description. Thus, the response of a material is often be described as a Taylor expansion of the material polarization \vec{P} in powers of the electric field \vec{E} . Each component \vec{P}_k ($k = x, y, z$) of the material polarization can be expressed as :

$$\vec{P}_k = \varepsilon_0 \left(\chi_{ik}^{(1)} E_i + \chi_{ijk}^{(2)} E_i E_j + \chi_{ijkl}^{(3)} E_i E_j E_l + \dots \right) \quad (4.20)$$

Here, the coefficients $\chi^{(n)}$ correspond to the tensor of the $n - th$ order non-linear process and it's magnitude describes the strength of the $n - th$ order nonlinear processes. A harmonic input field at frequency ω is given by:

$$\vec{E}_i = E_i e^{-i\omega t} + c.c. \quad (4.21)$$

where E_i is the field amplitude at a given position. If we consider for simplicity only the second order term, the resulting second order non-linear polarization is then:

$$P_k = \chi_{ijk}^{(2)}(E_i E_j e^{-2i\omega t} + E_i^* E_j^* e^{i2\omega t} + E_i E_j^* + E_i^* E_j) \quad (4.22)$$

The above equation shows the presence of new frequency components due to the nonlinear polarization. It is clear that the non-linear polarization contains a component that radiates at twice the frequency of the input light. And, also contains a component at frequency zero, an effect known as optical rectification. Contributions from the second and third order terms to the nonlinear polarization are predicted from different symmetry properties. For example, if we ignore the DC field, for a medium with inversion symmetry one has to consider an important symmetry aspect, that is all even order coefficients must vanish. Since the operation $\vec{r} \rightarrow -\vec{r}$ leaves the inversion symmetric media unaffected, but does add minus and signs to both $\vec{P} \rightarrow -\vec{P}$ and $\vec{E} \rightarrow -\vec{E}$, this is possible only when $\chi^{(n)} = 0$ for even n . Hence, a contribution from $\chi^{(2)}$ can come only from noncentrosymmetric media, whereas $\chi^{(3)}$ contributions can come from any medium regardless of symmetry.

In general, second-order nonlinear optical effects can be visualized as a three-wave mixing process, where the waves exchange energy with one another through the intercession of the nonlinear medium [73]. The process is described by the interaction of waves at frequencies ω_1 and ω_2 to produce a new frequency ω_3 . The susceptibility, in the frequency domain, is provided with an argument to describe the process, for example, $\chi^{(2)}(-\omega_3; \omega_1, \omega_2)$. For the case of second harmonic generation the term is $\chi^{(2)}(-2\omega; \omega, \omega)$, i.e. two photons from the input beam combine to generate a new photon at double the frequency. Similarly, third-order non-linear optical effects can be described as four-wave mixing processes where waves at frequencies $\omega_1, \omega_2, \omega_3$ interact to produce ω_4 . In general, the waves can be any combination of frequencies that satisfies the momentum conservation requirement. The coefficient

is represented as $\chi^{(3)}(-\omega_4; \omega_1, \omega_2, \omega_3)$. For third harmonic generation for instance, it becomes $\chi^{(3)}(-3\omega; \omega, \omega, \omega)$. Furthermore, for isotropic materials the induced polarization is parallel to the field and is related to it by a scalar proportionality factor $-\chi^{(n)}$, whereas for anisotropic materials the susceptibilities are tensor quantities relating the polarization response in one direction to field components in three directions.

For example, the basic idea concerning generation of second harmonic waves can be treated as a two-steps procedure. In the first step, the incident field E_1 at frequency ω excites a weak nonlinear polarization at double the frequency $P_2 \propto E_1^2$. In the second step this induced nonlinear polarization P_2 radiates according to Maxwell's equations and emits an optical field E_2 at optical frequency 2ω . The second harmonic light originates from the nonlinear polarization. The input field generates a set of dipoles inside the crystal that all radiate weakly at twice the frequency of the input wave. As the input beam has a well defined phase and amplitude at every point inside the crystal at a given time, the relative phase of the induced dipoles is fixed. To obtain a second harmonic output at the end of the crystal it is important that the induced dipoles radiate in phase. This process is referred to as phase-matching which ensures that the contributions from all positions in the crystal add up constructively.

At every position in the crystal, the non-linear polarization creates a dipole emitter that radiates at twice the fundamental frequency. At all times, the relative phase of these dipoles is given by the non-linear polarization generated by the fundamental wave: $(e^{ik_{z,\omega}z})^2 = e^{i2k_{z,\omega}z}$. The plane waves emitted in the forward direction are plane waves at double the frequency and have the form $e^{-ik_{z,2\omega}z}$. The overall efficiency of this process in the forward direction is obtained by adding all contributions from different positions. This leads to the following integral that gives the conversion efficiency per unit length (in terms of intensity) of the process:

$$\eta = \frac{1}{L^2} \left| \int_0^L e^{i2k_{\omega}z} e^{-ik_{2\omega}z} dz \right|^2 = \frac{1}{L^2} \left| \int_0^L e^{i\Delta k z} dz \right|^2 = \left(\frac{\sin\left(\frac{\Delta k L}{2}\right)}{\frac{\Delta k L}{2}} \right)^2 \quad (4.23)$$

where $\Delta k = 2k_{\omega} - k_{2\omega} = \frac{2\omega n(\omega)}{c} - \frac{2\omega n(2\omega)}{c}$ is the wavevector mismatch of the process and L is the crystal thickness. The *sinc* function has a maximum for $\Delta k = 0$ where $\eta = 1$. Therefore, the phase difference between the nonlinear

waves is $\Delta\Phi = (\Delta K)L$. We introduce the coherence length l_c for the nonlinear process as the distance over which the phase mismatch becomes equal to 2π . Thus, $\frac{2\omega}{c} (n_{2\omega} - n_\omega) l_c = 2\pi \Rightarrow l_c = \frac{\lambda}{2(n_{2\omega} - n_\omega)}$. For example, if $\lambda = 1\mu m$, $n_{2\omega} - n_\omega = 10^{-2}$, we get that $l_c \sim 50\mu m$. Only the waves emitted within a very short distance of the surface will add together coherently. The phase matching condition corresponds to momentum conservation in the nonlinear process. In the more general case, when a photon of wave vector k is generated by mixing two photons with wave vectors k_1 and k_2 , the phase matching condition can be written as $k = k_1 + k_2$

Consider now, an optical beam with frequency ω and a DC field written in the form: $E = E(0) + E(\omega) = E(0) - E\cos(\omega t - kz)$ (4.24). Substituting equation (4.27) into equation (4.23) gives [50]:

$$P = \chi^1 [E(0) + E_0\cos(\omega t - kz)] + \chi^{(2)} [E(0) + E_0\cos(\omega t - kz)]^2 + \chi^{(3)} [E(0) + E_0\cos(\omega t - kz)]^3 + \dots \quad (4.25)$$

Expanding these terms and applying the appropriate trigonometric identities, we get:

$$P(\omega) = \chi^{(1)} E_0 \cos(\omega t - kz) + 2\chi^{(2)} E(0) E_0 \cos(\omega t - kz) + 3\chi^{(3)} E_0^2 E_0 \cos(\omega t - kz) + \frac{3}{4}\chi^{(3)} E_0^3 \cos(\omega t - kz) = \chi_{eff} E(0) \cos(\omega t - kz) \quad (4.26)$$

Thus, for the nonlinear refractive index:

$$\begin{aligned} n^2 &= 1 + 4\pi\chi_{eff} = 1 + 4\pi \left[\chi^{(1)} + 2\chi^{(2)} E(0) + 3\chi^{(3)} E^2(0) + \frac{3}{4}\chi^{(3)} E_0^2 \right] \\ n^2 - n_0^2 &= 8\pi\chi^{(2)} E(0) + 12\pi\chi^{(3)} E(0)^2 + 3\pi\chi^{(3)} E_0^2 \\ n &= n_0 + \frac{4\pi\chi}{n_0} E(0) + \frac{6\pi\chi}{n_0} E(0)^2 + \frac{3\pi}{2n_0} \chi^{(3)} E_0^2 \quad (4.27) \end{aligned}$$

The definition of the light intensity in cgs units is $E_0^2 = \frac{8\pi}{cn} I(\omega)$, which when substituted into equation (4.27) gives:

$$n = n_0 + \frac{4\pi\chi^2}{n_0} E(0) + \frac{6\pi\chi^{(3)}}{n_0} E(0)^2 + \frac{12\pi^2}{cn_0^2} \chi^{(3)} I \quad (4.28)$$

Therefore, the value of the nonlinear refractive index at frequency ω can be written as:

$$n(\omega) = n_0(\omega) + n_1 E(0) + n_2 E(0)^2 + n_2(\omega) I(\omega) \quad (4.29)$$

where

$$n_0(\omega) = \frac{4\pi\chi^{(2)}}{n_0}, \text{ corresponds to the linear electrooptic effect}$$

$$n_1(\omega) = \frac{6\pi\chi^{(3)}}{n_0}, \text{ the quadratic electrooptic effect}$$

$$n_2(\omega) = \frac{12\pi\chi_2^{(3)}}{cn_0^2}, \text{ the optical Kerr effect}$$

4.2.3 The optical Kerr effect

In the case of the optical Kerr effect, we have just a single beam at frequency ω incident on the nonlinear medium, and the nonlinear interaction produces a third-order polarization at the same frequency as the input laser beam. This works by using $\omega_1 = \omega_2 = +\omega$ and $\omega_3 = -\omega$, so as to satisfy the four wave mixing $\omega_4 = \omega_1 + \omega_2 + \omega_3$. No phase matching problems occur in this case, because the nonlinear polarization is at the same frequency as the driving fields and thus the fields are in-phase throughout the whole medium.

As we saw in the previous section, one of the main consequences of the optical Kerr-effect is that the refractive index begins to depend on the intensity of the beam:

$$n = n_0 + \frac{\chi^{(3)}}{n_0 c \epsilon_0} I = n_0 + n_2 I \quad (4.31)$$

Self-action effects describe a special case of processes derived from the intensity dependence of the refractive index, in which the nonlinear polarization is created in the medium at the same frequency as the incident beam. There is only one incident beam that provides the three input photons for the interaction. It is called self-action effect since the nonlinear polarization created by an incident beam affects the propagation or other properties of the same beam through an intensity dependent refractive index. *Self-focusing* or *self-defocusing* processes are derived from the combined action of an intensity-dependent refractive index and a spatial variation of the laser intensity in which the beam is more intense at the center than at the edges.

It is worth mentioning here that self-action utilizes the real part of χ^3 , while two photon absorption involves the imaginary part of χ^3 . This process occurs when the material has an electronic excited level at twice the frequency ω of the input beam. A process involving the imaginary part of susceptibility implies damping of the wave in the medium resulting from the exchange of energy between the optical field and the medium. In contrast, self-action effects do not require any exchange of energy between the optical field and the nonlinear medium.

Z-scan method

Sheik-Bahae et al [57] used a z-scan method based on self-focusing to measure the sign as well as the magnitude of $\chi^{(3)}$. The z-scan experimental arrangement is shown in figure 4.8. A Gaussian beam is tightly focused by a lens and passed through the nonlinear medium. The output power is measured by a detector after passing through a finite aperture. The transmitted power is obtained as a function of the sample position in the z axis measured with respect to the focal plane. From a quantitative analysis of this z-scan transmitted power profile, one obtains both the magnitude and the sign of the nonlinearity. Consider the case where a nonlinear material with a nonlinear refractive index $n_2 < 0$ (case of self-defocusing) and thickness less than the depth of focus is located in front of the focus ($-z$). Starting the scan from a distance far away from focus (negative z), the beam irradiance is low and negligible nonlinear refraction occurs. As the sample is moved towards the focus, the increased power density rise to negative lensing effect with a net result of collimating the beam and consequently increasing the power through the aperture. With the sample moved to the $+z$ side of the focus, the negative lensing effect diverges the beam and, therefore, reduces the power passing through the aperture. At $z = 0$, the effect is analogous to placing a thin lens at the focus that will cause a minimal far-field pattern change. The resulting curve is shown schematically. For a self-focusing nonlinearity ($n_2 > 0$), a profile opposite in sign to that presented in figure 4.9 will be observed, i.e. a prefocal transmittance minimum (valley) followed by a postfocal transmittance maximum (peak).

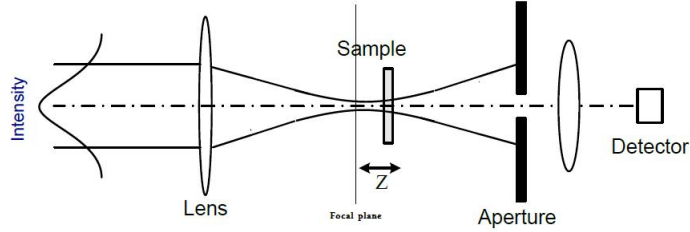


Figure 4.8: Z-scan scheme

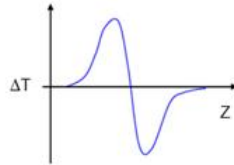


Figure 4.9: Z-scan curve

The above scheme is considered assuming that no absorptive nonlinearities such as multiphoton absorption are present. Qualitatively, multiphoton absorption leads to suppression of the peak and enhancement of the valley. The sensitivity to nonlinear refraction is entirely due to the aperture, and removal of the aperture completely eliminates the effect. Although, the method provides an easy way to obtain the sign and magnitude of the nonlinearity, the beam quality imposes a stringent requirement for it to be a Gaussian (TEM_{00}). Because it requires a high power density and long interaction length, the method is not useful for thin polymeric films. Furthermore, because of longer path lengths, even weakly absorbing samples will provide large refractive index changes derived from thermal effect [8],[20],[14]. This effect get more evident when a nanosecond pulse is used [18]. In the case of a solid sample, sample damage due to high power densities needed for self-focusing to take place, is another serious problem.

In the z-scan experiment, the intensity profile of the beam has a Gaussian distribution:

$$I(r, t) = I_0 \frac{w_0^2}{w(z)^2} e^{-\frac{2r^2}{w(z)^2}} \quad (4.32)$$

where $w^2(z) = w_0^2 \left(1 + \frac{z^2}{z_0^2}\right)$ is the beam radius, $z_0 = \frac{kw_0^2}{2}$ is the diffraction length of the beam, $r = \sqrt{x^2 + y^2}$ is the distance of the point to the center of the beam, $k = \frac{2\pi}{\lambda}$ is the wavevector and λ is the laser wavelength. Let L be the thickness of the sample, α the linear absorption coefficient. The effective length related to the phase change is given by $L_{eff} = \frac{1 - e^{-\alpha L}}{\alpha}$. In addition to the phase change due to the linear refractive index, there is another phase change due to the light intensity. This phase shift which follows the radial variation of the incident irradiance at a given position of the sample z , is given by:

$$\Delta\Phi(r, z, t) = \Delta\Phi_0(z, t) e^{-\frac{2r^2}{w^2(z)}} \quad (4.33)$$

with $\Delta\Phi_0(z, t) = \frac{\Delta\Phi_0(z, t)}{1 + \frac{z^2}{z_0^2}}$, $\Delta\Phi_0(t) = k\Delta n_0(t) L_{eff}$. In the steady state, the Kerr effect can be attributed to various origins, including the electronic contribution, molecular reorientation, and thermal effects. In our case we are interested in the electronic contribution, so $\Delta n_0 = n_2 I_0(t)$, with $I_0(t)$ being the on-axis irradiance at focus (i.e., $z = 0$).

The phase change of the optical wave inside the medium is proportional to the refractive index. For a laser beam that has a non-uniform intensity distribution at its phase front, the phase change is not uniform across the whole beam. As a consequence of this, different portions of the beam have different phase delays even if the medium has a uniform thickness. In other words, in a laser beam the index change in the flat sample takes the form of a lens whose effective focal length is determined by the nonlinear response. As a result of this nonlinear response, the refractive index of the material is larger (smaller) at the center of the beam than at its periphery, with the result that the medium is in effect turned into a positive (negative) lens, if the sample has a positive n_2 , it acts as a positive lens under illumination.

With some reasonable approximations (such as thin sample, small phase distortion), one can derive the normalized transmittance of the closed-aperture z-scan:

$$T(z, \Delta\Phi_0) \simeq 1 - \frac{4\Delta\Phi_0 x}{(x^2 + 9)(x^2 + 1)} \quad (4.34)$$

where $x = \frac{z}{z_0}$. If the sample moves along the propagation direction of the beam, the transmittance versus distance curve will show a valley-peak for positive n_2 or peak-valley for negative n_2 . The distance between the valley and peak is proportional to the Rayleigh range z_0 . The difference between the valley and peak is proportional to the phase distortion ($\Delta T = 0.406\Delta\Phi_0$) .

Apart from self-focusing and self-defocusing described above, there is another self-action effect related to the intensity dependent refractive index. *Self-phase modulation* is associated with the temporal behavior of the induced refractive index change, $\Delta n(t) = n_2 I(t)$, and is important only when the optical pulse is of the order of a picosecond or less. The result is a broadening of the frequency profile. The phase ϕ of the wave is given as

$$\phi(t, z) = \omega t - kz = \omega t - \frac{n\omega z}{c} = \omega t - \frac{[n_0 - n_2 I(t)]\omega z}{c} \quad (4.35)$$

The temporal variation $\omega(t) = \frac{d\phi}{dt} = \omega - \frac{2\pi}{\lambda_0} L n_2 \frac{dI}{dt}$ of the phase gives the instantaneous frequency ω . In the presence of a fast temporal intensity variation ($I = I_0 e^{-\frac{t}{\tau}}$), the refractive index n , being dependent on intensity, becomes a function of time. This time dependence of n leads to added temporal variations of phase ϕ through the above equation, and consequently generates different frequency components giving rise to a broadening of the frequency profile. Plotting $\omega(t)$ shows the frequency shift of each part of the pulse. A pulse (top curve) propagating through a nonlinear medium undergoes a self-frequency shift (bottom curve) due to self-phase modulation. The front of the pulse is shifted to lower frequencies, the back to higher frequencies. In the centre of the pulse the frequency shift is approximately linear. τ is half the pulse duration.

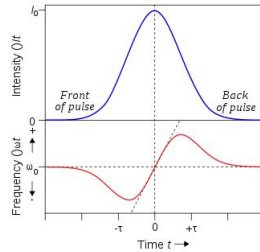


Figure 4.10: Self-phase modulation

It is clear that the extra frequencies generated through self-phase modulation broaden the frequency spectrum of the pulse symmetrically. In the time domain, the envelope of the pulse is not changed, however in any real medium the effects of dispersion will simultaneously act on the pulse. In regions of normal dispersion, the "redder" portions of the pulse have a higher velocity than the "blue" portions, and thus the front of the pulse moves faster than the back, broadening the pulse in time. White light continuum generation is based on a self-phase modulation effect and will be used in the optical characterization section of the experimental part.

$$P_i(\omega) = \frac{3}{4} \text{Im}[xi]$$

4.2.4 Non-linear molecules

The molecule can be considered as a polarizable entity in itself in contrast to the medium which consists of an assembly of such molecules. This distinction is necessary since many subtle features of molecular structure account for its polarization response. Understanding the molecular non-linear response and solid-state structure allows a connection to be established between the response of the molecule and that of the medium. Therefore, it is convenient to define microscopic non-linear coefficients that relate the molecular dipole moment with the electric field applied to the molecule. Including the possibility of a permanent molecular dipole moment, μ_0 , the molecular dipole moment is related to the electric field components in the frequency domain by:

$$\begin{aligned} \mu_i^\omega = & \mu_i^0 \delta_{0,\omega} + \sum_j \alpha_{i,j}^{(1)}(-\omega; \omega) E_j^\omega + \sum_{jk} \beta_{ijk}^{(2)}(-\omega; \omega_1, \omega_2) E_j^{\omega_1} E_k^{\omega_2} + \\ & \sum_{jkl} \gamma_{ijkl}^{(3)}(-\omega; \omega_1, \omega_2, \omega_3) E_j^{\omega_1} E_k^{\omega_2} E_l^{\omega_3} + \dots \end{aligned} \quad (4.36)$$

where $\alpha^{(1)}$, $\beta^{(2)}$ and $\gamma^{(3)}$ are the tensors corresponding to the first, second and third order molecular susceptibilities. The α polarizability term describes the linear interaction with the optical field and accounts for linear absorption and refraction behavior of the molecule. The higher order terms β , γ describe the microscopic non-linear optical interactions and likewise are sensitive to the electronic structure of the molecule. Again, symmetry requirements impose that only noncentrosymmetric molecules μ_i and β_{ijk} are nonzero.

Polymers are long-chain molecules composed of repeated sequences of monomer units based on carbon-carbon bonds. Polymers can be divided into two generic types, namely conjugated or saturated [[50]]. The division lies in whether there are alternate single-double bonds along the polymer backbone or not. In saturated polymers all the electrons are incorporated into σ bonds, and there are very tightly bound. Their transitions are at high energies in the ultraviolet spectral region. On the other hand, conjugated polymers are formed into a long chain with alternating single bond σ electrons and double bond π electrons between the carbon atoms. $\pi \rightarrow \pi^*$ transitions occur in the visible spectral region for many conjugated polymers. The π electrons have relatively high kinetic and low potential energy relative to the electrons in σ bonds. In the latter case, the orbitals involved in bonding overlap along the internuclear axis to give bonds with axial symmetry, whereas in the former case they overlap laterally. The π bonds are weaker giving the possibility for the π electrons to move freely along the polymer chain. It is the delocalization behavior of π electrons that makes the π electron distribution highly deformable giving rise to large optical nonlinearities.

Part II

Experimental

5 Chapter 5: Fabrication, Characterization and Simulation

Photonic crystals fabricated and described in the present thesis were structured by means of two - photon polymerization technique. This technique is favorable for layer by layer fabrication suitable for the realization of the woodpile structures. In addition, this technique provides the possibility to fabricate structures with feature sizes of a few tens of nanometers enabling the realization of high resolution photonic crystals with response in the optical frequencies. Optical characterization of the fabricated structures was done through a home - build setup used to measure angle resolved transmittance spectra, while laser diffraction enabled a determination of the quality and orientation of the fabricated crystals. Experimental results were compared to theoretical simulations provided through the freely available MPB software package [30] based on the finite difference time domain method.

5.1 Fabrication via Direct Laser Writing

The basic concept of direct laser writing is to expose a photosensitive material not by single-photon absorption, but by two or multi photon absorption. Therefore, a laser system is required that provides short pulses with a photon energy well below the one-photon absorption edge of the photoresist. The experimental setup is schematically depicted in figure 5.1.

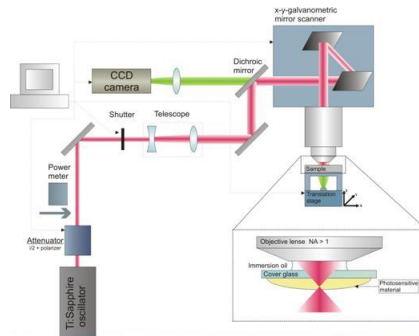


Figure 5.1: Experimental set - up for direct laser writing

The oscillator, a regenerative amplified Ti:Sapphire laser system provides short pulses (around 20 fs) at a central wavelength of 800 nm, at which single-photon absorption is negligible. The laser beam passes through a combination of a half-wave plate ($\frac{\lambda}{2}$) and a polarizer, which allows the adjustment of the intensity of the laser and controls the exposure of the photoresist and thus, to control the actually voxel size. In sequence, two lenses serve as a telescope to expand the beam diameter before entering a high numerical aperture (NA=1.4) oil-immersion objective lens. The laser beam is coupled to the objective lens using a dichroic mirror, highly reflective at the laser wavelength, but transmittive at other spectral positions. Such a setup enables one to collect photoexcited fluorescence, and transmitted radiation of an external illumination source mounted below the sample for in situ imaging. The photopolymerized structure is generated in a layer-by-layer format in two ways: a) either by using an x-y galvanometric mirror scanner, where the movement on the z-axis is achieved using a high resolution linear stage, or b) the sample is mounted on a piezo-electric transducer (PZT)-controlled high precision 3D translation stage, which ensures positioning within the range of hundreds of micrometers with an accuracy of a few nanometers. In addition, the laser beam can be opened or blocked by an electromechanical shutter enabling discrete or contiguous exposure traces according to need. The trajectory and speed of the stage motion, as well as, the shutter function are controlled synchronously with the arrival of laser pulses by customized software running through a PC. For the online monitoring of the photopolymerization process, a CCD camera is mounted behind the dichroic mirror. As the refractive index of the photopolymer changes during polymerization, the illuminated structure becomes visible during the building process.

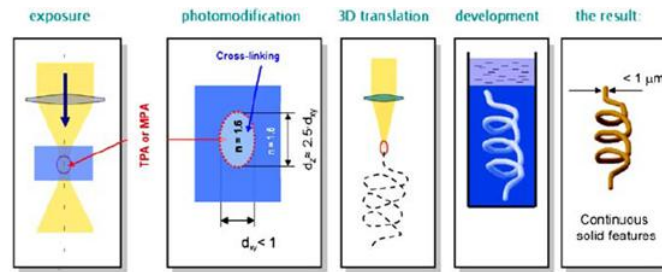


Figure 5.2: The principle of direct laser writing

In general, the main principle of direct laser writing is described in figure 5.2. Tightly focused laser pulses induce permanent photomodification in the high

intensity region at the focal spot. The shape of the focal region defined by a constant-intensity surface is ellipsoidal, with the long axis pointing along the optical axis of the focusing microscope objective. For tight focusing with an objective lens NA=1.4, the elongation ratio is $\frac{\text{big-axis}}{\text{small-axis}} \simeq 2.8$. Drawing continuous lines by focal spot or sample translation results in photomodified patterns. After development, these patterns become transformed into solid features. Their diameter can be adjusted by varying the laser beam intensity.

5.2 Optical Characterization

5.2.1 Angle Resolved Transmittance Measurements

All transmittance spectra of the fabricated woodpile structures are measured by a home-built setup based on the one built up in reference [10]. Light of a Ti-Sapphire laser at 800nm of $\sim 180fs$ pulse duration with an energy of 1mJ/pulse at 1KHz repetition rate is tightly focused with an $f = 3cm$ lens into a 3cm long cell filled with distilled water in order to produce a white light continuum source [2] providing a broad spectral range of 450nm to 1000nm wavelength. The spectrum of the white light continuum is shown in figure 5.4. The light is coupled out and collimated by lens L2 and then, focused by Lens L3 onto the sample. The sample holder is fixed to a goniometer, which in turn is mounted on top of a rotation stage. The combination of rotation stage and goniometer offers the possibility to align the sample along the optical axis very accurately. Additionally, the sample can be rotated by an angle with respect to the optical axis. Furthermore, the whole combination is mounted on top of a three-dimensional translational stage to align the sample relative to the focus. Another lens L4 couples out the beam and in combination with lens L5 image the sample onto an intermediate image plane. Then, this intermediate image plane is further imaged onto a IR/VIS fiber with a core diameter of 200 μm (OF2) by lenses L7 and L8. The output of the fiber is connected to an optical spectrum analyzer (Ocean

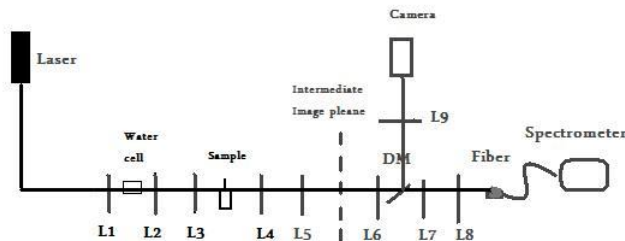


Figure 5.3: Optical characterization setup

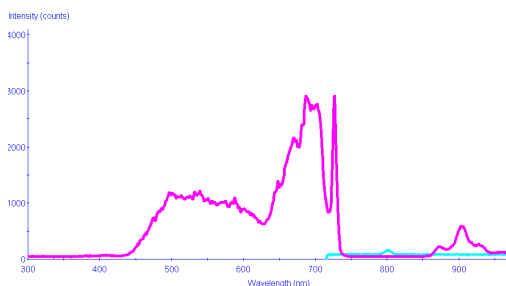


Figure 5.4: White light continuum spectrum

Optics S2000), covering a spectral range from 300 nm to 1000 nm wavelength. The spectrum is recorded through a Labview driven program in a PC. To ensure proper normalization, all the measured transmission spectra are normalized to the bare glass substrate for the same angle of incidence requiring only a very small lateral movement of the sample [10]. In order to align the sample appropriately on the optical axis, the intermediate image plane can be imaged onto a CCD camera using a dichroic mirror (DM). This also serves to remove the 800nm pump of the continuum, thus, avoiding saturation of the spectrum analyzer. The half-opening angle of the incident light is reduced down to 5° , which is assured by iris diaphragms.

5.2.2 Bragg Diffraction Measurements

The quality and rotational symmetry properties of the fabricated photonic crystals can be characterized by measuring the Bragg diffraction patterns. Photonic crystals, by definition, are periodic, therefore their Fourier transforms must also be periodic. The diffraction pattern can be regarded as the Fourier transform of the periodic array present in the photonic crystal, so that diffraction can be used so as to obtain the reciprocal lattice of a given

structure as has been done in X-Ray diffraction techniques. This allows one to orientate the crystal for probing the optical properties of the photonic crystal along high-symmetry directions in angle resolved measurements [17].

Diffraction patterns are built by a constructive interference of light scattered in directions other than the incident and specular ones. In a photonic crystal, the wave vector can take any form of $k_i + G$, where k_i is the initial wave vector and G denotes any reciprocal lattice vector. In the particular case of normal incidence, the parallel component of k_i is the null vector; however, the many possible values of G still provide the photon wave vector with a parallel component [19]. In the external medium, the angle of the exiting beam with respect to the normal is given by $\sin\varphi = \frac{k_{\parallel}}{k_{out}}$, where k_{\parallel} is the parallel component of the wave vector and it is a conserved quantity and $k_{out} = n_{ext} \frac{\omega}{c}$ is the modulus of the wavevector in the external medium. This imposes the following condition on the wave vector modulus out of the photonic crystal to observe the diffraction patterns: $k_{out} \geq k_{\parallel}$. To obtain a diffraction pattern from photons that propagate normally to the surface of the photonic crystal, the photons must couple with bands (eigenstates) that provide them with a non-null k_{\parallel} . This occurs when bands folded back into the first Brillouin zone by reciprocal lattice vectors not collinear with k_i are available [54]. In other words, in order to observe a diffraction pattern, a Bloch mode is required to exist, created by a non-collinear reciprocal lattice vector to which photons may couple. In general, for low energies (below the first stop band) only linear bands are available. This means that the latter condition imposes a minimum on the photon energy to produce diffraction patterns.

The experimental arrangement used to characterize the photonic structures is shown in figure 5.5. The relative orientation of the photonic crystal with respect to the source or the detector is described using a Cartesian reference system. The laser beam parallel to the z-axis defines a set of two incidence angles: the zenithal angle (Φ) and the azimuthal angle (Θ). The former is defined as the angle formed between the normal to the photonic crystal outer surface and the incident beam, whereas the latter is the angle formed between the longitudinal axis of the photonic crystal and the incidence plane (xz). The longitudinal axis of the woodpile structure coincides with the [100] direction of the surface lattice of the crystal, which is parallel to the x axis for $\Theta = 0^\circ$ and $\Phi = 0^\circ$. In front of the crystal, a screen is placed in such a

way that its normal coincides with the direction of the specularly transmitted channel.

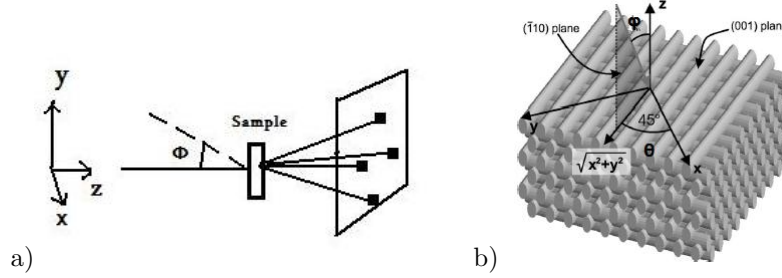


Figure 5.5: Experimental arrangement for Bragg diffraction characterization [56]

The woodpile structure, hence, presents the $\{001\}$ family of planes parallel to the crystal surface and the direction normal to these planes is called ΓX , which will be the one studied. As explained above, the first condition that must be satisfied in order to observe the diffraction patterns is that $k_{out} \geq k_{\parallel}$. In our case, the woodpile structure has a square symmetry in the planes *in between* the layers [52]. Thus, for the rod layers that are parallel to the xy plane for $\Theta_i = 0$ and $\Phi_i = 0$, a set of 2D primitive lattice vectors is $\vec{a}_1 = \frac{c}{2}(110)$ and $\vec{a}_2 = \frac{c}{2}(1-10)$, where c is the unit cell height and $\frac{c}{d} = \sqrt{2}$ with d , the inlayer rod distance. A set of primitive reciprocal lattice vectors can be chosen as: $b_1 = \frac{2\pi}{c}(110)$ and $b_2 = \frac{2\pi}{c}(1-10)$. So, any reciprocal lattice vector can be written as $\vec{g} = p\vec{b}_1 + q\vec{b}_2$, where (p, q) is a pair of integers. In normal incidence, when an incoming light beam travels in the positive z -axis direction, the wave vector of a diffracted beam emerging from the slab can be written as $K_g^{\pm} = g \pm \sqrt{k^2 - |g|^2}\vec{z}$, where the \pm sign corresponds to a transmitted (+)/ reflected (-) beam, $k = \frac{2\pi}{\lambda}$ is the magnitude of the incident wave vector and λ is the wavelength. Each diffracted beam corresponds to a propagating wave, if the z component of K_g^{\pm} is purely real. Then, diffraction channels are open when $|g| < k$ and we have a diffraction cutoff whenever $|g| = k$. For a square lattice, this condition reduces to [12]:

$$\vec{g} = p\vec{b}_1 + q\vec{b}_2 = \frac{2\pi}{c}p(\hat{x} + \hat{y}) + \frac{2\pi}{c}q(\hat{x} - \hat{y}) \Rightarrow$$

$$|\vec{g}| = \frac{2\pi}{c}\sqrt{(p+q)^2 + (p-q)^2}$$

and for $|g| = k$, we get:

$$\frac{c}{\lambda} = \frac{\sqrt{2}}{n} \sqrt{p^2 + q^2}$$

where n is the refractive index of the diffraction medium. In air ($n = 1$) four diffraction channels open corresponding to

$$(p, q) = (1, 0), (0, 1), (-1, 0), (0, -1)$$

when $\frac{c}{\lambda} > \sqrt{2} \Rightarrow d > \lambda$.

A second set of diffraction spots appears for

$$(p, q) = (1, 1), (1, -1), (-1, 1), (-1, -1)$$

when $\frac{c}{\lambda} > 2 \Rightarrow d > \sqrt{2}\lambda$.

The wave vectors of these diffracted beams are located along a cone and the angle φ between the K_g^\pm and the z axis is given by $\sin\varphi = \frac{\lambda}{d}$ by considering each layer within the photonic crystal as a two-dimensional diffraction grating [58]. This gives the angle φ of the first four diffracted beams as a function of the wavelength. The specularly reflected and forwardly transmitted beams corresponds to channel $(0, 0)$ which are always open channels. The fact that the photonic crystal is supported on a glass substrate ($n = 1.53$) introduces a first diffraction cut off for transmitted beams at $\frac{c}{\lambda} = \frac{\sqrt{2}}{1.53} = 0.924 \Rightarrow d > 0.653\lambda$. Although those beams are internally reflected at the glass-air interface and therefore do not propagate in air, they can be experimentally observed by frustrating total internal reflection. Since the diffracted wave vector K_g^\pm depends on the component of the incident wavevector parallel to the surface of the slab, the angular distribution of diffracted beams depends strongly on the tilt and rotation of the sample with respect to the incident beam [40]. When carrying out these measurements, the sample is oriented with respect to the diffraction plane by using the observed diffraction pattern.

5.3 Simulation

In order to compare our experimental results with theoretical expectations, the freely available MIT Photonic Bands (MPB) software package was used.

MPB is frequency-domain, that is, it does a direct computation of the eigenstates and eigenvalues of Maxwell's equations (using a planewave basis). Each field computed has a definite frequency, in contrast to time-domain techniques, such as Meep software, where Maxwell's equations are iterated in time: the computed fields have a definite time (at each time step) but not a definite frequency per sec. In general, time-domain methods are well suited to computing things that involve evolution of the fields, such as transmission, whereas frequency domain methods are better to calculate band structures and eigenstates.

A program named `woodpile.ctl` written in Scheme code, included in Appendix A, serves for the calculation of the bands for the case of a woodpile photonic crystal. A brief notation will be given below in order to state the main idea of the algorithm written and the way that it is related to those stated in theory. In general, the woodpile structure is generated by a superlayer made of two layers that are identical after rotation of 90° degrees of one of them. Each layer is made of two dielectric rods per unit cell. If c is the edge length of the associated cube, then the height of these layers is $\frac{c}{4}$. Maxwell's equations possess an important property, that is, they are *scale invariant*. If one multiplies all the sizes by 10, the solution scales are simply multiplied by 10 likewise. So, one can solve a problem once and apply that solution to all length-scales. For this reason, the main idea is to peak some fundamental length-scale c of a structure, such as its lattice constant (unit of periodicity), and write all distances in terms of that. In this sense, we choose this so that c is unity. Then apply this to any other physical system, one simply scales all distances by c . In this sense, the frequency eigenvalues returned by the program are in units of $\frac{c_0}{c}$, where c_0 is the speed of light and c is the unit of distance. Therefore, the corresponding vacuum wavelength is c over the frequency eigenvalue, i.e. $\lambda_0 = \frac{c}{\omega} \Rightarrow \omega = \frac{c}{\lambda_0}$.

The geometry of the woodpile structure is briefly stated as follows: the Bravais lattice of a photonic crystal is a face centered cubic (FCC) with crystal parameter $c = 1\mu m$ [lattice translations vectors: $\vec{a}_1 = \frac{c}{2}(0, 1, 1)$, $\vec{a}_2 = \frac{c}{2}(1, 0, 1)$, $\vec{a}_3 = \frac{c}{2}(1, 1, 0)$ and the primitive-cell contents can be described as two parallelepipeds: the first one, with origin $\vec{r}_1 = (0, 0, 0)$ with edge vectors $\vec{c}_1 = \frac{c}{2}(1, 1, 0)$, $\vec{c}_2 = \frac{c}{4}(0, 0, 1)$ and $\vec{c}_3 = \frac{c}{8}(-\sqrt{2}, \sqrt{2}, 0)$, and the second one, with origin $\vec{r}_2 = \frac{c}{4}(1, 1, 1)$ with edge vectors $\vec{c}_1 = \frac{c}{2}(1, -1, 0)$,

$\vec{c}_2 = \frac{c}{4} (0, 0, 1)$ and $\vec{c}_3 = \frac{c}{8} (-\sqrt{2}, \sqrt{2}, 0)$ [39]. Since the relative band gap width depends on both index contrast $\eta = \sqrt{\frac{\epsilon_s}{\epsilon_b}}$ and filling ratio $f = \frac{w}{d}$, these are the main relevant parameters that one has to consider as moves from one physical system to the other though retaining the same geometry. Keeping in mind those previously stated for the scale invariance, inside the program there are several variable parameters that can be defined by the user: the width of the rods w , the dielectric constant of the rods ϵ and the height of the rods h . All the length - related parameters are expressed in terms of the lattice constant c and are those that change as one moves from one length-scale to the other. The rest of the parameters related to the geometry of the unit cell remain the same. For example, if one wishes to calculate the band for a photonic crystal with an inlayer period $d = 500nm$ and refractive index $n = 1.5$, then what one has to do is simply rescale the above parameters according to the new unit cell (recall that the program is set by default to $c = 1$). Therefore, we calculate the filling ratio for these parameters: we set the width of the rods according to the experimental observations, i.e. $\sim 110nm$, so $f = \frac{w}{d} = \frac{110nm}{500nm} = 0.22 \Rightarrow \frac{w}{c} = 0.155$. Thus, the value of the width inserted into the program will be 0.155 expressed in units of the unit cell length. The same goes for the height of the rods: if we want to keep a ratio of $\frac{w}{h} = \frac{1}{3}$, which is approximately the theoretical ratio of the voxel parameters, then we have $h = 3w = 3 \times 0.155c = 0.465c$. And, finally, for the dielectric constant, we calculate $\epsilon = n^2 = 2.25$.

Hence, according to those stated above, we have calculated the bands for a woodpile structure with $\epsilon = 13$, $c = 1$, $\frac{w}{c} = 0.2$ and $\frac{h}{c} = 0.25$. The resulting band diagram is shown in figure 5.6, where we define the frequency eigenvalues

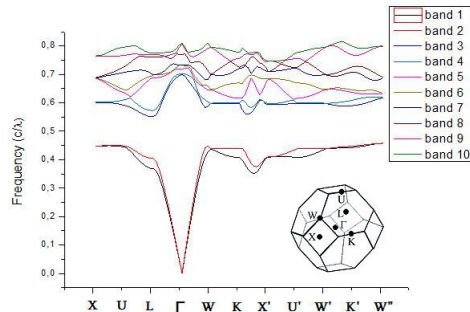


Figure 5.6: The band structure for a woodpile photonic crystal

along the y - axis in dimensionless units of $(\frac{c}{\lambda})$ and the k wavevector along the x - axis for a path along high symmetry points within the irreducible Brillouin zone of the diamond lattice (shown in the lower right corner of the figure). The structure presents a complete photonic band gap located between the second and third band, as expected. In our case, since the applied polymers have a refractive index of only $n = 1.49$ to $n = 1.63$ (as we will show in a following chapter) the fabricated structures possess photonic band gaps in certain directions.

Next, in order to visualize light propagation inside the woodpile structure, we have utilized the freely available visualization tool VisIt 1.12 in combination with the MPB platform to calculate the time-averaged electric-field energy density for the first four bands at the X point (figure 5.7). In figure 5.7a, the dielectric function is depicted from a general point of view indicating that the structure clearly resembles to a woodpile one, as expected. Next, in figures 5.7b and 5.7c, the two lowest bands are shown accordingly. They have their fields concentrated within the rods in order to minimize its frequency, flowing along more-or-less along linear paths. The second band differs from the first mainly by the orientation of its field paths. The fields for the first band at X point are shown with the strongest fields (highest energy density) represented as the red colored pixels, whereas the weakest fields (lower energy density) as blue colored pixels. The color scale is depicted as an inset at the upper left side of each picture. The first band above the gap is band $n = 3$. The field patterns are considerably harder to make out than for the lower band, but they seem to be more diffuse and ‘clumpy’, the latter indicating the expected field oscillations for orthogonality with the lower bands.

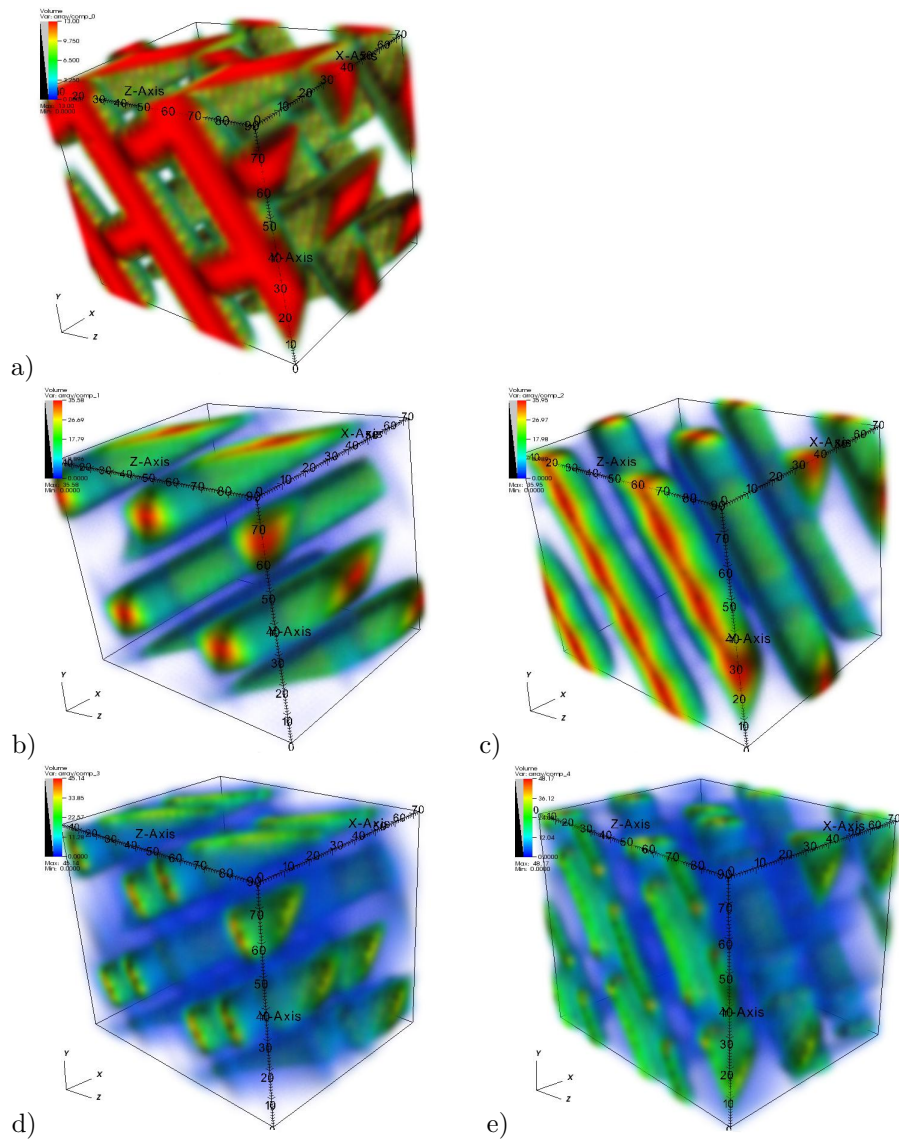


Figure 5.7: Visualizing the diamond lattice and bands a) general three dimensional view of the woodpile structure. Next, looking at the time averaged electric field energy density for the first four bands: b) $n = 1$, c) $n = 2$, d) $n = 3$, e) $n = 4$

6 Chapter 6: Linear Index Tuning of Titanium containing sol - gel composites

The synthesis of novel materials with adaptable and improved optical and mechanical properties is a critical issue for the fabrication of precise 3D photonic crystals. Titanium isopropoxide is chosen as an inorganic network former, since it incorporates two basic characteristics: a) transparency in the mid-IR suitable for two-photon polymerization and b) high refractive index for a full photonic band-gap. By changing the ratio of the metal alkoxide/titanium and the ratio of the precursor/titanium we are able to tune the refractive index of the resulting materials.

6.1 Titanium sol -gel composites

The sol-gel method, already described in chapter 3, will be used as the fabrication procedure. Inorganic – organic hybrids, which are materials typically produced by this method, have the ability to modify their properties by the incorporation of dopants or other functionalized groups. In our case, we will use a silicon hybrid material containing titanium (Si-O-Ti), which is known to strengthen the system, modify the refractive index and improve the mechanical stability when added to the precursor solution [43]. The doping process takes place via the reaction of silanol groups with TiOR groups, which affects the system as to reduce drying times and impart enhanced mechanical stability to deposited films [3]. This makes the cured material potentially stronger than conventional acrylate or epoxy resins. In general, mechanical properties of the material are described as a function of percentage of titanium.

The sol-gel film is fabricated from methacryloxypropyl trimethoxysilane and methacrylic acid (MAA), both of which have photopolymerizable C = C double bonds groups, and titanium n-propoxide $Ti(OPr)_4$ as an inorganic network former. In brief, the procedure followed is described as follows: Firstly, MAPTMS is hydrolyzed with dilute HCL and the mixture is left stirring for 30minutes. Next, in a second reaction vessel MAA and titanium isopropoxide $Ti(OPr)_4$ are combined in several mole ratios. Then, an equal volume of isopropanol is added to the chelated titanium and the sol is left stirring for another 30min. Finally, it is added dropwise to the hydrolyzed silane precursor (MAPTMS sol). This mixture is able to make a mineral and

an organic network as illustrated in figure 5.1. The mineral network (gel) is obtained through the hydrolysis and the polycondensation of alkoxide groups. The organics network is created by the polymerization of double bonds under UV exposure.

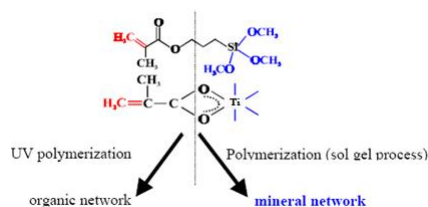


Figure 6.1: Mineral and organic network

In order to enhance the two-photon absorption rate, a standard amount of 1.5wt% (related to MAPTMS) of the photoinitiator Irgacure 369 is added to the mixture, which is left stirring for a day afterwards. The photoinitiator used, presents strong single photon absorption in the 320nm-420 nm region. Once the solution is ready, the sol-gel is spin-coated onto quartz substrates and the resultant gel films are prebaked at 100°C for an hour in order to remove solvents and give mechanical stability to the mineral network formed. Finally, the film is exposed for another hour under a UV lamp for the initiator to act (on the organic part). The UV polymerization process induces the conversion of small unsaturated molecules in the liquid state to solid macromolecules either through polymerization or through crosslinking. In the former case, macromolecules are created through chain reactions, while the latter case is concerned more with the formation of crosslinks with chemical bonds. Both cases result in a refractive index increase.

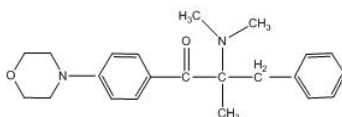
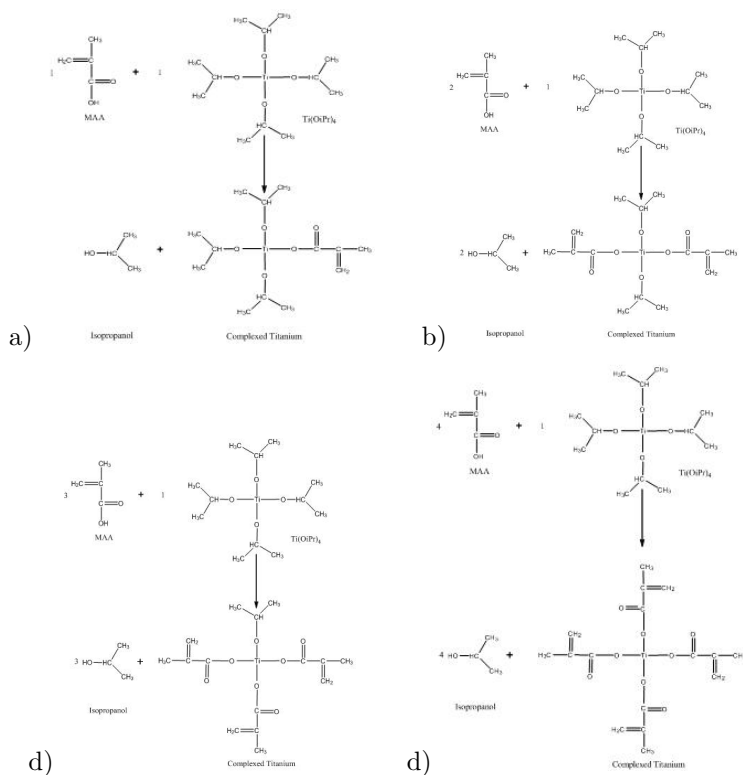


Figure 6.2: Irgacure 369

In order to investigate the processability and the refractive index variation of the resulting gel, the mole ratios of MAPTMS to $Ti(OPr)_4$ and of MAA to $Ti(OPr)_4$ were varied. In this sense, the mole ratio of MAPTMS to $Ti(OPr)_4$ varied from 9:1 until 1:9, whereas the mole ratios of MAA to $Ti(OPr)_4$ varied from 1:1 until 4:1. In every case, the mole ratio of MAA to



In general, when the $\text{MAA}:\text{Ti}(\text{OPr})_4$ ratio becomes higher, the number of acrylates ligands of the complex would be increased, with accruing the percentage of complex with four acrylate ligands [13]. The chelation of $\text{Ti}(\text{OPr})_4$ with MAA for mole ratios $\frac{\text{MAA}}{\text{Ti}(\text{OPr})_4} = \frac{2}{1}$ till $\frac{4}{1}$ lasted for 24 hours by continuous stirring. The mole ratio of MAA to $\text{Ti}(\text{OPr})_4$ 1:1 on the other hand, was left stirring for 15 minutes. Otherwise, the solution became saturated and precipitation occurred.

From the mixture of partially hydrolyzed MAPTMS with the complexed titanium, hydrolysis of titanium (if any isopropyl groups remained) occurs due to the presence of HCl.

- C)Hydrolysis of Titanium

6.1.1 Materials preparation process

As already mentioned, our main scope is to investigate the influence of the $Ti(OPr)_4$ and MAA content on the structurability and the processing of MAPTMS-based composites. The $\frac{MAPTMS}{Ti(OPr)_4}$ mole ratio was varied systematically from 9:1 to 1:9 and the $\frac{MAA}{Ti(OPr)_4}$ ratio from 1:1 to 4:1 resulting in 36 different MAPTMS, TIP, and MAA combinations. The quantities for each material were calculated as follows:

Initially, we choose a fixed final volume for the solution, so let's set it to 2ml.

$$\text{Then, we have: } V_{MAPTMS} + V_{MAA} + V_{Ti(OPr)_4} = 2ml \quad (6.1)$$

In sequence, we set the mole ratios of the organic and inorganic moieties:

$$\frac{n_{MAA}}{n_{Ti(OPr)_4}} = \frac{A}{B} \quad \text{and} \quad \frac{n_{MAPTMS}}{n_{Ti(OPr)_4}} = \frac{C}{D} ,$$

$$\text{where } \frac{A}{B} = \frac{1}{1}, \frac{2}{1}, \frac{3}{1}, \frac{4}{1} \quad \text{and} \quad \frac{C}{D} = \frac{9}{1}, \frac{8}{2}, \frac{7}{3}, \dots, \frac{2}{8}, \frac{1}{9}$$

Hence, in general we get:

$$\frac{n_{MAA}}{n_{Ti(OPr)_4}} = \frac{\frac{V_{MAA}d_{MAA}}{MB_{MAA}}}{\frac{V_{Ti(OPr)_4}d_{Ti(OPr)_4}}{MB_{Ti(OPr)_4}}} = \frac{A}{B} \Rightarrow V_{MAA} = \frac{A}{B} \frac{d_{Ti(OPr)_4} MB_{MAA}}{d_{MAA} MB_{Ti(OPr)_4}} V_{Ti(OPr)_4} \quad (6.2)$$

$$\begin{aligned} \frac{n_{MAPTMS}}{n_{Ti(OPr)_4}} &= \frac{\frac{V_{MAPTMS}d_{MAPTMS}}{MB_{MAPTMS}}}{\frac{V_{Ti(OPr)_4}d_{Ti(OPr)_4}}{MB_{Ti(OPr)_4}}} = \frac{C}{B} \Rightarrow V_{MAPTMS} = \\ &\frac{C}{D} \frac{d_{Ti(OPr)_4} MB_{MAPTMS}}{d_{MAPTMS} MB_{Ti(OPr)_4}} V_{Ti(OPr)_4} \quad (6.3) \end{aligned}$$

where d represents the density and MB the molecular weight.

Thus, we have formed a set of three equations with three unknown quantities. By substituting the known parameters for each material, we can construct the following four tables:

$$d_{MAPTMS} = 1.015 \frac{gr}{ml}, \quad MB_{MAPTMS} = 248.1 \frac{gr}{mol}, \quad d_{Ti(OPr)_4} = 0.955 \frac{gr}{ml}$$

$$MB_{Ti(OPr)_4} = 284.26 \frac{gr}{mol}, d_{MAA} = 1.015 \frac{gr}{ml}, MB_{MAA} = 86.1 \frac{gr}{mol}$$

MAPTMS (ml)	HCl (gr)	Ti(OiPr) ₄ (ml)	MAA (ml)	Isopropanol (ml)	Irgacure 369 (gr)
[90%] 1.710	0.1710	0.228	0.065	0.176	0.0244
[80%] 1.444	0.1444	0.433	0.123	0.176	0.0206
[70%] 1.204	0.1204	0.619	0.176	0.176	0.0172
[60%] 0.986	0.0986	0.789	0.225	0.176	0.0141
[50%] 0.786	0.0786	0.944	0.269	0.352	0.0112
[40%] 0.603	0.0603	1.086	0.310	0.352	0.0086
[30%] 0.435	0.0435	1.218	0.347	0.352	0.0062
[20%] 0.279	0.0279	1.339	0.382	0.352	0.0019
[10%] 0.134	0.0134	1.452	0.414	0.352	0.0016

Table 6.1: Titanium sol - gel composite with mole ratio $\frac{n_{MAA}}{n_{Ti(OPr)_4}} = \frac{1}{1}$

MAPTMS (ml)	HCl (gr)	Ti(OiPr) ₄ (ml)	MAA (ml)	Isopropanol (ml)	Irgacure 369 (gr)
[90%] 1.650	0.1650	0.220	0.125	0.176	0.024
[80%] 1.360	0.1360	0.408	0.233	0.176	0.019
[70%] 1.107	0.1107	0.569	0.324	0.176	0.016
[60%] 0.887	0.0887	0.709	0.404	0.176	0.0127
[50%] 0.693	0.0693	0.832	0.474	0.352	0.0100
[40%] 0.523	0.0523	0.941	0.536	0.352	0.007
[30%] 0.382	0.0382	1.070	0.610	0.352	0.005
[20%] 0.234	0.0234	1.125	0.641	0.352	0.0033
[10%] 0.111	0.0111	1.203	0.686	0.352	0.0016

Table 6.2: Titanium sol - gel composite with mole ratio $\frac{n_{MAA}}{n_{Ti(OPr)_4}} = \frac{1}{2}$

MAPTMS (ml)	HCl (gr)	Ti(OiPr) ₄ (ml)	MAA (ml)	Isopropanol (ml)	Irgacure 369 (gr)
[90%] 1.605	0.1605	0.214	0.183	0.176	0.022
[80%] 1.287	0.1287	0.385	0.329	0.176	0.018
[70%] 1.023	0.1023	0.526	0.450	0.176	0.015
[60%] 0.805	0.0805	0.644	0.551	0.176	0.0115
[50%] 0.620	0.0620	0.744	0.636	0.352	0.009
[40%] 0.461	0.0461	0.827	0.709	0.352	0.007
[30%] 0.323	0.0323	0.904	0.773	0.352	0.005
[20%] 0.202	0.0202	0.969	0.828	0.352	0.003
[10%] 0.095	0.0095	1.027	1.878	0.352	0.0013

Table 6.3: Titanium sol - gel composite with mole ratio $\frac{n_{MAA}}{n_{Ti(OiPr)_4}} = \frac{1}{3}$

MAPTMS (ml)	HCl (gr)	Ti(OiPr) ₄ (ml)	MAA (ml)	Isopropanol (ml)	Irgacure 369 (gr)
[90%] 1.553	0.1553	0.207	0.236	0.176	0.022
[80%] 1.217	0.1217	0.365	0.416	0.176	0.017
[70%] 0.915	0.0915	0.489	0.557	0.176	0.014
[60%] 0.738	0.0738	0.590	0.661	0.176	0.011
[50%] 0.561	0.0561	0.673	0.767	0.352	0.008
[40%] 0.412	0.0412	0.742	0.846	0.352	0.006
[30%] 0.286	0.0286	0.801	0.913	0.352	0.004
[20%] 0.178	0.0178	0.852	0.971	0.352	0.0025
[10%] 0.083	0.0083	0.896	1.021	0.352	0.001

Table 6.4: Titanium sol - gel composite with mole ratio $\frac{n_{MAA}}{n_{Ti(OiPr)_4}} = \frac{1}{4}$

6.1.2 Measurement of the linear refractive index

The refractive index of the sol-gel films was measured by means of an m-line prism coupling experiment. The refractive index and the thickness of a light-

guiding film are obtained simultaneously by measuring the coupling angles at the prism and fitting them through certain scaling rules for thin film optical waveguides. The experimental arrangement used for this purpose is shown below:

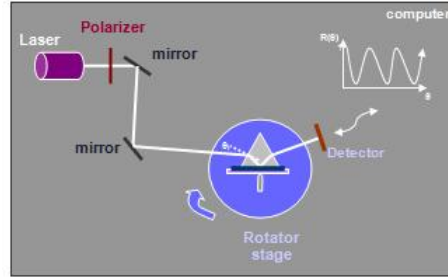


Figure 6.8: Prism-film coupler set-up

By means of a spring-loaded clamp, the film is pressed against the base of a coupling prism. A laser beam, linearly polarized (TE or TM) by a polarizer, is directed through a system of lens and apertures onto the prism face, so that the beam coincides with the prism base. The point where the beam strikes the prism base is the coupling spot [71]. At this point, the parameters n and film thickness are being measured. The prism sits on a yz translation stage that is mounted on a precision (~ 1 arcmin) rotary table or goniometer for the measurement of the incidence angles. For a calibration of the zero point of the angular scale we determine the position of the stage at which the beam is incident normally on the entrance face of the prism i.e. where the reflection from the front face of the prism goes back exactly into the incident beam. The angles of incidence on the entrance face of the prism are assigned positive or negative depending on whether the scale on the turntable increases clockwise or anticlockwise.

In our setup, we will use an He-Ne laser at 632nm, an SF6 optical glass prism with refractive index $n_P = 1.79884$, prism angle $\varepsilon_P = 60^\circ$ and quartz substrates for our films to be deposited on with a refractive index $n_s = 1.45702$. The value of the refractive index for the film and the prism at 632.8 nm wavelength is obtained according to the Sellmeier equation [see Appendix].

The film constitutes an ideal waveguide and therefore, is mounted on the rotating stage in order to measure the synchronism angles and subsequently the effective refractive index according to the equation

$$\frac{\beta}{k} = n_p \cos \left[(90^\circ - \varepsilon) + \sin^{-1} \left(\frac{\sin a}{n_p} \right) \right]$$

where a is the incidence angle, β is the effective refractive index. The effective guide index $N = \frac{\beta}{k}$ and the effective guide thickness can be determined for any slab-guide configuration by the introduction of appropriately normalized parameters and associated scaling rules, so that the number of independent parameters can be reduced. One of the basic guide parameters to be used is the normalized frequency or film thickness V , defined as [32]:

$$V = kf \left(n_f^2 - n_s^2 \right)^{\frac{1}{2}} \quad (6.4)$$

A second basic parameter introduced is that for the index asymmetry of the waveguide structure, a , where

$$a = \frac{(n_s^2 - n_c^2)}{(n_f^2 - n_s^2)} \quad (6.5)$$

This measurement is defined in a somewhat different way for the TE and the TM modes, and its values can range from zero for perfect symmetry ($a = 0$ if $n_s = n_c$) to infinity for strong asymmetry ($a \rightarrow \infty$ if $n_s \neq n_c$ and $n_s \rightarrow n_f$). We consider, in our case, asymmetric slab waveguides where the propagation constant β of the guide and the related effective refractive index are determined by the dispersion relation (4.27) rewritten as

$$\kappa f = m\pi + \Phi_s + \Phi_c, \quad m = 0, 1, 2 \dots \quad (6.6)$$

which is the basis for our discussion. Here m is the mode number, Φ_s and Φ_c are the phase shifts associated with total internal reflection from the film-substrate and film-cover interfaces, f is the film thickness and κ is the transverse propagation constant given by

$$\kappa^2 = k^2 \left(n_f^2 - N^2 \right) \quad (6.7)$$

To determine the phase shifts and the effective guide width we also need the decay constants γ_s and γ_c in substrate and cover, which are given by:

$$\gamma_s^2 = k^2 (N^2 - n_s^2) \quad (6.8)$$

$$\gamma_c^2 = k^2 (N^2 - n_c^2) \quad (6.9)$$

It is also convenient to use a parameter b which is called the normalized guide index defined by:

$$b = \frac{(N^2 - n_s^2)}{(n_f^2 - n_s^2)} \quad (6.10)$$

$$N^2 = n_s^2 + b(n_f^2 - n_s^2) \quad (6.11)$$

Assuming that $n_s \geq n_c$ this normalized index takes on values between zero and unity. At the cutoff of the guide we have $N = n_f$ and $b = 1$. In the case of TE modes, the formulas for the phase shifts Φ_s and Φ_c are:

$$\tan \Phi_s = \frac{\gamma_s}{\kappa} \quad (6.12)$$

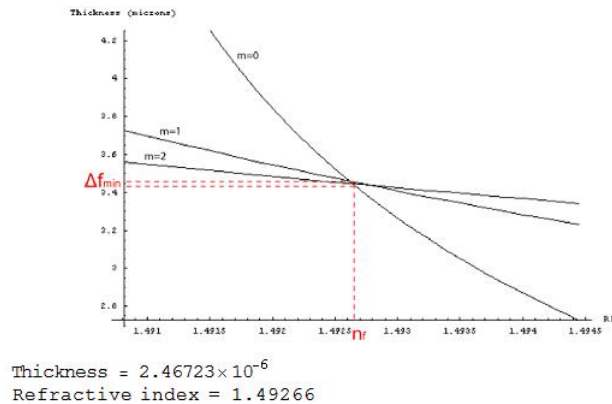
$$\tan \Phi_c = \frac{\gamma_c}{\kappa} \quad (6.13)$$

We use these formulas together with equations (5.7)–(5.9) and the definitions for V and b , to rewrite the dispersion relation in the normalized form:

$$V(1 - b) = m\pi + \tan^{-1} \left[\frac{b}{(1-b)} \right]^{\frac{1}{2}} + \tan^{-1} \left[\frac{(b+a)}{(1-b)} \right]^{\frac{1}{2}} \quad (6.14)$$

This form indicates that the guide index $b = (V, a)$ depends on only two independent parameters: the normalized thickness V and the asymmetry measure a . A program named SLABv3.m written in Mathematica code, included in Appendix B, serves for the calculation of the thickness and the refractive index of our thin film. A briefly notation will be given below in order to state the main idea of the algorithm written and the way that it is related to those stated in theory. For convenience, we consider the case of TE modes.

Therefore, for each incident synchronous angle of the light beam at the prism entrance face, the program calculates through the relation (1.28) (the function βF in the code) the effective refractive index related to each excited mode. According to the above formulation and using the values for each effective refractive index, we get for each mode, through equation (5.14), a value for the effective thickness V , and thus a value for the thickness f of the film using equation (6.4) (the function te in the code). However, since in equation (6.4) the refractive index of the film (n_f) is an unknown parameter, the code is programmed to run within a range of possible values for the n_f in the region of the value previously obtained for the 0th order effective index (function $teModes$). In accordance to this, a range of values for the thickness of the film is obtained for each mode. The variance of the several $f_{m,i}$ is then calculated and minimized afterwards in order to find the minimum difference between the f_m obtained [78]. Next, the minimum variation is applied to the effective index of the 0th order, thus a value for the film index is approximated. A diagram of the thickness versus the refractive index is plotted afterwards for each mode, where each curve represents the dispersion of the thickness for a range of values n_f near the region of the film refractive index calculated previously. The desired solution ($n, thickness$) corresponds to the point of intersection of the curves associated with each mode [48]. The value for the thickness given in the end is calculated by the *Mean* of the various f_i obtained for each mode. In this manner, the output of the program we get after executing the code, has the form shown below. Note that the mode with the largest angle a of incidence has the lowest mode number.

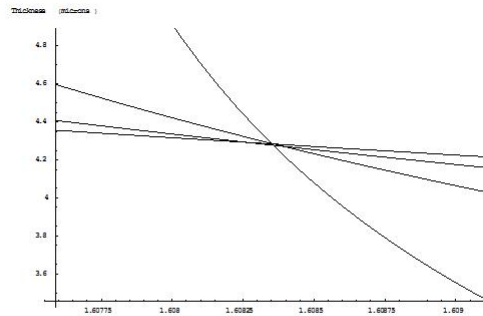


In order to get an approximation of our film's refractive index, at least three modes need to be supported by our waveguide. A minimum two are needed in order to make an intersection point for the two unknown parameters Thickness – Refractive Index and the third one to validate the minimum variance between them. The red colored values introduced in the output plot, indicate the region of minimum variance.

Considering those stated above, the calculated synchronous angles for the case of $\frac{MAPTMS}{Ti(OPr)_4} = \frac{2}{8}$ and $\frac{MAA}{Ti(OPr)_4} = \frac{2}{1}$ are given below:

θ_1	θ_2	θ_3	θ_4
-5.91667	-5.333333	-4.366667	-3.05

The values are entered in the program SLABv3.m, according to the methodology proposed in section 4.1, the output of which is given below:



Thickness = 4.28268x10⁻⁶
Refractive index = 1.60835

Note, also, that the angles measured by the goniometer are given in arcmins, thus, we have to convert each value in degrees in order to enter them in the program. The rest of the results that we have calculated for the refractive indices of all the samples are demonstrated below:

MAPTMS:Ti(OiPr) ₄	Ti(OiPr) ₄ :MAA	Ti(OiPr) ₄ :MAA	Ti(OiPr) ₄ :MAA	Ti(OiPr) ₄ :MAA
	1:1	1:2	1:3	1:4
	Refractive index	Refractive index	Refractive index	Refractive index
9:1	1.50639	1.50258	1.49959	1.49729
8:2	1.53876	1.50661	1.51296	1.51233
7:3	1.53790	1.53035	1.53300	1.53392
6:4	1.56277	1.54538	1.55279	1.55091
5:5	1.59152	1.56263	1.56196	1.57428
4:6	1.59200	1.58979	1.59251	1.59612
3:7	1.59205	1.60579	1.60406	1.60268
2:8	1.59205	1.60835	1.60911	1.62016
1:9	1.59340	1.63461	1.62971	1.63238

The data collected above are shown schematically in the following graph:

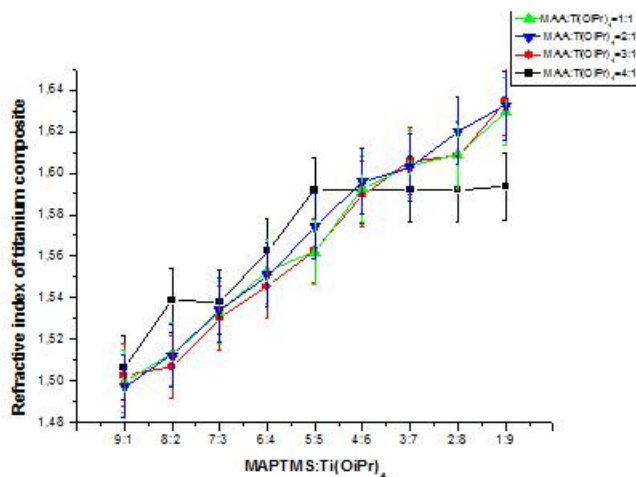


Figure 5.9: Refractive index dependence on the $Ti(OPr)_4$ content of the composite for four different $\frac{MAA}{Ti(OPr)_4}$ mole ratios

As we can see from the graph above, a linear increase of the refractive index of the material from 1.5 to 1.63 is observed when the concentration of $Ti(OPr)_4$ increased from 10 to 90%. This is attributed to the higher refractive index of the titanium oxide present in the material. Moreover, the observed increase of the refractive index is independent of the $\frac{MAA}{Ti(OPr)_4}$ mole ratio suggesting

that the effect of $Ti(OPr)_4$ on the refractive index overcomes the influence of the organic component of the material and allows one to tune the organic-inorganic content of the composite without changing its refractive index. A deviation was found for the composites with a $\frac{MAA}{Ti(OPr)_4} = \frac{1}{1}$.

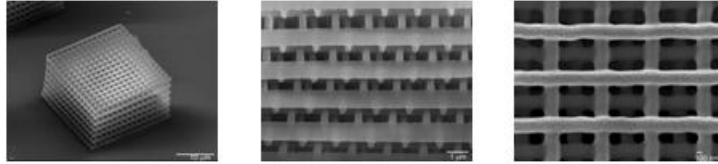


Figure 5.10: Titanium photonic crystals

In general, the range of the refractive index increment is over 0.1 which is promising for the use of such composite materials in the development of photonic components. In all cases, it was possible to produce good quality thin films, however, once the TIP content exceeded 50% relative to MAPTMS, the material became insoluble in any common solvent. This was independent of the degree of complexation of TIP by the MAA and hence, in a latter processability step, 3D structures could only be fabricated using MAPTMS:TIP mole ratios varying from 6:4 to 9:1 (shown in figure 5.10).

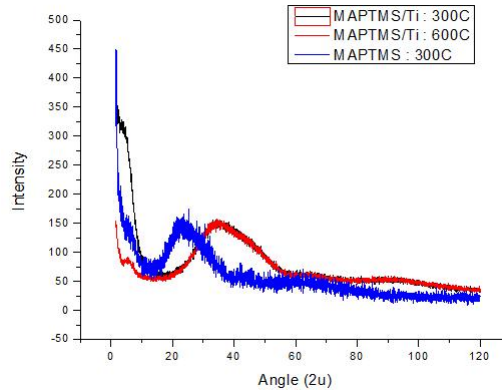


Figure 5.10: XRD patterns of the composite films with $\frac{MAPTMS}{Ti(OPr)_4} = \frac{5}{5}$ and $\frac{MAA}{Ti(OPr)_4} = \frac{1}{1}$ heated at $300^\circ C$ and $600^\circ C$ and MAPTMS only

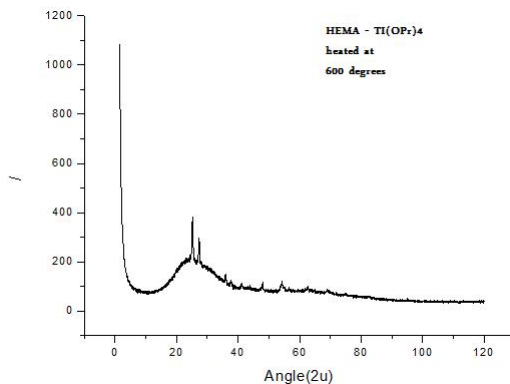


Figure 5.11: XRD patterns of a composite film with $\frac{HEMA}{Ti(OPr)_4} = \frac{5}{5}$ and $\frac{MAA}{Ti(OPr)_4} = \frac{1}{1}$ heated at $600^\circ C$

XRD was used to examine the possible formation of crystalline TiO_2 in the composite after heating at elevated temperatures. Figure 5.10 shows the XRD diffraction patterns of the composite films prepared with a $\frac{MAPTMS}{Ti(OPr)_4} = \frac{5}{5}$ and $\frac{MAA}{Ti(OPr)_4} = \frac{1}{1}$ mole ratios and heated at $300^\circ C$ and $600^\circ C$. This composite was chosen because it had the higher TIP and the lower organic content while being photostructurable. The broad peak between 20° and 50° is assigned to the polymeric material, since it appears in pure MAPTMS as well. However, the absence of sharp peaks at around 25° and 27° , which are characteristic of the crystalline anatase and rutile structure of titanium oxide [51], suggests that no crystalline TiO_2 is formed even upon heating the material above the decomposition temperature of the organic component. On the other hand, the formation of crystalline TiO_2 of both anatase and rutile form was observed for a composite comprising an organic photopolymerizable monomer, 2 - hydroxyethyl methacrylate (HEMA) and the Ti - MAA complex at a $\frac{HEMA}{Ti(OPr)_4} = \frac{5}{5}$ and a $\frac{MAA}{Ti(OPr)_4} = \frac{1}{1}$ mole ratio after heating at $600^\circ C$ (figure 5.11). This is attributed to the absence of the silicon oxide network formation in the latter material, which allows for the formation of TiO_2 and suggests a good mixing of the two alkoxides, TIP and MAPTMS used in this study, leading to true silicon and titanium oxide composites [53]. This was also verified by measuring the refractive indices of the composites after heating at $600^\circ C$. The materials did not show any abrupt increase of the refractive index, which would be characteristic of TiO_2 , in agreement with the XRD results.

7 Chapter 7: High resolution 3D woodpile structures with a response in the visible range

Several groups have demonstrated their investigations towards the realization of true 3D photonic structures. However, the experimental realization of photonic crystals with a complete, 3D band-gap still remains a major challenge mainly limited by the spatial resolution and flexibility of current technologies. Kawata et al. [66] demonstrated a subdiffraction-limit spatial resolution of 120 nm using a Ti:sapphire laser ($\lambda = 780$ nm), whereas Deubel, Wegener et al [9] have successfully fabricated 3D woodpile structures with an inlayer periodicity of 800nm and a best lateral resolution of 150nm using the same laser. In addition, by introducing a novel multi - scan technique, Staude, Wegener et al [60] have managed to fabricate woodpile structures with rod spacing of 500nm. The same group has recently demonstrated body - centered cubic woodpile crystals with rod spacings as small as 450nm using a continuous-wave depletion laser operating at 532nm [67]. Haske et al [21] produced nanoscale features as small as 65nm by using a 520nm femtosecond pulsed excitation of a 4,4 bis(din-butylamino) biphenyl chromophore enabling the realization of woodpile structures with an in layer periodicity of 500nm. Recently, Sun Q. et al [63] have proposed a new fabrication method for micro-structuring by photo-polymerization with femtosecond laser pulses. This method involves the fabrication of freestanding and movable 3D photonic microstructures enclosed in a mesh-cage. A uniform shrinkage and the ability of structuring even closer to the polymerization threshold is achieved in relation to conventional fabricated structures. Herein, a novel hybrid zirconium - dmaema based material is used for the fabrication of precise woodpile structures with feature sizes of 100nm, inlayer periodicity of 400nm and optical response in the visible range of frequencies. In addition, a new method for high resolution micro-structuring is presented, which involves multiple exposures. Fabrication of micro-structures below the polymerization threshold is tuned depending on the number of exposure times. Angle-resolved transmission spectroscopy was employed to characterize the fabricated structures. Diffraction patterns obtained under white light continuum illumination demonstrate the high quality of our samples.

7.1 Zirconium - Dmaema sol - gel composites

Recently, zirconium/silicon composites have been widely used for structuring by two photon polymerization [1],[47]. It has been demonstrated that these materials are suitable for two photon polymerization fabrication since they exhibit the characteristic of minimal shrinkage during photopolymerization. No additional efforts such as precompensation or mechanical stabilization to avoid structural distortions are thus, necessary. In addition, by varying the material's inorganic content, it is possible to modify and tune its refractive index. In fact, it was shown that as the ZPO content increases (from 5:5 to 9:1 for MAPTMS:ZPO), so does the material's refractive index. In particular, this increase is linear and that greatly simplifies the material design criteria, as typically such increases are saturating so that the doping concentration becomes very critical.

Amines, on the other hand, are known physical quenchers of singlet oxygen [6]. A crucial component in all photopolymerization processes is the photoinitiator, which absorbs light and generates radicals capable of initiating chain growth polymerization. The photochemical behavior of photoinitiators such as benzophenone (BP), thioxanthone (THX), quinone etc in the presence of amines can be represented by a mechanism involving the electron transfer from the amine to the triplet photoinitiator. In particular, radicals are formed by a bimolecular process consisting of an excited chromophore and a tertiary amine as the coinitiator (H donor). DMAEMA has a higher oxidation potential of the amine due to the methyl substituents at the N atom.

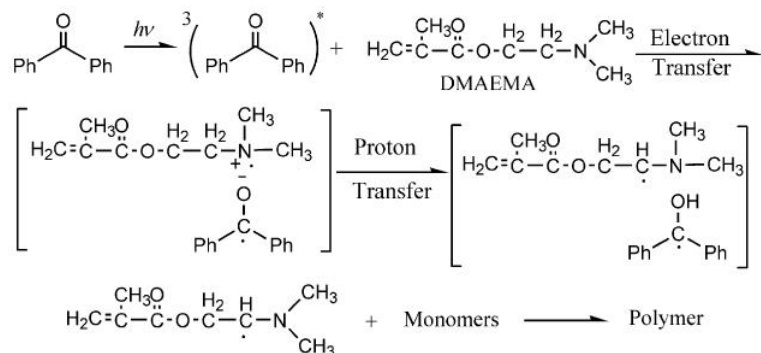


Figure 7.1: Initiation mechanisms for photoinitiators and coinitiator DMAEMA[72]

The BP/DMAEMA system produces free radicals either by electron transfer from DMAEMA to excited triplet state BP, followed by proton transfer, or by direct hydrogen atom subtraction from DMAEMA [72]. Because of the stronger electron-donating ability of the ethoxyl groups relative to the methyl groups in DMAEMA, the excited triplet BP and its derivatives may subtract hydrogen mainly from the methylene groups, and little from the methyl groups of dimethylamino groups of DMAEMA. The amine radicals, which originate from the decomposition of the charge transfer complex are the species that adds to the monomer. The radicals that lead to polymerization are those from the interaction of the BP triplet with the amine. The singlet deactivation leads to the polymerization inhibition. Thus, exploiting the advanced properties of zirconium as an inorganic network former and the quenching effects originating from DMAEMA has enabled us to fabricate high resolution woodpile structures with a response in the visible spectral range.

The procedure followed for the preparation of the zirconium - dmaema sol - gel is similar to the one described in the previous section for titanium containing composites. Initially, MAPTMS is hydrolyzed by HCl and then added to the solution of a zirconium (ZPO) 1:1 mixture with MAA. The mole ratios of MAPTMS:ZPO was varied from $\frac{7}{3}$ to $\frac{8}{2}$ and the mole ratio of the (ZPO+MAPTMS):DMAEMA from 95:5 to 90:10. The ratio of the metal alkoxide/zirconium and the ratio of the precursor/zirconium were chosen so, as they have given the best structures in previous experiments [47]. The mole ratio of ZPO:DMAEMA were investigated in such low percentages initially, since increasing the quantity of organic part results in a softer material lacking in structural integrity near threshold intensity. After stirring for 15 minutes, water was added in the mixture, which was left stirring until it becomes clear. Next, DMAEMA was introduced and finally, the photoinitiator 4,4-bis (diethylaminobenzophenone) was added to the mixture. In order to remove any aggregates, the solution was filtered through a $0.2\mu m$ pore size Millipore syringe filter. Samples were prepared by drop casting from solution onto a 120nm thick glass substrates and left for several days in air for gelation to take place. After the fabrication process, the samples were developed sequentially for some minutes in three different solvents:initially in 4-methyl-2-pentanone, then in 1-propanol and finally in dimethyl sulfoxide. Analytically, the step-by-step preparation of the Zirconium sol-gel matrix is

given as follows:

- A) *Hydrolysis of MAPTMS* using HCL as an acid catalyst

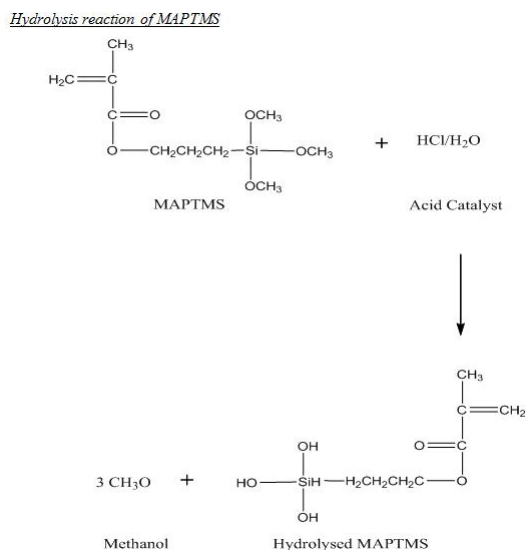


Figure 7.1: Hydrolysis of MAPTMS

- B) *Complexation of Zirconium*: zirconium propoxide (ZPO), $Zr(OPr)_4$ (70% solution in 1-propanol, Sigma-Aldrich), was used as an inorganic network former. $Zr(OPr)_4$ was complexed in a second bottle by adding methacrylic acid (MAA, Sigma-Aldrich) as a chelating agent in a mole ratio of 1:1. The mixture was stirred for 30 minutes.

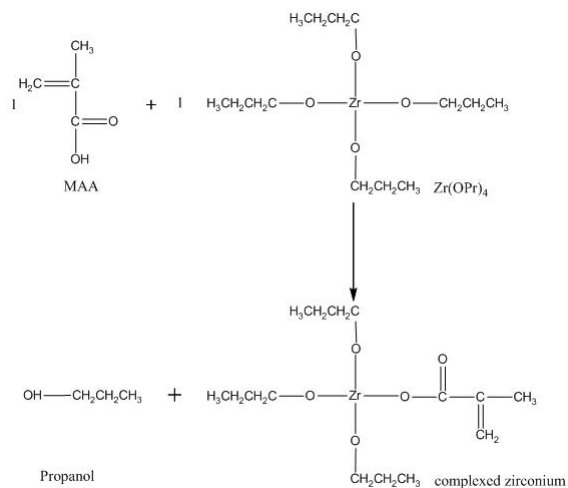


Figure 7.2: Complexation of Zirconium

- C) *Hydrolysis of Zirconium*: the partially hydrolyzed MAPTMS was added dropwise to the complexed ZPO following another 15 minutes of stirring. Afterwards water was added to the mixture in a molar ratio of *MAPTMS* : *H₂O* of 2.5:5. The additional quantity of water invoked hydrolysis in the remained Zr propoxide groups leading to Zr-OH groups.

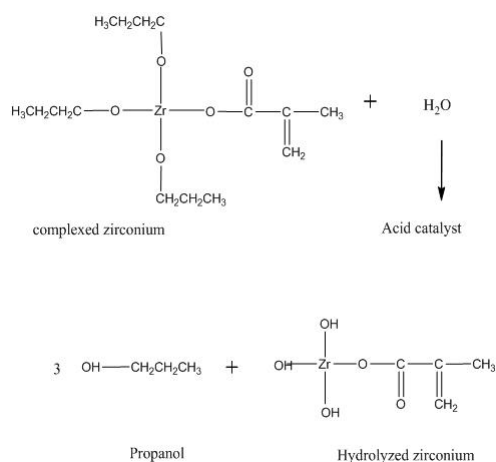


Figure 7.3: Hydrolysis of Zirconium

- D) *Condensation*: After the hydrolysis was over, DMAEMA and a photoinitiator (PI) was added to the mixture in sequence. The photoinitiator used is 4,4'-bis(diethylamino)benzophenone (Sigma-Aldrich), to 1.5% in the final solution. The mixture was stirred for 24 hours and the materials were filtered using 0.22 μm filters.

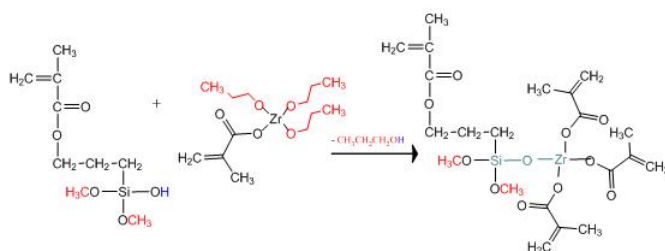


Figure 7.4: Condensation MAPTMS-Zirconium

7.1.1 Materials preparation process

In order to calculate the molar ratios of the components in the synthesis of the zirconium-dmaema composite, we follow the same procedure described in the previous chapter. Hence, for the case of

$$\frac{n_{MAPTMS}}{n_{ZPO}} = \frac{8}{2} \text{ and } \frac{n_{ZPO}}{n_{MAA}} = \frac{1}{1}$$

and for a final volume of the solution set to 2ml, as in the previous chapter, we get:

$$V_{MAPTMS} + V_{ZPO} + V_{MAA} = 2ml$$

$$\frac{n_{ZPO}}{n_{MAA}} = \frac{1}{1} \Rightarrow \frac{\frac{d_{ZPO}V_{ZPO}}{MB_{ZPO}}}{\frac{d_{MAA}V_{MAA}}{MB_{MAA}}} = \frac{1}{1} \Rightarrow V_{MAA} = 0.2739V_{ZPO}$$

where $MB_{MAA} = 86.1 \frac{gr}{mole}$, $d_{MAA} = 1.015 \frac{gr}{ml}$, $d_{ZPO} = 1.058 \frac{gr}{ml}$, $MB_{ZPO} = 327.58gr$

$$\frac{n_{MAPTMS}}{n_{ZPO}} = \frac{8}{2} \Rightarrow \frac{d_{MAPTMS}V_{MAPTMS}MB_{ZPO}}{d_{ZPO}V_{ZPO}MB_{MAPTMS}} = \frac{8}{2} \Rightarrow$$

$$V_{MAPTMS} = 3.204V_{ZPO}$$

where $d_{MAPTMS} = 1.015gr$, $MB_{MAPTMS} = 248.1 \frac{gr}{mole}$. Thus, we have a set of three unknown quantities ($V_{ZPO}, V_{MAA}, V_{MAPTMS}$) within three equations. Combining all the above, we can get: $V_{ZPO} = 0.5751ml$. In addition, Zirconium is contained in solution 70%wt in 1-propanol, thus we have:

$$V_{ZPO} = 0.5751ml \times 0.7 \frac{gr}{ml} = 0.4026ml$$

Therefore,

$$V_{MAA} = 0.2739 \times 0.4026ml = 0.1103ml$$

$$V_{MAPTMS} = 3.204 \times 0.4026ml = 1.2899ml$$

$$m_{HCL} = 0.12899 \text{ (HCL } 0.1M)$$

Next, in order to calculate the amount of DMAEMA: For example, consider the case of (ZPO+MAPTMS):DMAEMA=95:5, then we have:

$$\frac{n_{MAPTMS+nZPO}}{n_{DMAEMA}} = \frac{95}{5} \Rightarrow n_{DMAEMA} = 0.0065 \times \frac{5}{95} = 0.000342 \text{ mole}$$

$$V_{DMAEMA} = \frac{m}{d_{DMAEMA}} = \frac{n_{DMAEMA} \times MB_{DMAEMA}}{d_{DMAEMA}} = 0.0576 \text{ ml}$$

where $d_{DMAEMA} = 0.933 \text{ ml}$, $MB_{DMAEMA} = 157.22 \frac{\text{gr}}{\text{mole}}$. The amount of the water is calculated according to 10% vt to MAPTMS:

$$V_{H_2O} = \frac{0.304 \text{ ml}}{2.0972 \text{ ml}} 1.289 \text{ ml} = 0.1868 \text{ ml}$$

The amount of BIS added is 1.5% wt to MAPTMS+ZPO+DMAEMA:

$$m_{BIS} = \frac{0.01 \times (1.2899 + 0.1103 + 0.0576)}{0.7} = 0.0208 \text{ gr}$$

Following the same procedure, for the case of (MAPTMS + ZPO) : DMAEMA = 90 : 10, we have:

$$V_{DMAEMA} = 0.1217 \text{ ml}, m_{BIS} = 0.02174 \text{ gr}$$

Thus, we can construct the following table for the different mole ratios used relative to inorganic/organic and dmaema:

$\frac{n_{MAPTMS}}{n_{ZPO}}$	$\frac{7}{3}$	$\frac{7}{3}$	$\frac{8}{2}$	$\frac{8}{2}$
$\frac{n_{MAPTMS+nZPO}}{n_{DMAEMA}}$	$\frac{95}{5}$	$\frac{90}{10}$	$\frac{95}{5}$	$\frac{90}{10}$
MAPTMS (gr)	0.832	0.832	1.289	1.289
HCl (gr)	0.0832	0.0832	0.1289	0.1289
ZPO (ml)	0.4454	0.4454	0.4026	0.4026
MAA (ml)	0.122	0.122	0.1103	0.1103
H_2O (ml)	0.121	0.121	0.1868	0.1868
BIS (gr)	0.01423	0.0149	0.0208	0.02174
DMAEMA (ml)	0.04424	0.09	0.0576	0.1217

Table 7.1: Different mole ratios of MAPTMS:ZPO and DMAEMA

7.2 High resolution woodpile structures: the $\frac{c}{\lambda}$ challenge

Since the aspect ratio of a voxel is one of the most important parameters for high resolution fabrication via two-photon polymerization, the scheme of low laser power and long exposure time is adopted for the fabrication of precise woodpile structures in the present experimental procedure. As already mentioned in chapter 2, in order to fabricate high resolution photonic structures, fabrication near threshold energy is necessary. In particular, high spatial resolution can be achieved in the near threshold region of laser power, since the voxel length is more sensitive to the laser power than to the exposure time. The voxel length or in other words the $\frac{c}{\lambda}$ challenge is an essential parameter for high resolution fabrication of woodpile structures. To give a simple intuition on what we want to realize, suppose that one wishes to fabricate a woodpile structure with inlayer period of $d = 500nm$. This means that the unit cell height will be $c = \sqrt{2}d = 707nm$ leading to an interlayer distance of $\frac{c}{4} \simeq 177nm$ or the height of the rods to be less than $354nm$ ($h < \frac{c}{4} \times 2$) for partial interlayer overlapping to exist. This value is almost $\frac{1}{3}$ of the theoretical value of the $dof = 1.2\mu m$ given due to the laser wavelength and the imaging optics used. This fact presents a major constraint to the fabrication of woodpile structures with response in the optical spectral range.

In order to confirm the scheme mentioned above for the voxel aspect ratio, we have fabricated a set of woodpile structures sharing the same periodicity, though varying the exposure time and the laser power. In particular, we have made a series of them with a varying power from 4mW to 6mW with a step of 1mW and a varying exposure time or speed from $20\frac{\mu m}{sec}$ to $60\frac{\mu m}{sec}$ with a step of $10\frac{\mu m}{sec}$. The results obtained are schematically depicted below:

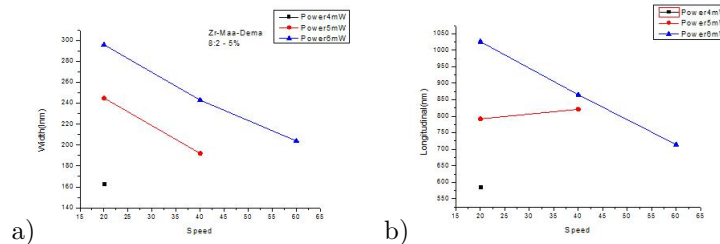


Figure 7.5: Width and Length of the voxel at varying power and exposure time

The material used was a zirconium-dmaema hybrid with mole ratio of $MAPTMS : ZPO = 8 : 2$ and $(MAPTMS + ZPO) : DMAEMA = 95 : 5$. As we can see from the two graphs above, the line width as well as the line length decrease while increasing the speed and decreasing the power. However, the minimum voxel size of $\sim 170nm$ width and $\sim 580nm$ length is clearly obtained for the minimum power and longer exposure time (i.e. minimum speed). In addition, increasing the speed while retaining the same power has led to structures that did not manage to survive developping. Thus, for the fabrication of high resolution woodpile structures, we have adopted the minimum scanning speed of our linear stage, set at $20 \frac{\mu m}{sec}$.

Next, several efforts have taken place in order to investigate the minimum unit cell achieved with such a zirconium - dmaema based material. Starting from large enough unit cells with inlayer periodicity of 1700nm going down to 900nm, the material has shown structures with good overall stability and a relatively easy fabrication as already published in previous experiments for the standard zirconium - based material [1, 47]. However, as one moves down to 700nm inlayer periodicity with a unit cell just below of $1\mu m$ and a relatively rod height needed less than 500nm, interlayer overlapping starts to play an important role to the overall integrity of the structure. The problem gets more pronounced as one goes further down to 500nm rod spacing, i.e. a unit cell of 707nm length and an interlayer spacing less than 350nm. Due to high filling fraction, developing comes into play as well. Conventional solvents do not manage to penetrate inside the complex 3D structure's net leading to the encapturement of the unpolymerized material within the first outer layers of the structure. Developing, thus, has played the second significant role for high resolution fabrication.

7.2.1 Multiple exposures scheme

A novel scheme was utilized for high resolution fabrication: that of multiple exposures. Since direct laser writing is a layer by layer method, multiple exposures involve the multiple scanning of every single layer of the desired microstructure. In particular, the scheme of minimum power and minimum exposure time (MPMP) is chosen for minimizing the aspect ratio of the voxels [37]. Initially, the first exposure is made according to the two scaling laws of voxels; the combination of low laser power and long exposure time, which is advantageous to the formation of low aspect ratio voxels near the

threshold energy. In our case, this condition is fulfilled for a scanning speed of $20 \frac{\mu m}{sec}$. For all the subsequent exposures, a minimum exposure time is applied, which is set to the scanning speed of $60 \frac{\mu m}{sec}$. In figure 7.6 we plot the minimum power - dependent number of exposure times for the fabrication of 3D woodpile structures with rods spacing varying from 700nm to 1500nm. As we can see, the minimum power for micro-fabrication by 2PP depends on

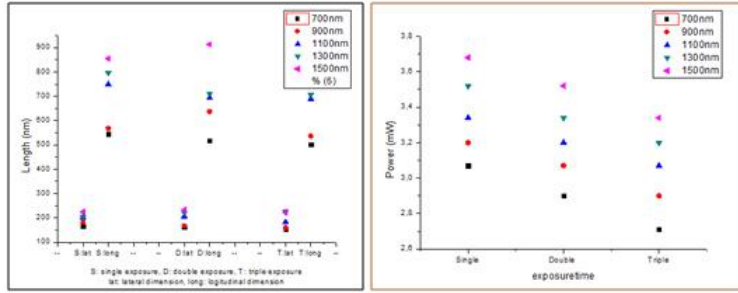


Figure 7.6: Multiple exposures scheme

the inlayer periodicity of the photonic structure in question for both single and multiple exposures. The polymerization threshold increases for smaller inlayer periodicity demonstrating that the topology of the structure favors mechanical stability against the destructive action of capillary forces during the wet development [31]. Mechanical stability with minimum irradiation power is, thus, achieved for greater inlayer periodicity either for single or multiple exposures. In addition, increasing the number of exposure times enables the tuning of the minimum polymerization energy for the desired structure. In our experiments, for the material we use, the fabricated structures could not survive intact when the pulse energy becomes smaller than 3.2mW for the case of 900nm inlayer periodicity. However, by increasing the number of exposure times to double or triple, the power needed for mechanically stable structures to be retrieved decreased to 3.07mW and 2.9mW, respectively. This, further leads to the improvement of the lateral spatial resolution achieved; from 183nm for single exposure to 167nm and 160nm for double and triple exposure respectively, as shown in figure 7.6 (left) and 7.7.a, b and c. Thus, tailoring the minimum energy needed for two-photon polymerization enables the fabrication of high resolution microstructures and makes multiple exposures a promising method for 2PP nanofabrication. However, since all the above results are based on SEM images, a statistical analysis need to be done in order to ensure reliable results beyond statistical error.

Furthermore, one has to measure the optical response of the structures fabricated with single and multiple exposures so as to ensure that this time consuming task really leads to a finer structure.

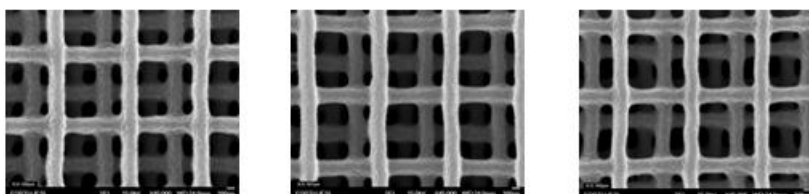


Figure 7.7: Woodpile with 900nm inlayer periodicity with
from left to right: single, double, triple exposures

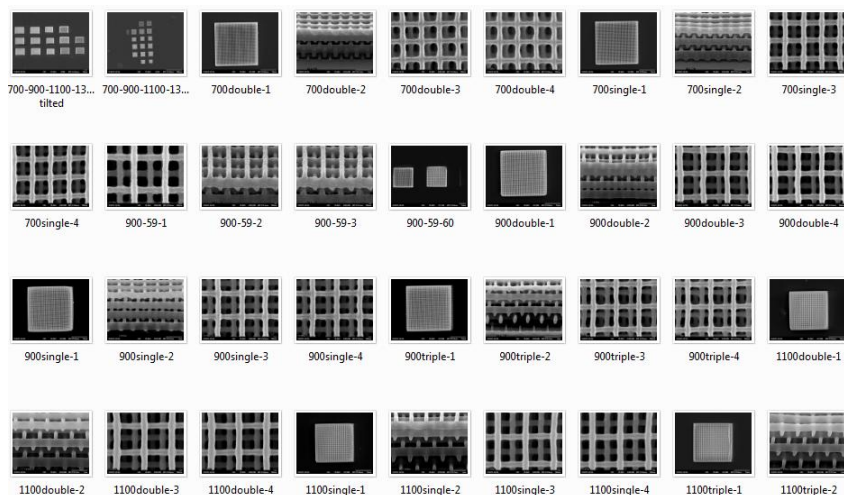


Figure 7.8a: Woodpiles with varying periodicity
700nm - 1100nm with multiple exposures

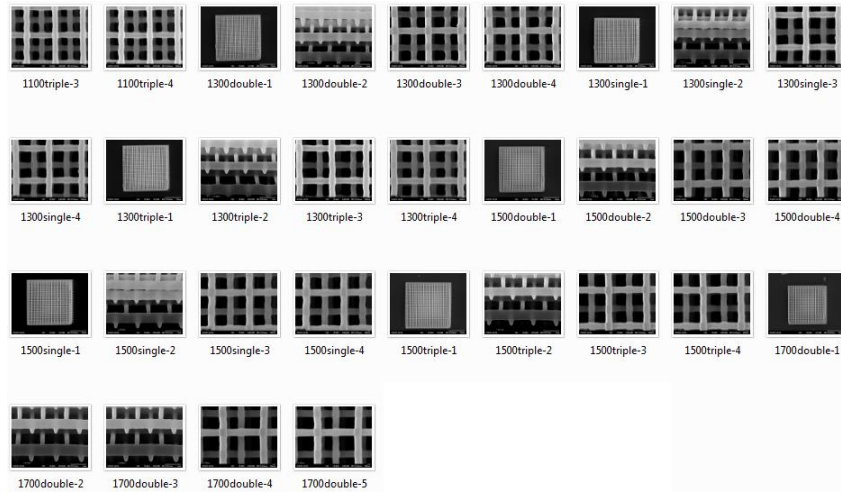


Figure 7.8b: Woodpiles with varying periodicity
1100nm - 1700nm with multiple exposures

Using multiple exposures scheme has enabled us to fabricate woodpile structures with an inlayer periodicity of 500nm and with feature sizes of 110nm (figure 7.8). As mentioned above, developing was a major constraint to high resolution fabrication. In general, the pattern collapse caused by capillary force exerted during development, rinsing, and drying steps is dependent on the wetting contact angle, the surface tension of the developer/rinsing solvent, and the pattern geometry. The use of supercritical drying or the selection of a solvent with a sufficiently large contact angle will provide a solution to high resolution fabrication [33]. However, in our case, conventional solvents such as 4-methyl-2 pentanone and isopropanol or either tetrahydrofuran, ethanol, dichloromethane individually or in combination with other solvents did not manage to penetrate the inner part of the structure due to high filling fraction. Thus, significant effort was made in order to find the correct combination among them. In fact, separately developing into 4-methyl-2-pentanone, 1-propanol and finally dimethyl sulfoxide has given the correct recipe. Any other combination or rearranging in a different sequence, even of the same solvents did not demonstrate any significant result.

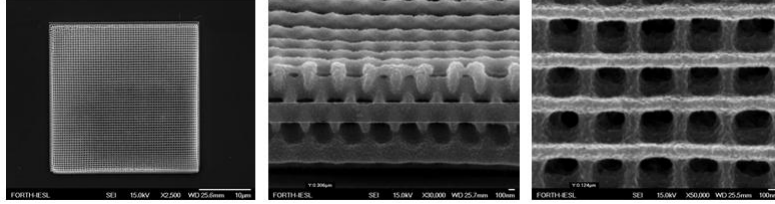


Figure 7.9: Woodpile with 500nm inlayer periodicity realized by triple exposures

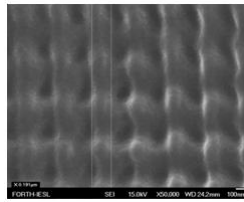


Figure 7.10: Woodpile with 400nm inlayer periodicity. Insufficient developing

7.2.2 High resolution woodpiles structures

Apart from developing, pushing the limit down to a unit cell close to the visible spectral range such as a woodpile structure with rod spacing of 400nm and a unit cell height of 565nm, higher precision stages are required. Our linear stage with a precision of 100nm is barely enough. So, instead of focal spot translation through an x-y galvanometric mirror scanner, 3D sample translation is adopted. Furthermore, in order to achieve the best structural resolution, a variation of inorganic/organic - dmaema mole ratio is realized. We have constructed a series of woodpiles with a constant inlayer period of 450nm for the four combinations mentioned in the previous section. We have chosen this value for the inlayer periodicity as the threshold structural parameter, since the problems already mentioned above are even more pronounced in the case of 400nm rod spacing and cannot be overcome with the methods currently used. This change in the structuring process has two benefits: a) laser power is delivered homogeneously to the sample rather than changing the acceptance angle as in the case of an x-y galvanometric scanner and b) enables the fabrication of large area photonic structures. The former advantage has resulted in precise fabrication of 3D woodpile structures with rod spacing of 500nm without the need of multiple exposures scheme. The latter led to enhanced signal recording.

Three combinations were chosen: $MAPTMS : ZPO = \frac{7}{3}$ for $(MAPTMS + ZPO) : DMAEMA = \frac{95}{5}, \frac{90}{10}$ and $(MAPTMS : ZPO = \frac{8}{2})$ for $(MAPTMS + ZPO) : DMAEMA = \frac{95}{5}$. Among them, only the last combination has given the best result shown in figure 7.11 below:

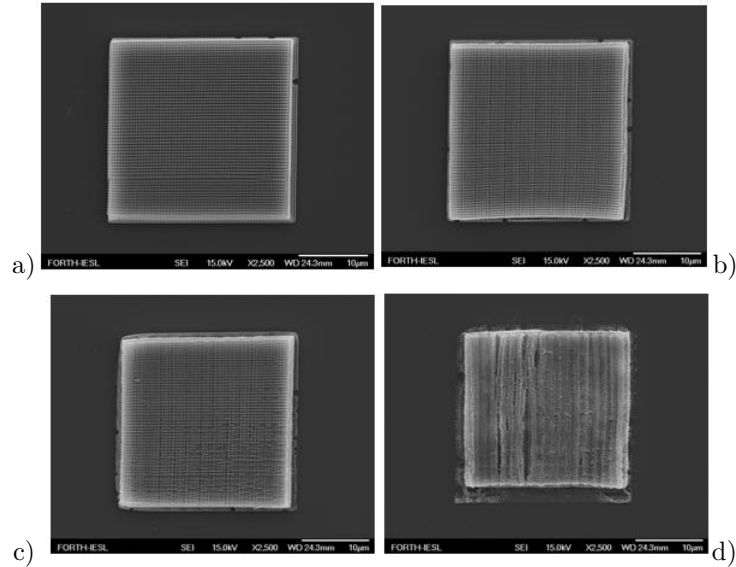


Figure 7.11: Woodpile 450nm inlayer periodicity $\frac{MAPTMS}{ZPO} = \frac{8}{2}$, $\frac{MAPTMS+ZPO}{DMAEMA} = \frac{95}{5}$ for various laser powers a)2.3mW, b)2.2mW, c)2.1mW and d)2.0mW

SEM images reveal the high quality of the samples. Working near threshold for various energies starting at a power of 2.3mW upper left decreasing with a step of 0.1mW, has enabled high resolution fabrication of $0.90\mu\text{m}$ features widths at laser power of 2.3mW. As the energy is decreasing, deformations of the structures due to shrinkage effects after developing become obvious. The structural deformation in the transition layer is detrimental to high precision microfabrication.

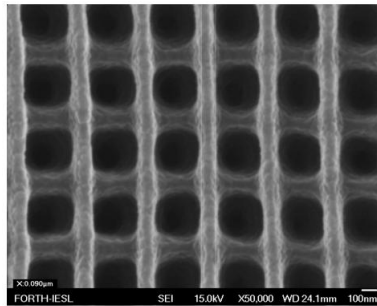


Figure 7.12: High resolution woodpile structure with feature width of $0.90\mu\text{m}$

Next, the last combination tried in order to push the limit down to woodpiles with rod spacing of 400nm and a unit cell height of 565nm is the one with mole ratio of $\frac{MAPTMS}{ZPO} = \frac{8}{2}$ and $\frac{MAPTMS+ZPO}{DMAEMA} = \frac{90}{10}$. Same structuring strategy as before, retaining low writing speed at $20\frac{\mu\text{m}}{\text{sec}}$ and low laser power close to the polymerization threshold, a series of woodpile were fabricated.

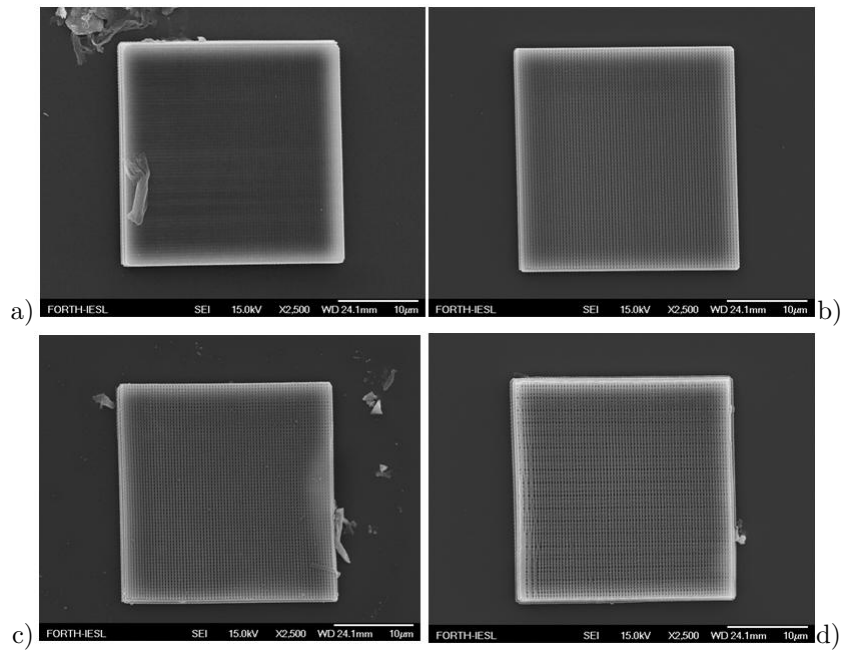


Figure 7.13: Woodpile structures with inlayer periodicity of 400nm for varying energies: a) 2.4mW , b) 2.3mW , c) 2.2mW , d) 2.1mW

As in the previous case, starting from a laser power of 2.4mW (upper left) decreasing with a step of 0.1mW we can see the different structural deforma-

tions due to shrinkage effects. As one moves down from higher energies to lower ones, structural characteristics become more pronounced. At the highest energy applied (2.4mW) the lines are nearly discriminated in the outer layer, the filling fraction is relatively high resulting in a rather 3D cube. Moving down just 0.1mW, lines start to appear and become relatively more pronounced as one decreases the energy to 2.2mW. Finally, at 2.1mW the structural deformation is more obvious, shrinkage starts to dominate since the filling fraction decreases. However, as we will see in the following section of the optical characterization, this structure was the only one to reveal a kind of diffraction pattern indicating the periodicity of the structure. All the rest, have simply given diffused scattering.

These two examples above have revealed the necessity for one to be very precise during the fabrication procedure. Near threshold fabrication is a task quite sensitive to laser power fluctuations given the fact that the two photon absorption rate depends quadratically on the light intensity. High resolution structures have, thus, been fabricated at low laser powers and long exposure times in accordance with the theoretical predictions.

7.3 Optical Characterization

The optical response of the fabricated structures was measured by means of angle resolved transmission spectroscopy using the set up described in a previous section. The samples were placed on top of a 3D translation stage and the diffraction patterns obtained were used to orientate the samples. Spectra are taken at normal incidence. Figure 7.14 shows the actual experimental setup:

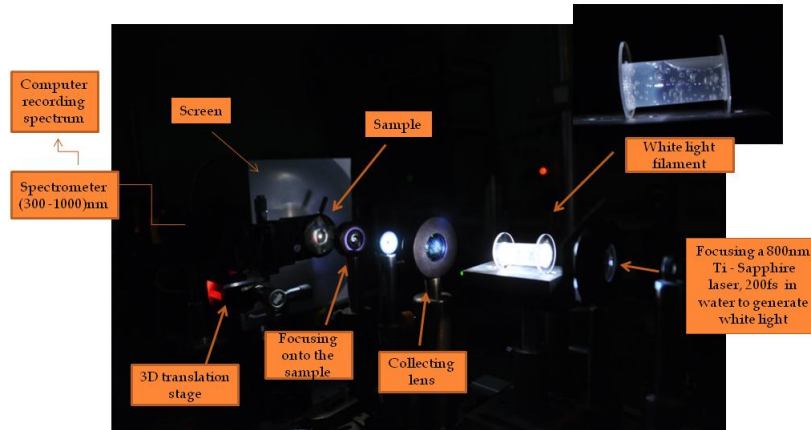


Figure 7.14: Optical characterization set-up

A Ti-Sapphire laser beam centered at a wavelength of 800nm with a pulse duration of 200fs is tightly focused onto a cell filled with distilled water producing a white light filament. The output is collected by a lens and imaged onto the sample, which is placed on top of a 3D translational stage. The light transmitted by the sample is spatially filtered in an intermediate image plane, which can also be inspected with a camera system (not shown) in order to collect light that has passed through the sample. The filtered light is imaged onto an optical fiber connected to a spectrometer, which gives access to the spectral range from 300nm to 1000nm. In order to observe diffraction patterns revealed from the periodic nanostructures, a screen is inserted right after the light has passed through the sample.

To ensure proper normalization, the measured transmission spectra are normalized to the transmission of the bare glass for the same angle of incidence requiring only a small lateral movement of the sample. This implies that the transmission defined in this manner can slightly exceed unity for wavelengths where the photonic crystal essentially acts as an antireflection coating for the glass substrate [10].

7.3.1 Theoretical calculations and FTIR measurements

Furthermore, for a direct comparison with the expectations for a perfect structure and to interpret the observed structures, two examples of measured

transmission spectra are performed using an FTIR spectrometer in combination with band - structure calculations. These are schematically shown in figure 7.15.

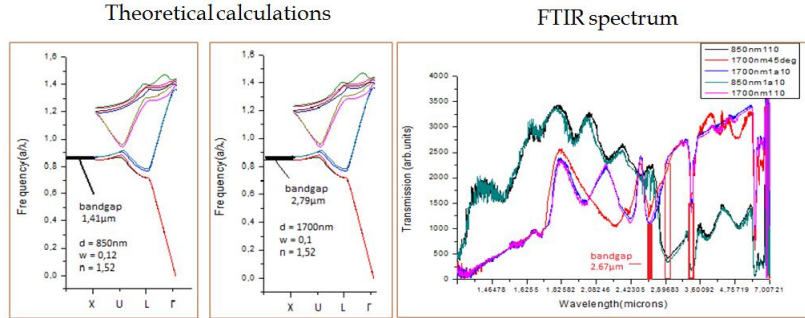


Figure 7.15: FTIR measurements and theoretical calculations for woodpile with inlayer periodicity of 1700nm and 850nm

Two kind of photonic structures are used: one with inlayer periodicity of 1700nm and another one with 850nm. As we can see on the left panel, theoretical calculations predict that the main bandgap for the case of $d = 850nm$ lies at $\frac{a}{\lambda} = 0.855 \Rightarrow \lambda = 1.41\mu m$, where a is the unit cell height and λ the vacuum wavelength. Whereas, for the case of $d = 1700nm$, the main bandgap is around $\frac{a}{\lambda} = 0.86 \Rightarrow \lambda = 2.79\mu m$. In relation to the FTIR measurements on the right panel, we have very good agreement between theoretical calculations and experimental results; for the latter case the bandgap measured corresponds to $2.67\mu m$, whereas for the former it is located just to the edge of the spectral range of the spectrometer around $1.35\mu m$. We can also clearly see the absorption bands at $3.4\mu m$ and $3.0\mu m$ due to the material itself [1].

7.3.2 Diffraction patterns

During the experimental process, woodpile structures with varying unit cell heights have been fabricated. Diffraction patterns recorded for the optical characterization reveal structural characteristics, as well as, high quality samples. A series of them is depicted in figure 7.16. As already stated in a previous section, the woodpile structure presents a square symmetry in the planes in between the layers that is actually revealed by the square symmetry of the diffraction pattern observed. Furthermore, diffraction channels open when $|g| < k$ and we have a diffraction cutoff whenever $|g| = k$. In particular, for a square lattice, this condition reduces to

$$\frac{c}{\lambda} = \frac{\sqrt{2}}{n} \sqrt{p^2 + q^2}$$

Thus, in air four diffraction channels open corresponding to

$$(p, q) = (1, 0), (0, 1), (-1, 0), (0, -1)$$

when $\frac{c}{\lambda} > \sqrt{2} \Rightarrow d > \lambda$.

In accordance to those mentioned above, the first four diffraction channels are observed for all the fabricated structures molding the characteristic cross round the forward transmitted beam. However, the difference lies at the colors observed. As one goes from $d = 1700nm$ to $d = 700nm$, the whole visible spectrum is diffracted since the condition $d > \lambda$ holds. The diffraction cutoff starts to become more pronounced as one moves to unit cells close to the visible spectral range, such as for $d = 600nm$ and $d = 500nm$, where one can clearly observe the cut off for the “red part” of the visible. The same situation holds as one moves from $d = 500nm$ to $d = 400nm$, where a cutoff exists for the “red” and the “green part” of the visible spectrum.

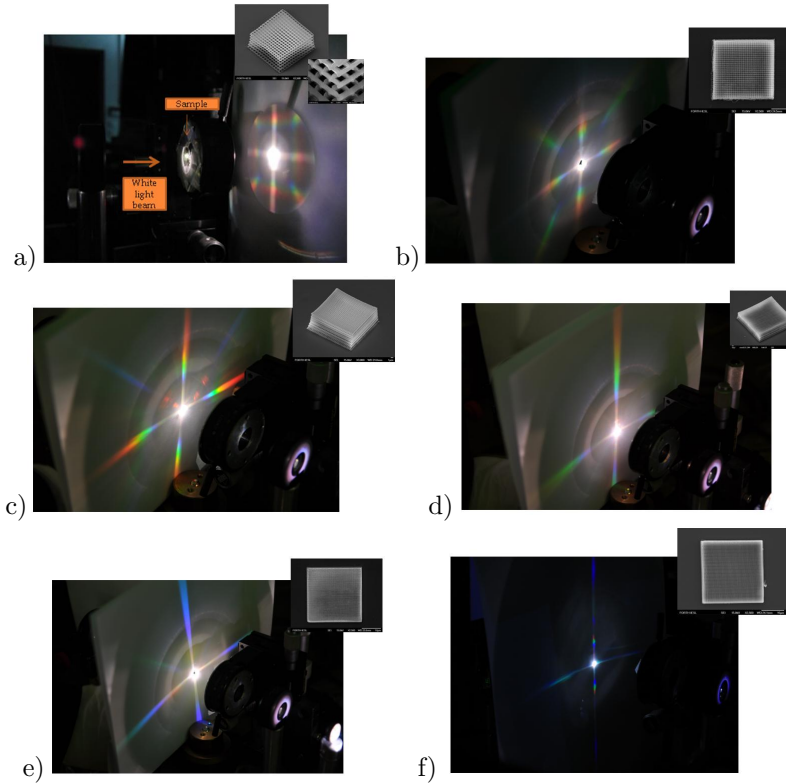


Figure 7.16: Diffraction patterns from woodpile crystals with various inlayer periodicity: a)1700nm, b)900nm, c)700nm, d)600nm, e)500nm, f)400nm

Next, the second set of diffraction spots appears for

$$(p, q) = (1, 1), (1, -1), (-1, 1), (-1, -1)$$

when $\frac{c}{\lambda} > 2 \Rightarrow d > \sqrt{2}\lambda$. In addition to the four spots molding the cross, another set appears along the diagonal direction. Still, these channels are observed as on goes from $d = 1700nm$ to $d = 700nm$. For the case of $d = 1700nm$, $\lambda < \frac{1700nm}{\sqrt{2}} = 1200nm$ the whole visible spectrum is diffracted. In the case of $d = 900nm \Rightarrow \lambda < \frac{900nm}{\sqrt{2}} = 636nm$ the “red part” is nearly diffracted, whereas for $d = 700nm \Rightarrow \lambda < \frac{700nm}{\sqrt{2}} = 495nm$ the “red part” is cutoff and the green part is just diffracted. However, for $d = 600nm \Rightarrow \lambda < \frac{600nm}{\sqrt{2}} = 424nm$ and $d = 500nm \Rightarrow \lambda < \frac{500nm}{\sqrt{2}} = 353nm$ the visible wavelengths are limited, thus no diagonal spots are observed. It is worth noticing that for the case of the woodpile structure with $d = 400nm$,

the characteristic cross is not clearly seen. Though, the sharpness of the diffraction spots indicates the long-range order inherent to periodic photonic crystals due to their translational symmetry. In particular, instead of the four diffraction channels along two orthogonal directions, only two are observed along a single direction. This is in accordance to the SEM image taken, where structural deformation due to shrinkage is evident. This is further supported by the optical response measured. Theoretical calculations made using the MPB software for $w = 0.176c$, $n = 1.52$, $h = 0.5c$ are shown schematically in figure 7.17a. The bandgap is located for a normalized frequency of $\frac{c}{\lambda} \sim 0.8$, that is for a vacuum wavelength of $\sim 710\text{nm}$, which is about 100nm blueshifted in relation to the transmittance dip measured experimentally (figure 7.17b). It is worth mentioning that the diffraction cutoff is located at $\frac{c}{\lambda} = 1.414 \Rightarrow d = 400\text{nm}$, thus the other two set of spots may correspond to a higher order partial bandgap located at $\frac{c}{\lambda} \sim 0.966$ and higher.

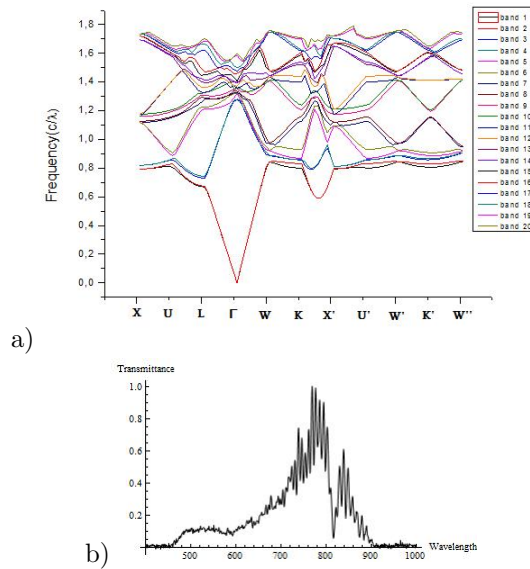


Figure 7.17: Measured and calculated data for a woodpile with inlayer periodicity of 400nm

8 Chapter 8: NonLinear Photonic crystals of CdS - Zirconium-Dmaema polymer composites

The design of a stimulus-responsive material for dynamic tuning of photonic properties is presented. We demonstrate woodpile photonic crystals of CdS-Zirconium-Dmaema polymer composites fabricated by the combination of the two - photon polymerization technique and in situ synthesis of CdS nanoparticles inside the 3D photonic matrix. The nonlinear properties of the composite material were measured by means of the z-scan method. Angle resolved transmission spectroscopy was employed for the optical characterization of the fabricated structures, whereas the dynamic tuning of the system's response was recorded through a pump and probe experiment.

8.1 CdS -Zirconium-Dmaema composite

In general, using semiconductor nanomaterials is useful for improving the optical properties of polymeric materials due to the unique properties of nanomaterials. However, the methods used for the synthesis, characterization and properties of inorganic/semiconductor nanocomposites are not suited to the requirements of microstructure fabrication by two photon polymerization, since the materials should be easily photopolymerizable, as well as, transparent at the wavelength of the laser used in fabrication. It is difficult to keep photopolymerizable materials transparent by simply dispersing semiconductor/inorganic nanoparticles in the materials. Thus, the in situ synthesis of nanoparticles in a polymer matrix is a useful method for resolving this issue, since it can be applied to 3D microstructures after two - photon fabrication [65].

Recently, it has been demonstrated by [64] who give a strategy for controlling the size of in situ synthesized CdS NPs within polymer matrices by tuning the crosslinking density of polymers that are obtained by photopolymerization. The size of the in situ synthesized CdS NPs within the polymer matrix is confined by the space available within the crosslinking polymer network. The designed photopolymerizable resins are composed of precursors of CdS NPs, monomers, and oligomers, along with the photoinitiator and the photosensitizer. They have used cadmium methacrylates ($\text{Cd}(\text{MA})_2$) as precursors for

CdS NPs; these species also serve as monomers for photopolymerization. A commercially available oligomer, dipentaerythritol hexaacrylate (DEP-6A), has been selected as the crosslinker. Methacrylic acid (MA) and methyl methacrylate (MMA) have been used as monomers.

In our case, by using a sol gel process we have developed a novel material consisting of a photosensitive zirconium - dmaema hybrid polymer functionalized with CdS quantum dots to achieve a large third order nonlinearity. The material is synthesized following the procedure mentioned above. In particular, cadmium methacrylates used as precursors for CdS nanoparticles were combined with the zirconium - dmaema composite described in the previous chapter to form the inorganic network for high resolution fabrication; both methacrylates units also serve as monomers for photopolymerization. In situ synthesis of CdS in the photonic crystals has taken place via Na_2S treatment. Woodpile structure with inlayer periodicity of 500nm are successfully fabricated.

8.1.1 Synthesis of CdS-Polymer Nanocomposites

$Cd(MA)_2$ was prepared by the following procedure: CdO powder was added in portions to a round bottom flask containing MAA and ethanol (10 mL) at room temperature. Subsequently, the mixture was stirred for 30 h. After removing ethanol, MAA, and H_2O in vacuum, the desired product was obtained. Since each Cd has two bonding sites for each methacrylic acid, the mole ratio is: $n_{CdO} = 2n_{MAA}$ (figure 8.1). Depending on the final quantity we want to fabricate, we choose the appropriate amount of CdO and MAA. Suppose, for example, that we want to use $n_{CdO} = 10mmol = 10 \times 10^{-3}mol$, then $n_{MAA} = 2 \times 10mmol = 20mmole = 20 \times 10^{-3}mol$.

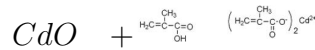


Figure 8.1: Cadmium methacrylate

$$n_{CdO} = \frac{m_{CdO}}{MB_{CdO}} \Rightarrow m_{CdO} = n_{CdO} MB_{CdO} = 10 \times 10^{-3}mol \times 128.4 \frac{gr}{mole} = 1.284gr$$

$$n_{MAA} = \frac{m_{MAA}}{MB_{MAA}} \Rightarrow m_{MAA} = n_{MAA} MB_{MAA} = 20 \times 10^{-3}mole \times 86.6 \frac{gr}{mole} = 1.7212gr$$

$$d_{MAA} = \frac{m_{MAA}}{V_{MAA}} \Rightarrow V_{MAA} = \frac{m_{MAA}}{d_{MAA}} = \frac{1.7212gr}{1.015 \frac{gr}{ml}} = 1.7ml$$

The amount of ethanol added is: $V_{ETH} = \frac{10mmole \times 10ml}{98.1mmol} = 1ml$

The photopolymerizable resins were prepared by mixing $Cd(MA)_2$ in Methacrylic Acid and ZPO according to the mole ratio chosen as in previous section. In particular, the inorganic/organic combination of $\frac{MAPTMS}{ZPO} = \frac{8}{2}$, $\frac{MAA}{ZPO} = \frac{1}{1}$ and $\frac{ZPO}{DMAEMA} = \frac{90}{10}$ was chosen, as it has given the best structural results. Films were prepared by spin-coating the resins onto a glass substrate, and subsequently polymerized under the irradiation of a high-voltage mercury lamp for an hour. The films were then treated with Na_2S in solution for 4h to form pale yellow nanocomposites. CdS nanoparticles are synthesized in a polymer matrix photopolymerized via the reaction between the cadmium ions in the polymer and nitrogen sulfide (Na_2S). The polymer film containing cadmium ions is clearly colorless and transparent before the treatment with Na_2S . After a 4h of the treatment with Na_2S , a broad absorption band from the exciton CdS nanoparticle appears and demonstrates as a pale yellow nanocomposite. The main emission band of CdS nanoparticle - polymer nanocomposites is clearly attributed to the band edge emission of CdS nanoparticle (figure 8.2).

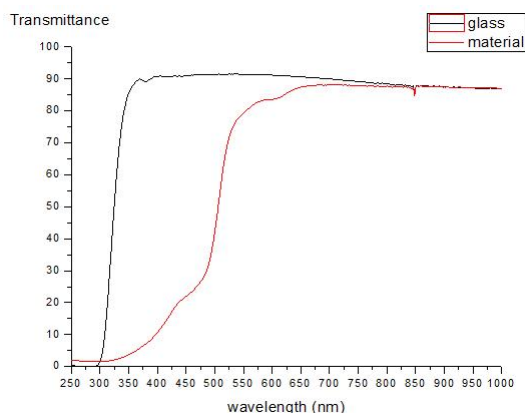


Figure 8.2: Absorption band at 480nm attributed to the exciton CdS nanoparticle

Quantum dots are made out of semiconductor materials. Thus, the electrons in quantum dots have a range of energies and the concepts of energy levels, bandgap, conduction band and valence band still apply. However, there is a major difference. Excitons formed from the pair of a raised electron and the hole, have an average physical separation between the electron and hole;

referred to as the Exciton Bohr Radius, this distance is different for each material. In bulk, the dimensions of the semiconductor crystal are much larger than the exciton bohr radius, allowing the exciton to extend to its natural limit. However, if the size of a semiconductor crystal becomes small enough that it approaches the size of the materials Exciton Bohr Radius, then the electron energy levels can no longer be treated as continuous - they must be treated as discrete, meaning that there is a small and finite separation between energy levels. This situation of discrete energy levels is called quantum confinement, and under these conditions, the semiconductor material ceases to resemble the bulk, and instead can be called a quantum dot. This has large repercussions on the absorptive and emissive behavior of the semiconductor material.

Because the quantum dot's electron energy levels are discrete rather than continuous, the addition or subtraction of just a few atoms to the quantum dot has the effect of altering the boundaries of the bandgap. Changing the geometry of the surface of the quantum dot also changes the bandgap energy, owing again to the small size of the dot, and the effects, of quantum confinement. The bandgap in a quantum dot will always be energetically larger; therefore, we refer to the radiation from quantum dots to be "blue shifted" reflecting the fact that electrons must fall a greater distance in terms of energy and thus produce radiation of a shorter, and therefore "bluer" wavelength. In relation to the bulk semiconductor material, electrons tend to make transitions near the edges of the bandgap. However, with quantum dots, the size of the bandgap is controlled simply by adjusting the size of the dot. Because the emission frequency of a dot is dependent on the bandgap, it is therefore possible to control the output wavelength of a dot with extreme precision. In effect, it is possible to tune the bandgap of a dot, and therefore specify its "color" output. Unfortunately, in our case, in situ synthesis of CdS nanoparticles inside the 3D photonic matrix does not allow us to control the size of the CdS NPs, thus, introducing an ambiguity in their band edge emission.

8.2 Linear Characterization

8.2.1 Angle resolved transmittance measurements

Using this novel Cd(MA)₂- zirconium - dmaema material, woodpile structures with inlayer periodicity of 500nm were fabricated. Subsequently, in

situ synthesis of CdS nanoparticles in the polymer matrix has taken place via Na_2S treatment. For the optical characterization, we have used the standard setup already described. Theoretical calculations using the MPB software were carried out for a direct comparison with theory. The calculated band diagram for a woodpile structure having a contrast in the refractive index of $n = 1.52$, is shown in figure 8.3. The width and the height of the rods are $w = 0.165c$ and $h = 0.495c$, respectively, where c is the unit cell height.

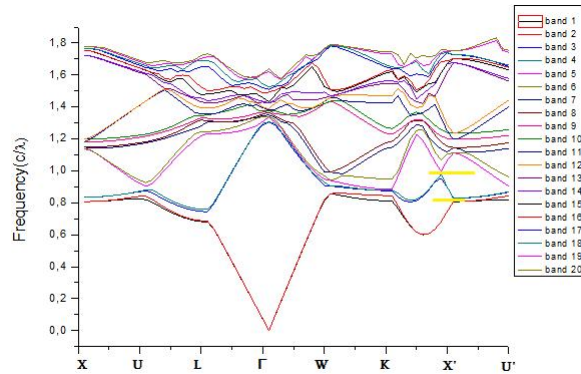


Figure 8.3: Band structure of a woodpile with inlayer periodicity of 500nm

The optical response recorded under white light continuum illumination is shown in figure 8.4. Transmittance measurements were carried out several times to ensure repeatable measurements.

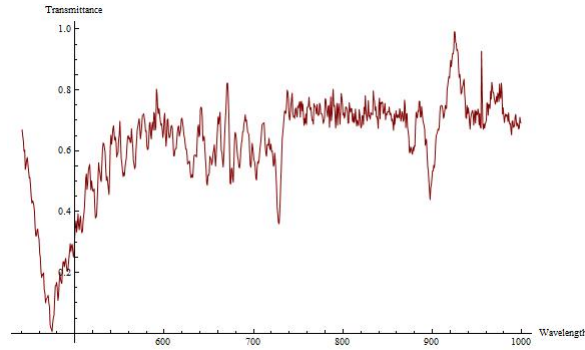


Figure 8.4: Transmittance measurements

From the optical response recorded, one can clearly see two sharp transmittance dips. The first one is located at 880nm and the second one at 730nm.

One can also clearly see the diffraction cutoff below 500nm [11]. As expected, due to the low contrast in refractive index these woodpile crystals do not possess a complete PBG, however, a partial band gap exists in the Γ -X direction. Thus, the first order band gap marked in a yellow bulk line is located at a normalized frequency of $\frac{c}{\lambda} = 0.8707$, that is for a vacuum wavelength of 876nm very close to the one observed at 880nm. Furthermore, this partial gap is extended to the normalized frequency of $\frac{c}{\lambda} = 0.83 \Rightarrow \lambda = 852\text{nm}$, about 25nm broad also observed in our measurements. In addition, the second order bandgap is located at a normalized frequency of $\frac{c}{\lambda} = 0.978$, that is for a vacuum wavelength of 722nm extended to $\frac{c}{\lambda} = 0.996 \Rightarrow \lambda = 710\text{nm}$, about 12nm broad. Both peaks identified, are in accordance to those expected by the theoretical calculations showing only small deviations from the theoretical values related to the position or the size of the gap. The accurate estimation of the filling fraction or the refractive index contrast represent the two major factors giving rise to these deviations.

8.3 Nonlinear characterization

For the determination of the nonlinear refractive index of our CdS - zirconium - dmaema material, the z-scan method will be employed. Initially, for the validation of our system, z-scan measurements was performed upon standard materials widely studied in the literature. In the following, the novel nonlinear material with CdS quantum dot - zirconium - dmaema composites, was characterized.

8.3.1 Nonlinear material characterization: Z-scan method

In general, in a pure transparent solvent, thermal, electrostriction, molecular reorientation, and electronic polarization are responsible for the optical Kerr effect. The change of refractive index is the sum of those effects. The reorientation contribution is essentially caused by the presence of the dipole moment and the asymmetric shape of the molecule. As we know, a dipole undergoes a torque under an electric field if it is not parallel to the field that is causing the molecular dipole moment to align along the external electrical field. Under laser illumination, the molecules will respond to the field and tend to align along the polarization direction instead of being randomly aligned. The typical response time for molecule reorientation is about 10^{-12}s , though, the final contribution from molecular re-orientation depends on the

duration of the laser pulse; the longer the pulse, the bigger the response is. The thermal contribution is mainly determined by the energy of each laser pulse and the size of the focus region. The temperature increase at the focal point is also determined by the heat capacity and dissipation rate. The electronic polarization contribution to n_2 is usually the smallest and the fastest. It is small because it is the third order correction to the linear susceptibility. Compared to the mass of the molecule, the mass of the electron is very small. The distortion of the electronic cloud can happen in 10^{-15} s or even faster. Because the optical pulse has an oscillation period ranging from 1 fs to a few fs, the nonlinear response from electronic polarization is always treated as an instantaneous effect that follows the temporal shape of the laser pulse. Therefore, in order to minimize other contributions while measuring the electronic contribution of n_2 , a short laser pulse that has high instantaneous power but low average power is needed. In our experiment, the pulse duration of the laser was of the order of 200 fs.

Experimental layout

The experimental layout used for the Z-scan measurements is schemenatically depicted in figure 8.1. The laser source employed for this experiment is a Ti-Sapphire centered at 800nm wavelength with 200fs pulse duration, which gives 1mJ pulses with a 1KHz repetition rate. The laser beam is focused along the Z-axis by a lens with focal length, $f = 10cm$ and the signal transmitted is recorded on a oscilloscope through a photodiode. An iris placed in front of the detector serves as the aperture. The sample sits on a linear translation stage and moves along the z-path using a Labview control program.

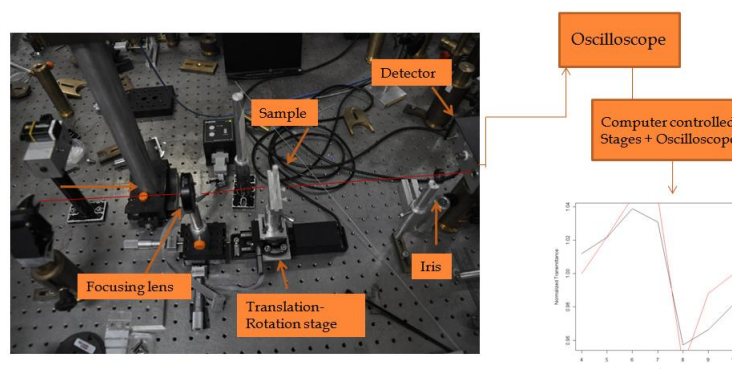


Figure 8.5: Z-scan experimental set-up

The ultra-fast pulse has two advantages in the n_2 measurement: a) high instantaneous power that allowed us to measure small n_2 , b) low pulse energy and short pulse duration that allowed us to rule out the thermal and molecule reorientation effects. Therefore, in our experiment, the electronic polarization is the major contribution to n_2 .

Beam Characterization

To ensure a Gaussian beam profile for our system, the beam cross section is measured through the intensity distribution in the x-y plane along the z-path. A CCD camera is placed on top of the sample holder in order to capture the intensity distribution while translating along the focus. Next, for every single picture taken the intensity distribution is fitted to the Gaussian model through a Labview written program in order to obtain the FWHM value at each single position. Then, the variation of the FWHM value fitted at each position is in turn fitted to the Gaussian model in order to get the FWHM along the z-path. Finally, the pixels of our CCD camera are converted to the specified real dimensions.

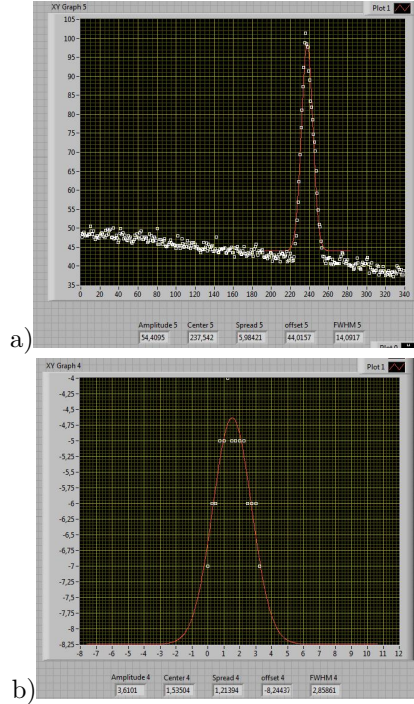


Figure 8.6: a) Gaussian intensity distribution at the x-y plane for a specific z-position
b) Gaussian fit of the FWHM along the z-path

The intensity distribution at the x-y plane along the z-path is captured for 14 subsequent positions, each of them is fitted to the Gaussian model as shown schematically in figure 8.6a. Then, these 14 different values obtained for the FWHM at each single position are fitted in turn to the Gaussian model and we get the value of $FWHM = 2.85861$. The specifications of our camera are such that each pixel corresponds to $5.6\mu m$. So that the FWHM for our laser beam is estimated to be $FWHM = 2.85861 \times 5.6\mu m \simeq 16\mu m$. To compare with theory, we know that from Gaussian beam optics the beam radius at focus w_0 is given by:

$$2w_0 = \frac{4\lambda}{\pi} \left(\frac{f}{D} \right)$$

where f the focal length of the lens, D the beam diameter and λ the laser wavelength. Thus, in our case, we get that:

$$2w_0 = \frac{4}{\pi} 800nm \frac{100mm}{6mm} \simeq 17\mu m$$

which is very close to the experimental value estimated. In accordance, the diffraction length z_0 is given by:

$$z_0 = \frac{kw_0^2}{2} = \frac{\pi}{\lambda} \left(\frac{17\mu m}{2} \right)^2 \simeq 283\mu m$$

8.3.2 Z-scan measurements

The materials characterized during the experimental procedure were Toluene, Chlorobenzene and the CdS - zirconium - dmeama hybrid. The former two are standard solvents used for the validation of our system. The solvents were measured in a 1-mm-thick quartz cuvette, whereas the nanocomposite thin films were prepared from the CdS - zirconium - material. The z-scan traces obtained are shown below:

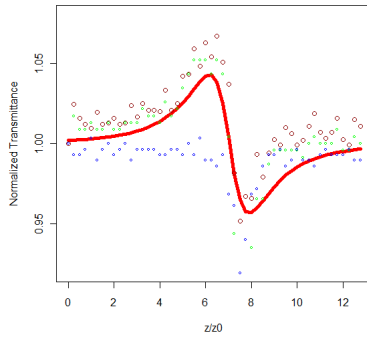


Figure 8.7: Z-scan curve for Toluene

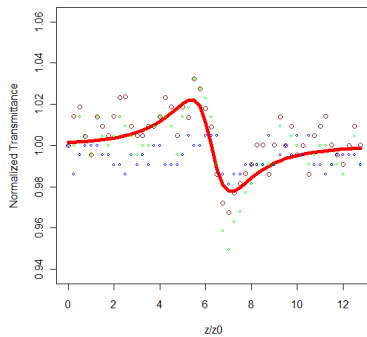


Figure 8.8: Z-scan curve for Chlorobenzene

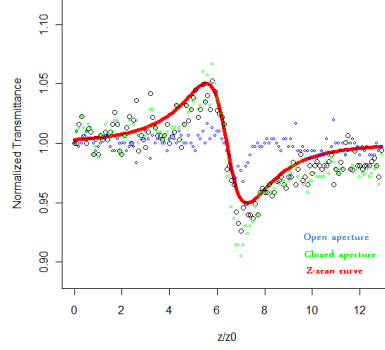


Figure 8.9: Z-scan curve for CdS-zirconium-dmaema

The measured close aperture z-scan trace is presented by a green dotted line, whereas the open aperture trace is marked with a blue dotted line. The net effect traced by the bigger red circles is fitted to equation (4.36) from where we can extract the nonlinear phase shift and the ratio $\frac{\Delta\Phi_0}{z_0}$. In addition, considering the following relations:

$$\text{linear absorption } \alpha = \frac{1}{L} \ln \left(\frac{I}{I_0} \right),$$

$$\text{effective length } L_{eff} = \frac{(1 - e^{-\alpha L})}{\alpha},$$

the peak irradiance at focus $I_0 = \frac{2E}{\pi w_0^2 \tau}$, where τ = pulse duration, E = pulse energy

$$\text{the nonlinear refractive index } n_2 = \left(\frac{\lambda}{2\pi} \right) \frac{\Delta\Phi_0}{I_0 L_{eff}}$$

we can construct the following table:

	$\Delta\Phi_0$	α (cm^{-1})	I_0 ($10^{12} \frac{W}{cm^2}$)	L_{eff} (cm^{-1})	n_2 ($10^{-15} \frac{cm^2}{W}$)
Toluene	0.213	-0.392	0.0771	0.098	0.354, 1.83[7]
Chlorobenzene	0.1102	-0.763	0.0896	0.096	0.161
QD	0.2488	-230	0.1891	0.00089	185.7

As we can see from figure 8.9, for the nanocomposites, a clear third order nonlinearity can be observed as indicated by the peak - valey z - scan trace. In particular, a positive nonlinearity is attributed to it, since the peak - then - valey sequence was recorded as the sample translated towards the focusing lens. It should be mentioned that the open-aperture Z-scan trace at the same excitation intensity revealed negligible two - photon absorption and confirms that the observed third order nonlinearity is a result of non-linear refraction. It is worth noticing also that the magnitude of n_2 measured for our nanocomposites is three orders larger than those obtained for the standard solvents. Such large nonlinearities have been previously reported in analogous experiments involving QDs doped nanocomposites [26],[36].

8.3.3 Pump and Probe technique

The pump-probe experiment has been widely used to determine the dynamics of a system. In a pump-probe experiment, a beam of pump light (photon) excites the material into an intermediate state first; next, a beam of probe light is directed onto the same spot in order to detect the change induced by the pump light. In our experiment, we employed the pump-probe technique to measure the optical switching effect in a 3D photonic crystal. The experimental setup is shown in figure 8.10.

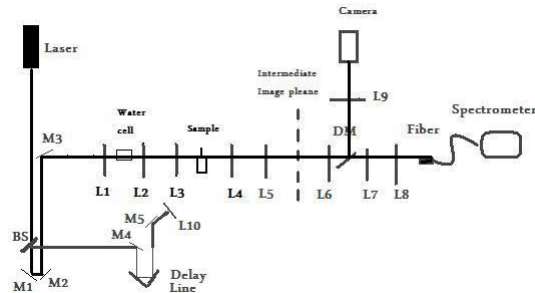


Figure 8.10: Pump-Probe setup

The setup is similar to the one used for the probe experiment. In this case, the Ti-sapphire laser beam centered at 800nm used to generate the white continuum is halved at the exit of the amplifier. Thus, one part of it is used as the pump beam for the experiment and the other half as the white light probe. A beam splitter (BS) is used to split the beam into two arms. The probe beam is directed through the mirrors M1, M2 from its initial path,

whereas the pump beam through mirrors M4, M5 is directed and focused by lens L10 ($f = 20cm$) onto the sample. Lenses L3 and L10 ensure the spatial overlapping of the pump and probe beam at focus, whereas, a delay line between mirrors M4, M5 serves for their temporal overlap. The latter is checked by observing the sum frequency generation (second harmonic generation) in a BBO crystal. The focal length of the L10 lens is chosen to be higher than that of the probe thus, the size of pump beam spot on the sample was much larger than that of the probe beam for better spatial overlap at focus.

Therefore, when carrying out the experiment, initially the time zero for the pump and probe beam is defined by using the BBO crystal. In sequence, the sample is placed on top of the holder. Then, under white light continuum illumination, the diffraction pattern observed ensures that the sample is well orientated and positioned near focus. The optical response of the sample is recorded while the pump beam is delayed in time. This is achieved by spatially moving the delay line before and after the time - zero position. The results recorded are shown in the following figures. Each time step corresponds to $500\mu m$ (x2 for the two branches of the delay line) translation, that is about 3.33ps time - delay. Transmittance measurements were carried out several times to ensure repeatable measurements. Two sets of measurements are shown in figures 8.11 and 8.13.

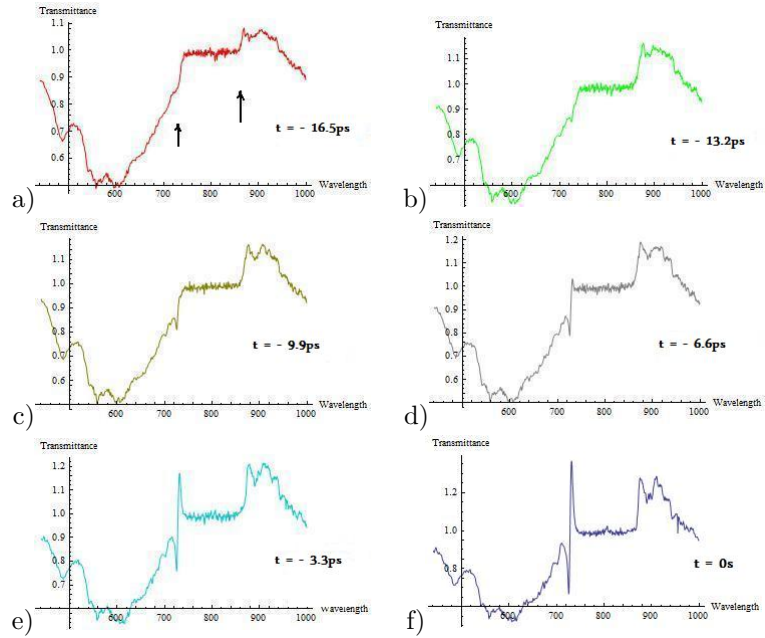


Figure 8.11: Pump-probe transmittance measurements in several time delays (set1)

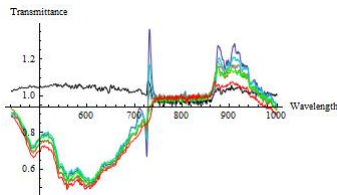


Figure 8.12: Pump - probe transmittance measurements (set1)

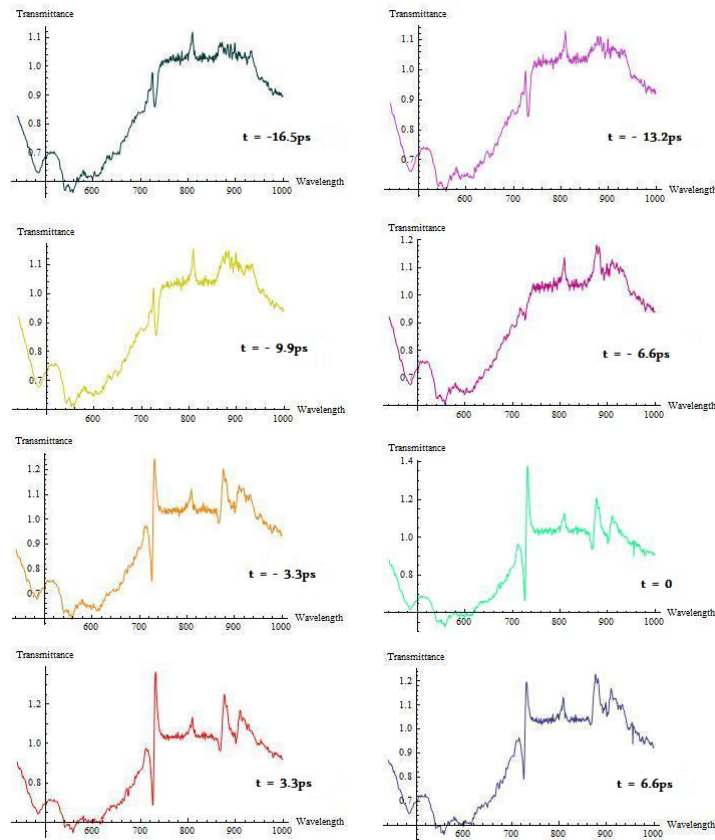


Figure 8.13: Pump and probe (set2)

As we can see in both figures 8.11, 8.13 the pump beam causes an enhancement of the optical response of the sample located at the positions where the two transmittance dips were observed during the probe experiment. The dips are clearly sharper and deeper in relation to the linear measurements. As predicted by theory, close to the band gap the group velocity of light decreases, leading to a high density of states and field localization. This local-field enhancement occurs at both the high and low-energy edges of the band gap. In figure 8.12 and 8.13a all the data recorded are plotted simultaneously for a better comparison. The black line in figure 8.12 corresponds to the background noise recorded with the bare glass only.

In particular, figure 8.14b depicts a sequential measurement of the optical response in two different time delays in relation to the $t = 0$ position. As

the time delay reduces from 9.9ps to 6.6ps, a “blue” shift of the second dip position is observed. Figure 8.14c shows a graphical representation of that shift at each time position. Away from time zero (-16.5ps), the dip is located at 730nm. As the time delay decreases from -9.9ps to -6.6ps, a pronounced shift from 730nm to 726nm is observed accompanied by a sharp transmittance decrease. The transmitted intensity decreases further as the time approaches to the $t = 0$ position, whereas the dip position remains the same. Finally, the time delay starts to increase again as the delay line passes through the $t = 0$ position, the dip position further shifts to 725nm, whereas the intensity of the dip decreases in turn.

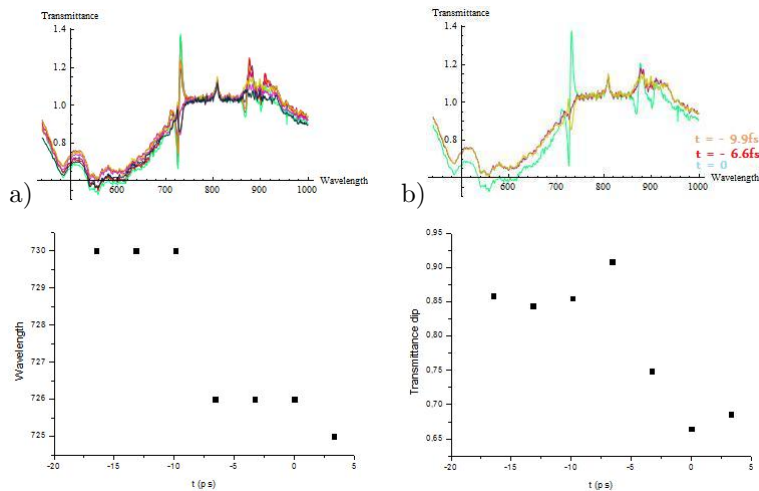


Figure 8.14: Pump-probe: a) all measurements (set 2), b) sequential time steps, c) wavelength shift and d) intensity change of the dip located at 730nm

As expected, due to the optical kerr effect, the pump beam induces a change in refractive index analogous to the intensity, i.e $\Delta n = n_2 I$. The intensity of the pump beam at focus is approximately $I_0 = 1.244 \times 10^{13} \frac{W}{cm^2}$. Though, this value is reduced by a factor of 4 due if one wished to calculate the related intensity at focus for the z - scan experiment. That is because different focusing lenses were used in the z - scan and pump - probe experiment. Thus, the change in refractive index induced is about $\Delta n = 5.77$. This value implies a huge change in refractive index, though the origin of this change is not only attributed to the electronic polarization. In such high intensities, other nonlinear and thermal effects may come into play as well, thus it is difficult to extract any “safe” conclusion about the induced change

theoretically expected. The “blue” shift in the dip position implies a positive change in refractive index in accordance to the experimental results, though we can not extract any analogous conclusion for the transmittance dip located at 880nm as it lies very close to the edge of the 800nm filter cut off.

9 Conclusions

Throughout this thesis, we have concentrated on the fabrication of high resolution 3D linear and nonlinear photonic crystals in order to investigate their optical properties. In particular, the systems under study were woodpile based photonic structures fabricated by applying the technique of direct laser writing. The design of novel linear and nonlinear materials suitable for two-photon fabrication and with proper optical and mechanical properties, such as high refractive index, high transmission at the wavelength of interest, wide tunability and high thermal and mechanical stability has enabled the fabrication of precise 3D structures with a response in the visible spectral range.

Several techniques were employed for this purpose. As mentioned previously, two-photon polymerization was the technique utilized for the fabrication of our photonic structures, while the sol-gel technique has provided a versatile tool for the control of materials chemistry. Refractive index tuning by varying the molar ratio of inorganic-organic components, as well as, the incorporation of active molecules was achieved. White-light Bragg diffraction experiments in combination with scanning electron microscopy were employed in order to characterize the quality of the fabricated structures. Both methods have demonstrated high sample quality. The prism-film coupler technique was applied for the linear refractive index measurements, while the z-scan method was employed for the study of the nonlinear refractive index. Furthermore, angle resolved transmittance spectroscopy was applied in order to investigate the optical properties of the fabricated structures, while pump-probe experiments were carried out in order to record the dynamic tuning of their optical response. Appropriate theoretical calculations were applied to evaluate the experimental findings.

In the first part of this study, we have synthesized and characterized a novel, titanium-containing hybrid material that can be structured three-dimensionally using two-photon polymerization. The co-polymerization of a silicon alkoxide with another metal alkoxide has been shown to enhance the material's mechanical stability and allow the modification of its refractive index. Strong complexing ligands such as methacrylic acid are often used to control the relative hydrolysis and condensation reaction rates of non-silicate

metal alkoxide precursors. Titanium alkoxide was chosen because of the interest in making high refractive index material via TiO_2 , while titanium composites possess high optical transparency in the visible and near-infrared part of the spectrum. Furthermore, titanium alkoxide can readily undergo hydrolysis and condensation to generate titania. In the presence of silane - based compounds, it can also form a covalent bond with silicon alkoxide, which serves as to localize the particles formed resulting in a metal - polymer composite dispersed at the molecular level. In this sense, the effect on the structurability of the increase of titanium isopropoxide and methacrylic acid in this photosensitive composite is investigated. We show that while it is possible to make transparent thin films with a titanium isopropoxide molar content as high as 90%, three-dimensional structures can be made only when the titanium isopropoxide molar content is less than 50%. We measure the refractive index of films with different titanium isopropoxide : methacrylic acid concentrations and we show that while the refractive index increases linearly with the titanium iso-propoxide, the increase of the methacrylic acid content does not affect the refractive index of the material.

Recently, zirconium/silicon composites have been widely used for structuring by two photon polymerization . It has been demonstrated that these materials are suitable for two photon polymerization fabrication, since they exhibit the characteristic of minimal shrinkage during photopolymerization. No additional efforts such as precompensation or mechanical stabilization to avoid structural distortions are, thus, necessary. In addition, by varying the material's inorganic content, it is possible to modify and tune its refractive index. On the other hand, amines are known as physical quenchers of singlet oxygen and radical quenching is the major factor for sub-diffraction limit fabrication. Radicals generated during the photopolymerization process combine with oxygen molecules producing much less active radicals, thus photo-polymerization reactions are prohibited. Based on these mechanisms, high resolution 3D woodpile structures with an inlayer periodicity of 400nm and an optical response in the visible range of frequencies were fabricated by synthesizing a novel hybrid material containing zirconium - dmaema composites. In addition, a new method for high resolution micro-structuring was presented, which involves multiple exposures. Fabrication of micro-structures below the polymerization threshold were tuned depending on the number of exposure times. White - light Bragg diffraction and angle

resolved transmittance measurements were carried out to study their optical properties. Bragg diffraction patterns display the reciprocal space or Fourier transform of the photonic crystal for a specific spatial direction. Since Bragg diffraction is the relevant mechanism for the formation of the band structure, the diffraction pattern obtained is related to the band structure as a cut at a specific frequency (and for a specific spatial direction) and, thus, is in principle dependent on the wavelength of the light, the photonic crystal was probed with. In photonic crystals, light is diffracted strongly and leads to sharp Bragg diffraction peaks, if the difference of the wave vectors of the incident and diffracted light, respectively, corresponds to a reciprocal lattice vector, i.e., $|\Delta\vec{k}| = |\vec{k}_{inc} - \vec{k}_{diffr}| = \vec{G}$. The sharpness of the diffraction spots observed has indicated the long-range order inherent in periodic photonic crystals due to their translational symmetry.

The design of a stimulus-responsive material for dynamic tuning of photonic properties is a major research issue due to potential applications in ultrahigh-speed information processing. The refractive index contrast of photonic crystals made from Kerr nonlinear materials can change under optical pumping with high intensity light. The subsequent rapid shift in band gap can be exploited as optical switching. In our case, by using a sol gel process we have developed a novel material consisting of a photosensitive zirconium - dmaema hybrid polymer functionalized with CdS quantum dots to achieve a large third order nonlinearity. In particular, cadmium methacrylates used as precursors for CdS nanoparticles were combined with the zirconium - dmaema composite described previously to form the inorganic network for high resolution fabrication; both methacrylates units have also served as monomers for photopolymerization. However, the methods used for the synthesis, characterization and properties of inorganic/semiconductor nanocomposites are not suited to the requirements of microstructure fabrication by two photon polymerization, since the materials should be easily photopolymerizable, as well as, transparent at the wavelength of the laser used in fabrication. Thus, the in situ synthesis of nanoparticles in a polymer matrix was utilized for resolving this issue, as it can be applied to 3D microstructures after two-photon fabrication. In our case, in situ synthesis of CdS in the photonic crystals has taken place via Na_2S treatment. The Z-scan measurements revealed that the third-order non-linearity of the uniformly dispersed CdS nanocomposite is $1.8 \times 10^{-12} \frac{cm^2}{W}$ after polymerization. Woodpile structures

with inlayer periodicity of 500nm were successfully fabricated via two photon polymerization. Angle resolved transmittance spectroscopy has enabled the experimental observation of the first and second order partial band gap, while the pump - probe experiment recorded the dynamic tuning of the system's response with a "blue" shift of 6nm of the second order dip.

Part III

Appendices

Appendix A

MPB code for the woodpile structure:

```
(set! geometry-lattice (make lattice
  (basis-size (sqrt 0.5) (sqrt 0.5) (sqrt 0.5))
  (basis1 0 1 1)
  (basis2 1 0 1)
  (basis3 1 1 0)))
(define-param k-interp 9)
; Corners of the irreducible Brillouin zone for the fcc lattice,
; in a canonical order. In this case, woodpile breaks some of
; the symmetry so we have additional points W'', X', etc.
(define X (vector3 0 0.5 0.5))
(define U (vector3 0.25 0.625 0.625))
(define L (vector3 0.5 0.5 0.5))
(define Gamma (vector3 0 0 0))
(define W (vector3 0.25 0.5 0.75))
(define K (vector3 0.375 0.375 0.75))
; inequivalent points due to broken symmetry
(define W'' (rotate-reciprocal-vector3 X (deg->rad 90) W))
(define X' (vector3 0.5 0.5 0)) ; z (stacking) direction
(define K' (rotate-reciprocal-vector3 L (deg->rad -120) K))
(define W' (rotate-reciprocal-vector3 L (deg->rad -120) W))
(define U' (rotate-reciprocal-vector3 L (deg->rad -120) U))
(set! k-points (interpolate k-interp (list X U L Gamma W K X' U' W'
K' W'')))
(define-param eps 13); the dielectric constant of the "log" material
(define diel (make dielectric (epsilon eps)))
(define-param w 0.2) ; width of the logs
(define-param h 0.25) ; height of logs (should be 1/4 for fcc to not overlap)
; shortcut for cartesian->lattice function:
(define (c->l . args) (cartesian->lattice (apply vector3 args)))
(set! geometry (list (make block (material diel)
  (center (c->l 0 0 0))
```

```
(e1 (c->l 1 1 0))
(e2 (c->l 1 -1 0))
(e3 (c->l 0 0 1))
(size infinity w h)
(make block (material diel)
(center (c->l 0.125 0.125 h))
(e1 (c->l 1 1 0))
(e2 (c->l 1 -1 0))
(e3 (c->l 0 0 1))
(size w infinity h))))
(set-param! resolution 32)
(set-param! num-bands 20)
(run (output-at-kpoint (vector3 0.5 0.5 0) output-dpwr))
```

Appendix B

Mathematica code for refractive index measurements

```
(*****  
  
    Adapted from  
    Roman E. Maeder: Programming in Mathematica,  
    Second Edition, Addison-Wesley, 1991.  
  
*****)  
  
(* set up the package context, included any imports *)  
  
BeginPackage["MyPackages`Slabv3`"]  
  
Needs["Statistics`DescriptiveStatistics`"] (* read in any hidden  
imports \  
*)  
  
(* usage messages for the exported functions and the context itself *)  
  
Skeleton::usage = "Skeleton.m is a package for slab waveguide  
analysis."  
  
betaF::usage = "betaF[Angles,nc,np,prism angle]=mode indices ."  
  
teModes::usage = " teModes[mode indices, ns, nc, lambda]=ri and  
thickness "  
  
tmModes::usage=" tmModes[mode indices, ns, nc, lambda]=ri and thickness  
"
```

```

Begin["`Private`"] (* begin the private context *)

te[modeIndex_List,nf_,ns_,nc_,k_] :=
Module[{a,b,i1,i2,n,v},
a=(ns^2-nc^2)/(nf^2-ns^2);
b=(modeIndex^2-ns^2)/(nf^2-ns^2);
i1=ArcTan[Sqrt[b/(1-b)]] + ArcTan[Sqrt[(b+a)/(1-b)]];
i2=Table[i1[[n]]+(n-1) Pi,{n,Length[i1]}];
v=i2/Sqrt[1-b];
v/(k Sqrt[nf^2 - ns^2])
]

tm[modeIndex_List,nf_,ns_,nc_,k_] :=
Module[{a,b,d,qs,i1,i2,n,v},
qs=modeIndex^2/nf^2 + modeIndex^2/ns^2 - 1;
a=nf^4/nc^4 + (ns^2-nc^2)/(nf^2-ns^2);
b=(modeIndex^2-ns^2)/(nf^2-ns^2)*(nf^2)/(qs*ns^2);
d=(1-ns^2)/nf^2 + (1-nc^2)/nf^2;
i1=ArcTan[Sqrt[b/(1-b)]]+ArcTan[Sqrt[(b+a*(1-b*d))/(1-b)]];
i2=Table[i1[[n]] + (n-1) Pi, {n,Length[i1]}];
v=i2/(Sqrt[qs]^nf/ns^Sqrt[1-b]);
v/(k Sqrt[nf^2-ns^2])
]

betaF[theta_List,nc_,np_,phi_] :=
np Cos[90 Degree - phi Degree + ArcSin[nc Sin[
theta Degree]/np]]/nc/W

teModes[modeIndex_List,ns_,nc_,lambda_] :=
Module[{k,ri,filmIndex,dummy},
k=2 Pi/lambda;
ri=NMinimize[Variance[te[modeIndex,nf,ns,nc,k]],
{nf,modeIndex[[1]]+1 10^(-5),modeIndex[[1]]+1 10^(-3)}];
filmIndex=nf/.ri[[2,1]];
Plot[Evaluate[te[modeIndex,x,ns,nc,k] 1 10^6],

```

```

    {x,modeIndex[[1]]+(filmIndex-modeIndex[[1]])/2,
    filmIndex+(filmIndex-modeIndex[[1]])/2},
    AxesLabel -> {"RI", "Thickness (microns)"},
    AxesOrigin -> {modeIndex[[1]]+(filmIndex-modeIndex[[1]])/2,
    te[modeIndex,filmIndex+(filmIndex-modeIndex[[1]])/2,
    ns,nc,k][[1]]*1 10^6}
];
Print["Thickness = ",N[Mean[te[modeIndex,
    filmIndex,ns,nc,k]],3]];
Print["Refractive index = ",N[filmIndex,6]];
]

tmModes[modeIndex_List,ns_,nc_,lambda_] :=
Module[{k,ri,filmIndex,dummy},
    k=2 Pi/lambda;
    ri=NMinimize[Variance[tm[modeIndex,nf,ns,nc,k]],
        {nf,modeIndex[[1]]+1 10^(-5),modeIndex[[1]]+1 10^(-3)}];
    filmIndex=nf/.ri[[2,1]];
    Plot[Evaluate[tm[modeIndex,x,ns,nc,k] 1 10^6],
        {x,modeIndex[[1]]+(filmIndex-modeIndex[[1]])/2,
        filmIndex+(filmIndex-modeIndex[[1]])/2},
        AxesLabel -> {"RI", "Thickness (microns)"},
        AxesOrigin -> {modeIndex[[1]]+(filmIndex-modeIndex[[1]])/2,
        tm[modeIndex,filmIndex+(filmIndex-modeIndex[[1]])/2,
        ns,nc,k][[1]]*1 10^6}
];
Print["Thickness = ",N[Mean[tm[modeIndex,
    filmIndex,ns,nc,k]],3]];
Print["Refractive index = ",N[filmIndex,6]];
]

End[] (* end the private context *)

Protect[ betaF,teModes,tmModes ] (* protect exported symbols *)

EndPackage[] (* end the package context *)

```

Part IV

Bibliography

References

- [1] B. N. Chichkov et al. A. Ovsianikov, A. Gaidukeviciute. Two-photon polymerization of hybrid sol-gel materials for photonics applications. *Laser Chemistry*, 2008:7, 2008.
- [2] Mihaela Balu, Joel Hales, David Hagan, and Eric Van Stryland. White-light continuum z-scan technique for nonlinear materials characterization. *Opt. Express*, 12(16):3820–3826, Aug 2004.
- [3] B. Bhuiyan, R.J. Winfield, S. O'Brien, and G.M. Crean. Investigation of the two-photon polymerisation of a zr-based inorganic-organic hybrid material system. *Applied Surface Science*, 252(13):4845 – 4849, 2006. Proceedings of the European Materials Research society 2005 - Symposium-J: Advances in Laser and Lamp Processing of Functional Materials - EMRS 2005 Symposium J.
- [4] Scherer G.W. Brinker C.J. *The Physics and Chemistry of Sol-Gel Processing*. Academic Press, 1990.
- [5] C.T. Chan, S. Datta, K.M. Ho, and C.M. Soukoulis. A7 structure: A family of photonic crystals. *Phys. Rev. B*, 50(3):1988–1991, Jul 1994.
- [6] T. Corrales, F. Catalina, C. Peinado, N. S. Allen, A. M. Rufs, C. Bueno, and M. V. Encinas. Photochemical study and photoinitiation activity of macroinitiators based on thioxanthone. *Polymer*, 43(17):4591 – 4597, 2002.
- [7] S. Couris, M. Renard, O. Faucher, B. Lavorel, R. Chaux, E. Koudoumas, and X. Michaut. An experimental investigation of the nonlinear refractive index (n_2) of carbon disulfide and toluene by spectral shearing interferometry and z-scan techniques. *Chemical Physics Letters*, 369(3-4):318 – 324, 2003.
- [8] R. de Nalda, R. del Coso, J. Requejo-Isidro, J. Olivares, A. Suarez-Garcia, J. Solis, and C. N. Afonso. Limits to the determination of the

- nonlinear refractive index by the z-scan method. *J. Opt. Soc. Am. B*, 19(2):289–296, Feb 2002.
- [9] M. Deubel. Direct laser writing of three-dimensional photonic-crystal templates for telecommunications. *Nature Materials*, 3:444–447, 2004.
- [10] M. Deubel, M. Wegener, S. Linden, and G. von Freymann. Angle-resolved transmission spectroscopy of three-dimensional photonic crystals fabricated by direct laser writing. *Applied Physics Letters*, 87(22):221104, 2005.
- [11] L. A. Dorado, R. A. Depine, and H. Míguez. Effect of extinction on the high-energy optical response of photonic crystals. *Phys. Rev. B*, 75(24):241101, Jun 2007.
- [12] Luis A. Dorado, Ricardo A. Depine, Daniel Schinca, Gabriel Lozano, and Hernán Míguez. Experimental and theoretical analysis of the intensity of beams diffracted by three-dimensional photonic crystals. *Phys. Rev. B*, 78(7):075102, Aug 2008.
- [13] Xuan-Ming Duan, Hong-Bo Sun, Koshiro Kaneko, and Satoshi Kawata. Two-photon polymerization of metal ions doped acrylate monomers and oligomers for three-dimensional structure fabrication. *Thin Solid Films*, 453-454:518 – 521, 2004. Proceedings of Symposium H on Photonic Processing of Surfaces, Thin Films and Devices, of the E-MRS 2003 Spring Conference.
- [14] Mauro Falconieri. Thermo-optical effects in z -scan measurements using high-repetition-rate lasers. *Journal of Optics A: Pure and Applied Optics*, 1(6):662, 1999.
- [15] S. Foteinopoulou and C. M. Soukoulis. Electromagnetic wave propagation in two-dimensional photonic crystals: A study of anomalous refractive effects. *Phys. Rev. B*, 72(16):165112, Oct 2005.
- [16] Stavroula. Foteinopoulou. Electromagnetic wave propagation in two-dimensional photonic crystals /. 2003.
- [17] J. F. Galisteo-López, E. Palacios-Lidón, E. Castillo-Martínez, and C. López. Optical study of the pseudogap in thickness and orientation controlled artificial opals. *Phys. Rev. B*, 68(11):115109, Sep 2003.

- [18] R.A. Ganeev, A.I. Ryasnyansky, M. Baba, M. Suzuki, N. Ishizawa, M. Turu, S. Sakakibara, and H. Kuroda. Nonlinear refraction in Cs_2Te . *Applied Physics B: Lasers and Optics*, 78:433–438, 2004. 10.1007/s00340-003-1389-y.
- [19] F. García-Santamaría, J. F. Galisteo-López, P. V. Braun, and C. López. Optical diffraction and high-energy features in three-dimensional photonic crystals. *Phys. Rev. B*, 71(19):195112, May 2005.
- [20] Andrea Gnoli, Luca Razzari, and Marcofabio Righini. Z-scan measurements using high repetition rate lasers: how to manage thermal effects. *Opt. Express*, 13(20):7976–7981, Oct 2005.
- [21] Wojciech Haske, Vincent W. Chen, Joel M. Hales, Wenting Dong, Stephen Barlow, Seth R. Marder, and Joseph W. Perry. 65 nm feature sizes using visible wavelength 3-d multiphoton lithography. *Opt. Express*, 15(6):3426–3436, Mar 2007.
- [22] K. M. Ho, C. T. Chan, and C. M. Soukoulis. Existence of a photonic gap in periodic dielectric structures. *Phys. Rev. Lett.*, 65(25):3152–3155, Dec 1990.
- [23] K.M. Ho, C.T. Chan, C.M. Soukoulis, R. Biswas, and M. Sigalas. Photonic band gaps in three dimensions: New layer-by-layer periodic structures. *Solid State Communications*, 89(5):413 – 416, 1994.
- [24] Pascal Huguet-Chantôme, Ludovic Escoubas, and François Flory. Guided-wave technique for the measurement of dielectric thin-film materials’ thermal properties. *Appl. Opt.*, 41(16):3127–3131, Jun 2002.
- [25] K. Inoue. *Photonic Crystals: Physics, Fabrication and Applications*. Springer-Verlag, Berlin, 2010.
- [26] Baohua Jia, Dario Buso, Joel van Embden, Jiafang Li, and Min Gu. Photosensitive nanocomposites: Highly non-linear quantum dot doped nanocomposites for functional three-dimensional structures generated by two-photon polymerization (adv. mater. 22/2010). *Advanced Materials*, 22(22):n/a–n/a, 2010.
- [27] J. D. Joannopoulos. Photonic crystals: putting a new twist on light. *Nature*, 386(6621):143–149, 1997.

- [28] John D. Joannopoulos, Robert D. Meade, and Joshua N. Winn. *Photonic Crystals: Molding the Flow of Light*. Princeton University Press, second edition, February 2008.
- [29] Sajeev John. Strong localization of photons in certain disordered dielectric superlattices. *Phys. Rev. Lett.*, 58(23):2486–2489, Jun 1987.
- [30] Steven Johnson and John Joannopoulos. Block-iterative frequency-domain methods for maxwell’s equations in a planewave basis. *Opt. Express*, 8(3):173–190, Jan 2001.
- [31] Saulius Juodkazis, Vygantas Mizeikis, Shigeki Matsuo, Kosei Ueno, and Hiroaki Misawa. Three-dimensional micro- and nano-structuring of materials by tightly focused laser radiation. *Bulletin of the Chemical Society of Japan*, 81(4):411–448, 2008.
- [32] H. Kogelnik and V. Ramaswamy. Scaling rules for thin-film optical waveguides. *Appl. Opt.*, 13(8):1857–1862, Aug 1974.
- [33] T. Kondo, S. Juodkazis, and H. Misawa. Reduction of capillary force for high-aspect ratio nanofabrication. *Applied Physics A: Materials Science & Processing*, 81:1583–1586, 2005. 10.1007/s00339-005-3337-7.
- [34] P. Kopperschmidt. Tetragonal photonic woodpile structures. *Applied Physics B: Lasers and Optics*, 76:729–734, 2003. 10.1007/s00340-003-1169-8.
- [35] Hideo Kosaka, Takayuki Kawashima, Akihisa Tomita, Masaya Notomi, Toshiaki Tamamura, Takashi Sato, and Shojiro Kawakami. Superprism phenomena in photonic crystals. *Phys. Rev. B*, 58(16):R10096–R10099, Oct 1998.
- [36] V.Q. Lam, S. Turrell, A. Martucci, M. Bouazaoui, and B. Capoen. Synthesis and optical properties of mptms-capped cds quantum dots embedded in tio2 thin films for photonic applications. *Journal of Non-Crystalline Solids*, 352(30-31):3315 – 3319, 2006.
- [37] Kwang-Sup Lee, Dong-Yol Yang, Sang Hu Park, and Ran Hee Kim. Recent developments in the use of two-photon polymerization in precise 2d and 3d microfabrications. *Polymers for Advanced Technologies*, 17(2):72–82, 2006.

- [38] S.Y Lin. A three-dimensional photonic crystal operating at infrared wavelengths. *Nature*, 394:251–253, 1998.
- [39] Virginie Lousse and Jean-Pol Vigneron. Self-consistent spectrum of photonic crystals containing non-linear optical materials. *Synthetic Metals*, 116(1-3):461 – 463, 2001.
- [40] Gabriel Lozano, Javier E. Mazzaferri, Luis A. Dorado, Silvia Ledesma, Ricardo A. Depine, and Hernán Míguez. Angular dependence of the intensity of light beams diffracted by colloidal crystals. *J. Opt. Soc. Am. B*, 27(7):1394–1399, Jul 2010.
- [41] Chiyan Luo, Steven G. Johnson, and J. D. Joannopoulos. All-angle negative refraction in a three-dimensionally periodic photonic crystal. *Applied Physics Letters*, 81(13):2352–2354, 2002.
- [42] Chiyan Luo, Steven G. Johnson, J. D. Joannopoulos, and J. B. Pendry. All-angle negative refraction without negative effective index. *Phys. Rev. B*, 65(20):201104, May 2002.
- [43] Mohamed Mokhtar Mohamed, T. M. Salama, and T. Yamaguchi. Synthesis, characterization and catalytic properties of titania-silica catalysts. *Colloids and Surfaces A: Physicochemical and Engineering Aspects*, 207(1-3):25 – 32, 2002.
- [44] Jun Hyuk Moon and Shu Yang. Chemical aspects of three-dimensional photonic crystals. *Chemical Reviews*, 110(1):547–574, 2010. PMID: 19655793.
- [45] M. Notomi. Theory of light propagation in strongly modulated photonic crystals: Refractionlike behavior in the vicinity of the photonic band gap. *Phys. Rev. B*, 62(16):10696–10705, Oct 2000.
- [46] Masaya Notomi. Manipulating light with strongly modulated photonic crystals. *Reports on Progress in Physics*, 73(9):096501, 2010.
- [47] Aleksandr Ovsianikov, Jacques Vierterl, Boris Chichkov, Mohamed Oubaha, Brian MacCraith, Ioanna Sakellari, Anastasia Giakoumaki, David Gray, Maria Vamvakaki, Maria Farsari, and Costas Fotakis. Ultra-low shrinkage hybrid photosensitive material for two-photon polymerization microfabrication. *ACS Nano*, 2(11):2257–2262, 2008.

- [48] Emile Pelletier, F. Flory, and Y. Hu. Optical characterization of thin films by guided waves. *Appl. Opt.*, 28(14):2918–2924, Jul 1989.
- [49] J. B. Pendry. Negative refraction makes a perfect lens. *Phys. Rev. Lett.*, 85(18):3966–3969, Oct 2000.
- [50] Williams J.D Prasad, N.P. *Introduction to Nonlinear optical effects in molecules & polymers*. Wiley Interscience, 1990.
- [51] YuanQiao Rao and Samuel Chen. Molecular composites comprising tio2 and their optical properties. *Macromolecules*, 41(13):4838–4844, 2008.
- [52] David Roundy and John Joannopoulos. Photonic crystal structure with square symmetry within each layer and a three-dimensional band gap. *Applied Physics Letters*, 82(22):3835–3837, 2003.
- [53] I. Sakellari, A. Gaidukeviciute, A. Giakoumaki, D. Gray, C. Fotakis, M. Farsari, M. Vamvakaki, C. Reinhardt, A. Ovsianikov, and B. Chichkov. Two-photon polymerization of titanium-containing sol-gel composites for three-dimensional structure fabrication. *Applied Physics A: Materials Science & Processing*, 100:359–364, 2010. 10.1007/s00339-010-5864-0.
- [54] K. Sakoda. *Optical properties of photonic crystals*. Springer-Verlag, Berlin, 2001.
- [55] J. Serbin, A. Egbert, A. Ostendorf, B. N. Chichkov, R. Houbertz, G. Dommann, J. Schulz, C. Cronauer, L. Fröhlich, and M. Popall. Femtosecond laser-induced two-photon polymerization of inorganic organic hybrid materials for applications in photonics. *Opt. Lett.*, 28(5):301–303, Mar 2003.
- [56] Jesper Serbin and Min Gu. Superprism phenomena in polymeric woodpile structures. *Journal of Applied Physics*, 98(12):123101, 2005.
- [57] M. Sheik-Bahae, A. A. Said, T.-H. Wei, D. J. Hagan, and E. W. Van Stryland. Sensitive measurement of optical nonlinearities using a single beam. *IEEE Journal of Quantum Electronics*, 26:760–769, 1990.
- [58] Alexander Sinitskii, Vera Abramova, Tatyana Laptinskaya, and Yuri D. Tretyakov. Domain mapping of inverse photonic crystals by laser diffraction. *Physics Letters A*, 366(4-5):516 – 522, 2007.

- [59] C.M. Soukoulis. *Photonic Band Gaps and Localization*. Nato Scientific Affairs Division, 2003.
- [60] I. Staude, M. Thiel, S. Essig, C. Wolff, K. Busch, G. von Freymann, and M. Wegener. Fabrication and characterization of silicon woodpile photonic crystals with a complete bandgap at telecom wavelengths. *Opt. Lett.*, 35(7):1094–1096, Apr 2010.
- [61] Hong-Bo Sun and Satoshi Kawata. Two-photon photopolymerization and 3d lithographic microfabrication. In *NMR . 3D Analysis . Photopolymerization*, volume 170 of *Advances in Polymer Science*, pages 169–273. Springer Berlin / Heidelberg, 2004. 10.1007/b94405.
- [62] Hong-Bo Sun, Kenji Takada, Moon-Soo Kim, Kwang-Sup Lee, and Satoshi Kawata. Scaling laws of voxels in two-photon photopolymerization nanofabrication. *Applied Physics Letters*, 83(6):1104–1106, 2003.
- [63] Quan Sun, Saulius Juodkazis, Naoki Murazawa, Vygantas Mizeikis, and Hiroaki Misawa. Freestanding and movable photonic microstructures fabricated by photopolymerization with femtosecond laser pulses. *Journal of Micromechanics and Microengineering*, 20(3):035004, 2010.
- [64] Z.-B. Sun, X.-Z. Dong, W.-Q. Chen, S. Nakanishi, X.-M. Duan, and S. Kawata. Multicolor polymer nanocomposites: In situ synthesis and fabrication of 3d microstructures. *Advanced Materials*, 20(5):914–919, 2008.
- [65] Z.-B. Sun, X.-Z. Dong, S. Nakanishi, W.-Q. Chen, X.-M. Duan, and S. Kawata. Log-pile photonic crystal of cds polymer nanocomposites fabricated by combination of two-photon polymerization and in situ synthesis. *Applied Physics A: Materials Science & Processing*, 86:427–431, 2007. 10.1007/s00339-006-3776-9.
- [66] Tomokazu Tanaka, Hong-Bo Sun, and Satoshi Kawata. Rapid sub-diffraction-limit laser micro/nanoprocessing in a threshold material system. *Applied Physics Letters*, 80(2):312–314, 2002.
- [67] M. Thiel, J. Fischer, G. von Freymann, and M. Wegener. Direct laser writing of three-dimensional submicron structures using a continuous-wave laser at 532 nm. *Applied Physics Letters*, 97(22):221102, 2010.

- [68] P. K. Tien, G. Smolinsky, and R. J. Martin. Thin organosilicon films for integrated optics. *Appl. Opt.*, 11(3):637–642, Mar 1972.
- [69] P. K. TIEN and R. ULRICH. Theory of prism-film coupler and thin-film light guides. *J. Opt. Soc. Am.*, 60(10):1325–1337, Oct 1970.
- [70] P. K. Tien, R. Ulrich, and R. J. Martin. Modes of propagating light waves in thin deposited semiconductor films. *Applied Physics Letters*, 14(9):291–294, 1969.
- [71] R. Ulrich and R. Torge. Measurement of thin film parameters with a prism coupler. *Appl. Opt.*, 12(12):2901–2908, Dec 1973.
- [72] Hongyu Wang, Jun Wei, Xuesong Jiang, and Jie Yin. Effect of n-phenylmaleimide on a novel chemically bonded polymerizable photoinitiator comprising the structure of planar n-phenylmaleimide and benzophenone for photopolymerization. *Polymer International*, 56(2):200–207, 2007.
- [73] Boyd W.R. *Nonlinear Optics, Second edition*. Academic Press, 2002.
- [74] Sibeï Xiong and Hiroshi Fukushima. Analysis of light propagation in index-tunable photonic crystals. *Journal of Applied Physics*, 94(2):1286–1288, 2003.
- [75] E. Yablonovitch and T. J. Gmitter. Photonic band structure: The face-centered-cubic case. *Phys. Rev. Lett.*, 63(18):1950–1953, Oct 1989.
- [76] Eli Yablonovitch. Inhibited spontaneous emission in solid-state physics and electronics. *Phys. Rev. Lett.*, 58(20):2059–2062, May 1987.
- [77] Xiaofang Yu and Shanhui Fan. Anomalous reflections at photonic crystal surfaces. *Phys. Rev. E*, 70(5):055601, Nov 2004.
- [78] Gongjian Zhang and Keisuko Sasaki. Measuring anisotropic refractive indices and film thicknesses of thin organic crystals using the prism coupling method. *Appl. Opt.*, 27(7):1358–1362, Apr 1988.